Title
Properties of Irregular Satellites and Fragmenting Comets

Author
Graykowski, Ariel

Publication Date
2022

UNIVERSITY OF CALIFORNIA
Los Angeles

Properties of Irregular Satellites and Fragmenting Comets

A dissertation submitted in partial satisfaction
of the requirements for the degree
Doctor of Philosophy in Geophysics and Space Physics

by

Ariel Graykowski

2022

ABSTRACT OF THE DISSERTATION

Properties of Irregular Satellites and Fragmenting Comets

by

Ariel Graykowski
Doctor of Philosophy in Geophysics and Space Physics
University of California, Los Angeles, 2022
Professor David C. Jewitt, Chair

In this thesis, I investigate the nature of two small body populations; the irregular satellite populations of the giant planets and the properties of fragmented nuclei of comets. In both cases the objective is to understand evolutionary processes acting on primitive solar system objects. An optical color survey of 43 irregular satellites enabled color comparisons with other small body populations that may reflect upon the origin of the irregular satellites. Ultrared matter (color index B-R $\geq$ 1.6), while abundant in the excited Kuiper belt and Centaur populations, is depleted from the irregular satellites. Also, the color distributions of the irregular satellites at each giant planet are statistically similar to each other, consistent with a common source region and/or evolutionary mechanism. Separately, the current observed supply of comets allows for estimates on the masses of their outer solar system source regions, however, comet fragmentation may occur more often than previously thought, which will lead to shorter estimates of comet lifetimes than predicted. As a case study, I analyzed archival Hubble Space telescope images of comet 73P/Schwassmann-Wachmann 3 (73P). The measured rotation period of the nucleus is much longer than the critical period for rotational instability for any reasonable nucleus density and shape, even in the absence of tensile strength. The data also show hundreds of fragments within 73P-B and 73P-G on which photometry was used to measure the brightness distribution of the fragments. I also measure the motion of these fragments and find the relative speeds of the fragments within 73P-B are a few m/s, implying an impulsive breakup about 7 days prior to the observations. Both the irregular satellites and comets are small bodies comprised of primitive material. The origin and evolution of the small bodies describe the early formation and evolution of the solar system itself.

The dissertation of Ariel Graykowski is approved.

Ian S. McLean

David A. Paige

Hilke E. Schlichting

David C. Jewitt, Committee Chair

University of California, Los Angeles

2022

To my grandparents:

Gerald and Yvonne Graykowski
and
Kenneth and Sandra Kant

Rest in Peace

TABLE OF CONTENTS

LIST OF FIGURES

LIST OF TABLES

ACKNOWLEDGMENTS

I want to acknowledge all of the people who have made this work possible, and supported me throughout my graduate student career.

To my advisor, David Jewitt, who gave me the opportunity to study planetary science at UCLA. I am so thankful for everything he taught me, his collaboration on my work, and his constant support throughout the years.

To the EPSS graduate students, who keep each other motivated and happy. Tyler Powell, Danielle Kline, Man-To Hui, and Dave Milewski deserve special mention. My experience and my pursuit of knowledge was elevated because of them.

To my mom, dad, and sister - Kathy, Steve, and Hannah. Any stress and anxiety that may have arisen during this journey was all dumped on them, and they carried it for me without question and with pride. That has given me the confidence I needed to move through this journey.

Thank you.

Chapter Acknowledgments:

Chapter 2 is adapted from the peer-reviewed paper titled "Colors and Shapes of the Irregular Planetary Satellites" by Graykowski & Jewitt, which has been published in the Astronomical Journal (Graykowski, A. & Jewitt, D. 2018, AJ, 155, 184. doi:10.3847/1538-3881/aab49b). The Co-author David Jewitt was the PI on the project. The data presented in this chapter were obtained at the W. M. Keck Observatory, which is operated as a scientific partnership among the California Institute of Technology, the University of California and the National Aeronautics and Space Administration. The Observatory was made possible by the generous financial support of the W. M. Keck Foundation. This work was supported, in part, by a grant to D. Jewitt from NASA.

Chapter 3 is adapted from the peer-reviewed paper titled "Fragmented Comet 73P / Schwassmann-Wachmann 3", which has been published in the Astronomical Journal (Graykowski, A. & Jewitt, D. 2019, AJ, 158, 112. doi:10.3847/1538-3881/ab2f7a). The Co-author David Jewitt was the PI on the project. This work was supported by the HST's Archival Research Program, proposal #15301 awarded to D.J. Also, A.G. acknowledges her NESSF grant #18-0217 for providing funding to accomplish this work. This work was based on observations made with the NASA/ESA Hubble Space Telescope, and obtained from the Hubble Legacy Archive, which is a collaboration between the Space Telescope Science Institute (STScI/NASA), the Space Telescope European Coordinating Facility (ST-ECF/ESA) and the Canadian Astronomy Data Centre (CADC/NRC/CSA).

Chapter 4 is adapted from the paper titled "Hubble Space Telescope Investigation of Fragmenting Comet 73P/Schwassmann-Wachmann 3: 73P-B and -G", which is in preparation to be submitted to the Astronomical Journal (Graykowski & Jewitt 2022, In Prep.). The Co-author David Jewitt was the PI on the project. This work was supported by the HST's Archival Research Program, proposal GO 15301 awarded to D.J. Also, A.G. acknowledges her NESSF grant #18-0217 for providing funding to accomplish this work. This work was based on observations made with the NASA/ESA Hubble Space Telescope, and obtained from the Hubble Legacy Archive, which is a collaboration between the Space Telescope Science Institute (STScI/NASA), the Space Telescope European Coordinating Facility (ST-ECF/ESA) and the Canadian Astronomy Data Centre (CADC/NRC/CSA).

VITA

Education

2018 - 2022	Ph.D. Candidate (Geophysics and Space Physics), University of California, Los Angeles
2018	M.S. (Geophysics and Space Physics), University of California, Los Angeles
2015	B.S. (Physics with an Emphasis in Astrophysics), University of California, Davis

Research Experience

2018 - 2021	NASA Earth and Space Science Fellow (NESSF), Project title: "Systematic Investigation of Cometary Fragmentation"
2018	Keck Visiting Scholar, W. M. Keck Observatory - Waimea, HI
2014 - 2015	Undergraduate Research Assistant, University of California, Davis. Advisors: Qing-Zhu Yin and Anthony Tyson

Teaching Experience

2016 - 2022	Astrobiology (EPSS 3), Introduction to Oceanography (EPSS 15), Evolution of the Cosmos and of Life (CLUSTER 70a, 70b, 70c)

Observing Programs

Kitt Peak National Observatory

2019	PI, HDI instrument on the WIYN 0.9 m telescope

2016, '17, '18	Co-I (PI: Man-To Hui), HDI instrument on the WIYN 0.9 m telescope
2015	Co-I (Co-I (PI: David Jewitt), HDI instrument on the WIYN 0.9 m telescope

W. M. Keck Observatory

2018	Co-I (PI:David Jewitt); NIRES instrument on the Keck II telescope
2015, '17, '18	Co-I (PI: David Jewitt); LRIS instrument on Keck I telescope

PUBLICATIONS

A. Graykowski and D. Jewitt (2021). Split Comet 73P: Fragments 73P-B and 73P-G. In Prep.

A. Graykowski and D. Jewitt (2019). Fragmented Comet 73P/Schwassmann-Wachmann 3. Astronomical Journal, 158, 112

D. Jewitt, Y. Kim, J. Luu, and **A. Graykowski** (2019). The Discus Comet: C/2014 B1 (Schwartz). Astronomical Journal, 157,103

A. Graykowski and D. Jewitt (2018). Colors and Shapes of the Irregular Planetary Satellites. Astronomical Journal, 155, 184

CHAPTER 1

Introduction

In the outer solar system, the Kuiper belt and Oort cloud are homes to primitive objects that are thought of as artifacts from the formation phase of the planets. The Kuiper belt begins beyond the orbit of Neptune around 30 AU and the Oort cloud begins near 2000 AU (Dones et al. 2004). Towards the end of the planetary formation phase, icy planetesimals in the planet region ($\sim$ 4 - 30 AU) were easily perturbed, with their perihelion remaining constant and their semi-major axes pumped well into the Oort cloud (Dones et al. 2004). Some were saved from ejection by forces from passing stars and the galactic tide, which are random, causing nearly isotropic velocity distributions in the Oort cloud, and keeping the semi-major axes of the comets between $a \sim 10,000$ and $a \sim 100,000$ AU (Heisler & Tremaine 1986, Duncan et al. 1987, Tremaine 1993). These icy bodies are known as the long-period comets, sublimating when they orbit close to the Sun at their perihelion. The short-period comets did not experience such dramatic perturbations. Instead, icy planetesimals with Neptune encountering orbits ($\sim$ 34 - 50 AU) were perturbed such that their semi-major axes reached $a \sim 32$ to $a \sim 48$ AU, making up the scattered disk population in the Kuiper belt, which is thought to be the sole source of the short-period comets (Levison &Duncan, 1997). It is suggested that other small body populations observed within the planet region of the solar system were sourced from the outer protoplanetary disk (OPD) as well, such as the irregular satellites of the giant planets (Morbidelli et al. 2005; Nesvorný et al. 2013). While there is no observational evidence that the irregular satellites dynamically originated from the outer protoplanetary disk, their current physical features are indicative of their early evolution, providing insight to their source region.

This thesis investigates the nature of two small body populations: the irregular satellite populations of the giant planets and the fragmented nuclei of comets. Both are products of accretion in the Sun's planetesimal disk. The irregular satellites were captured, probably during the time of giant planet growth, into weakly bound orbits around their parent planets. Some comets were formed in the vicinity of the giant planets and scattered out to orbits in the Oort cloud while others originated near the Kuiper belt reservoir beyond Neptune.

1.1 Irregular Satellites

1.1.1 Defining Irregular Satellites

Irregular satellites are broadly distinguished from regular satellites by their orbital characteristics. Regular satellites occupy nearly circular, low eccentricity orbits deep within the Hill spheres of their respective planets. The Hill sphere is defined by the volume around a planet where the gravity of the planet dominates over the gravity of the Sun, with radius

$$r_H \sim a_P \left(\frac{m_P}{3M_\odot} \right)^{1/3} \tag{1.1}$$

where a_P is the semi-major axis of the host planet, m_P is the mass of the host planet and $M_\odot$ is the mass of the Sun. In contrast, the irregular satellites orbit at distances up to 0.5-0.6 Hill radii and are subject to significant torques from the Sun even while remaining bound to the host planets. The irregulars also have large eccentricities, $e = 0.1$ to 0.7, and inclinations, i, many with $i > 90°$ (Jewitt and Haghighipour 2007, Nicholson et al. 2008). Only the giant planets possess irregular satellites. The current number of irregular satellites observed at each giant planet, along with the mass, semi-major axis, and Hill radius of each host planet are listed in Table 1.1. The difference in the orbits of the regular and irregular satellites is clear in Figures 1.1 and 1.2. The semi-major axes, inclinations, and eccentricities of each irregular satellite are plotted in Figures 1.3 and 1.4.

Planet	m_P [a]	a_P (AU)[b]	r_H (AU)[c]	N_i [d]
Jupiter	310	5	0.35	71
Saturn	95	10	0.43	57
Uranus	15	20	0.47	9
Neptune	17	30	0.77	7

Table 1.1: Irregular Satellites at Each Giant Planet

[a] Mass of the planet in Earth masses

[b] Semi-major axis of the planet in AU

[c] Hill radius of the planet in AU

[d] Number of irregular satellites reported at each giant planet

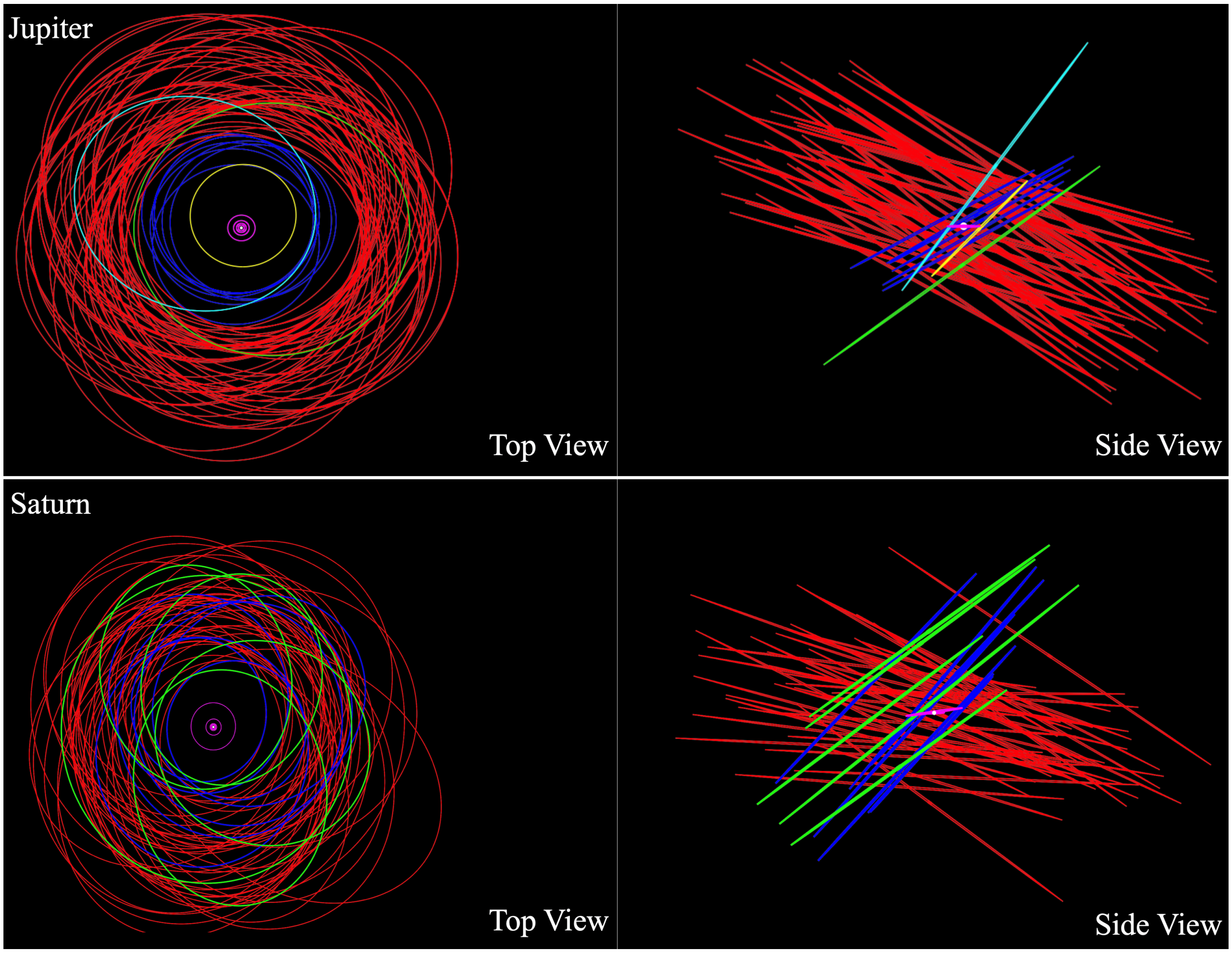

Figure 1.1: Satellite Orbits at Jupiter and Saturn - Orbits in pink represent the orbits of the regular satellites, red represents retrograde irregular satellites, blue, light blue, yellow, and green represent prograde irregular satellites. The left column images are top-down views, and the right column images are side-on views. Adapted from Scott S. Sheppard's website, `https://sites.google.com/carnegiescience.edu/sheppard/moons?authuser=0`.

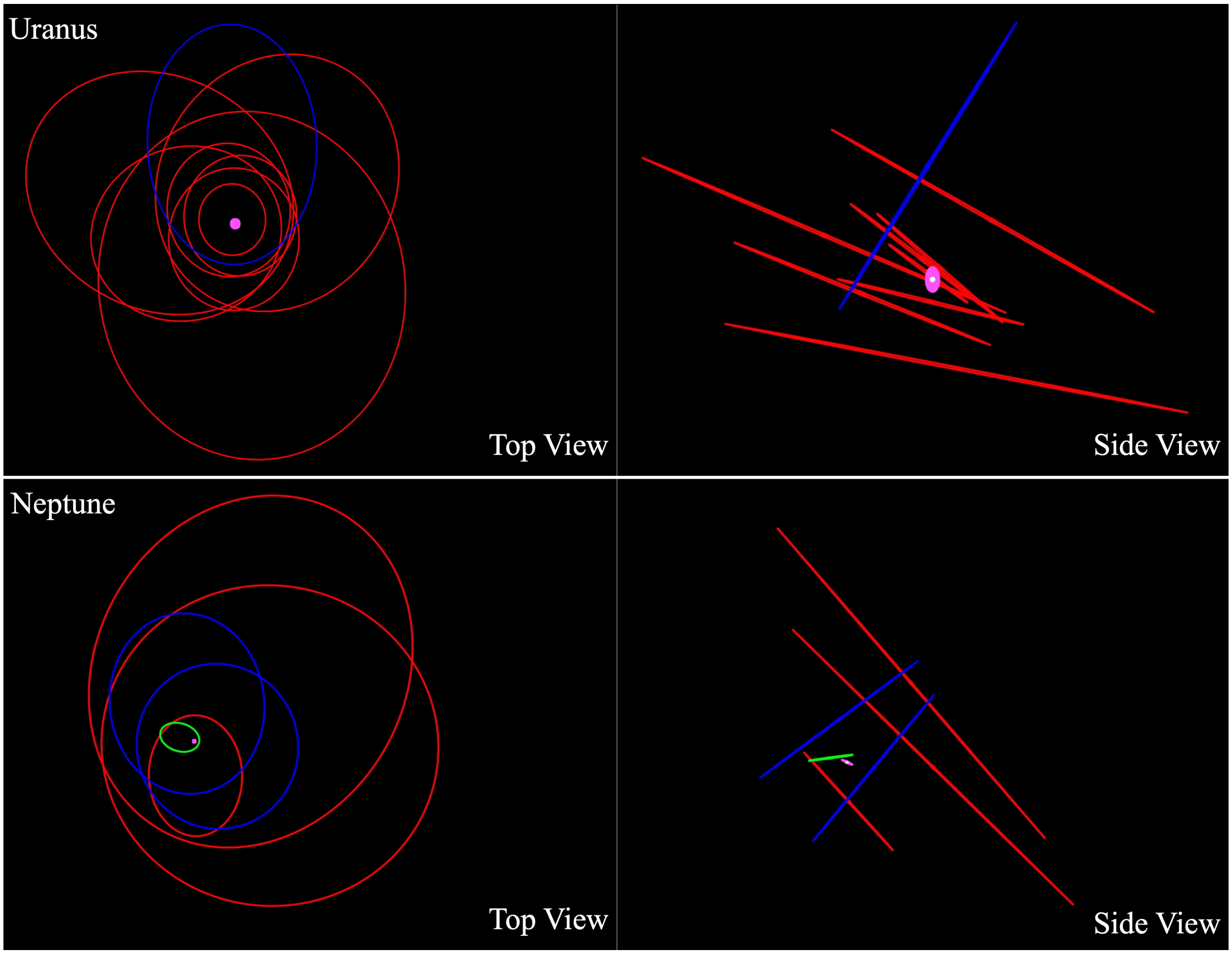

Figure 1.2: Satellite Orbits at Uranus and Neptune - Same as Figure 1.1, except Uranus and Neptune instead of Jupiter and Saturn. Adapted from Scott S. Sheppard's website, `https://sites.google.com/carnegiescience.edu/sheppard/moons?authuser=0`.

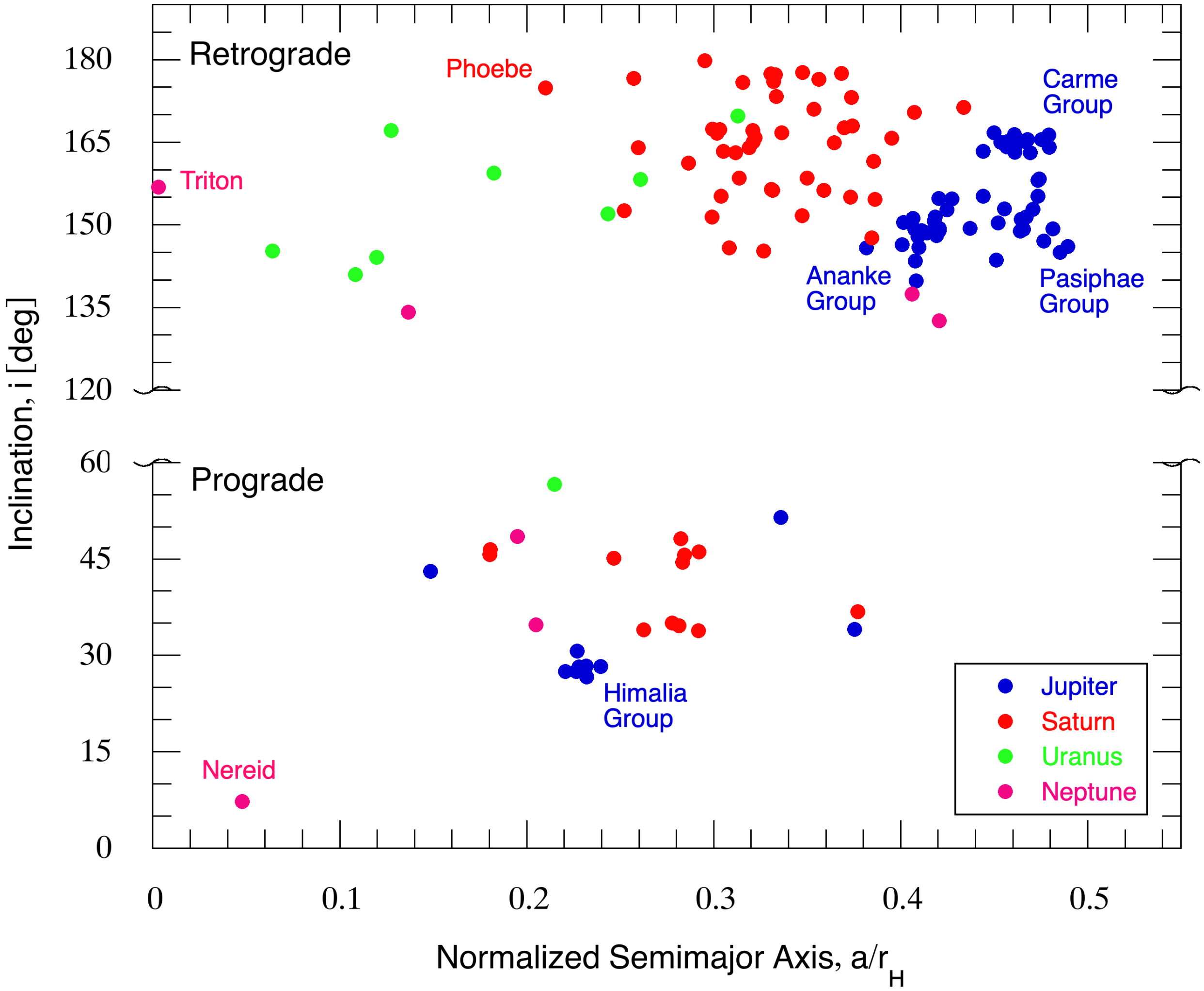

Figure 1.3: Semi-Major Axis, a vs. Inclination, i of the irregular satellites of the giant plants known as of May 10, 2022. The semi-major axis is normalized to the Hill radius, r_H, of the irregular satellites' respective host planet. Jovian irregular satellites are represented by blue circles, Saturnian satellites are red, Uranian satellites are green, and Neptunian satellites are pink. The satellites with inclination $i > 90°$ are orbiting in a retrograde motion and satellites with inclination $i < 90°$ are prograde. There is a clear clumping of Jovian irregular satellites, and those groups represent the labelled collisional family.

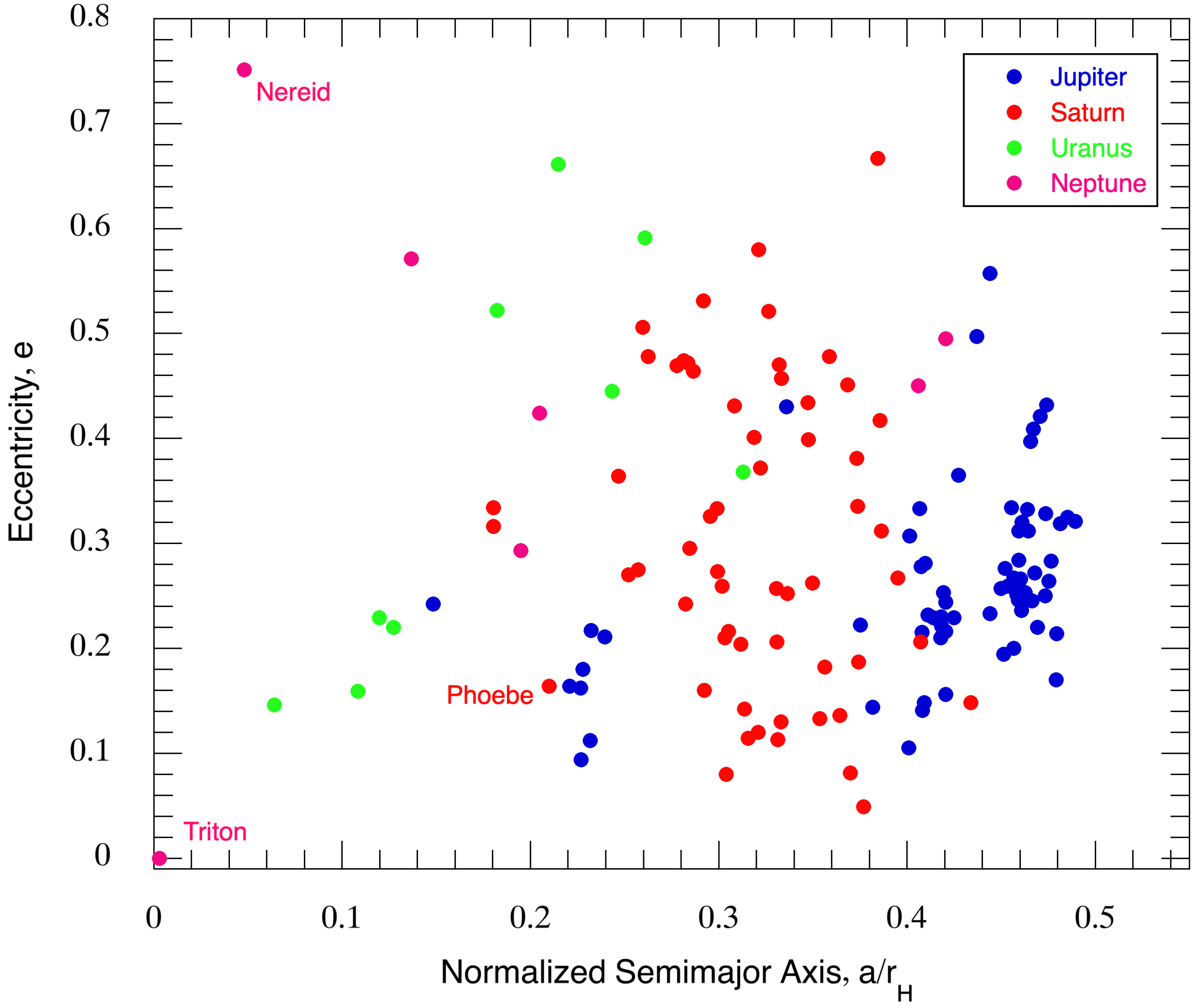

Figure 1.4: Semi-Major Axis, a, vs. Eccentricity, e of the irregular satellites of the giant plants known as of May 10, 2022. The semi-major axis is normalized to the Hill radius, r_H, of the irregular satellites' respective host planet. Jovian irregular satellites are represented by blue circles, Saturnian satellites are red, Uranian satellites are green, and Neptunian satellites are pink. A clumping similar to that seen in Figure 1.3 can be seen here as well, though the clumping is less obvious.

From figures 1.3 and 1.4, it can be seen that while the orbits of the irregular satellites have a large spread of semi-major axes, there are none observed beyond distance of half their host planet's Hill radius. All satellites have normalized semi-major axes $a/r_H < 0.5$. This could indicate an observational bias, as the volume of space that the Hill sphere occupies increases with the cube of the Hill radius, making it increasingly difficult to survey the area for these faint bodies. It may also indicate that the outer part of the Hill sphere is largely depleted of irregular satellites. With their exceptionally large eccentricities, we would expect to see satellites with larger semi-major axes within the surveyed regions during portions of their orbits. This may indicate that the irregular satellites with larger semi-major axes were not stable. With the increased small body survey and observation power that is coming with the Vera C. Rubin Observatory and the James Webb Space Telescope, this observational bias vs. dynamical instability argument should be confirmed in the near future. Also, there are more irregular satellites orbiting in retrograde than prograde as seen in Figure 1.3. This may further imply that the mechanisms leading to the capture of the irregular satellites are asymmetric. However, it could also imply that the long term stability of the irregular satellites after capture is asymmetric. The latter is more supported as the potential mechanisms explained below do not lend to asymmetric capture into pro- and retrograde orbits. Additionally, the orbits of the irregular satellites avoid inclinations $55° < i < 130°$, which is likely due to the Kozai resonance, which drives the inclinations down and the eccentricities up (Carruba et al. 2002, Nesvorný et al. 2003). The high eccentricities observed for the irregular satellites also support this.

1.1.2 The Origin and Evolution of the Irregular Satellites

The irregular satellites' extreme orbits are a result of their early evolution. Regular satellites were formed in the accretion disk of their host star (Lunine & Stevenson 1982; Canup & Ward 2002; Mosqueira & Estrada 2003), lending to their low semi-major axes, eccentricities, and inclinations. This, therefore cannot explain the origin of the irregular satellites. The orbits of the irregular satellites are more consistent with capture from initially heliocentric orbits. Temporary capture is common, especially in the early solar system (Carusi & Valsecchi 1979). Typically, in these cases, a body will temporally orbit a more massive body and then return to a heliocentric orbit on timescales of ∼10s of years (Benner & McKinnon 1995). In some cases, temporarily captured bodies crash into their temporary host, as was the case with comet Shoemaker-Levy 9, which famously split apart during its temporary orbit around Jupiter, and eventually the fragments collided with Jupiter (Weaver et al. 1995). These situations occur on timescales of ∼1000 years (Kary & Dones 1996). Permanent capture is less common, as energy needs to be lost from the system. There are several proposed mechanisms to permanently capture the irregular satellites. When considering mechanisms, it is important to keep in mind that the size distributions of the irregular satellites of each giant planet are similarly shallow, roughly consistent with differential power laws having index $q = 2$ (Figure 1.5), suggesting capture from a common source region by a common mechanism (Sheppard and Jewitt 2003, Jewitt and Sheppard 2005).

Three main classes of capture mechanism have been proposed. Pull-down capture relies on the runaway accretion phase of planetary growth, when the Hill radius of the planet grew rapidly (Heppenheimer and Porco, 1977). Nearby bodies might have been permanently captured if the Hill radius expanded on a timescale short compared to the residence time within the Hill spheres. One argument against pull-down capture as a general mechanism is that the ice giants Uranus and Neptune have relatively little H and He in their gaseous envelopes, limiting the effects of runaway growth. In gas-drag, the extended gaseous envelopes of the forming giant planets are supposed to frictionally dissipate the energy of passing bodies, leading to permanent capture (Pollack et al. 1979). This model relies on fine-tuning of the timing, because the collapse of the gaseous envelope is thought to have been rapid. Capture by gas drag is again less attractive for Uranus and Neptune than for Jupiter and Saturn because the ice giants contain a much smaller fraction of their total mass in gas (Jewitt and Sheppard 2005; Jewitt and Haghighipour, 2007). Accordingly, most recent work has

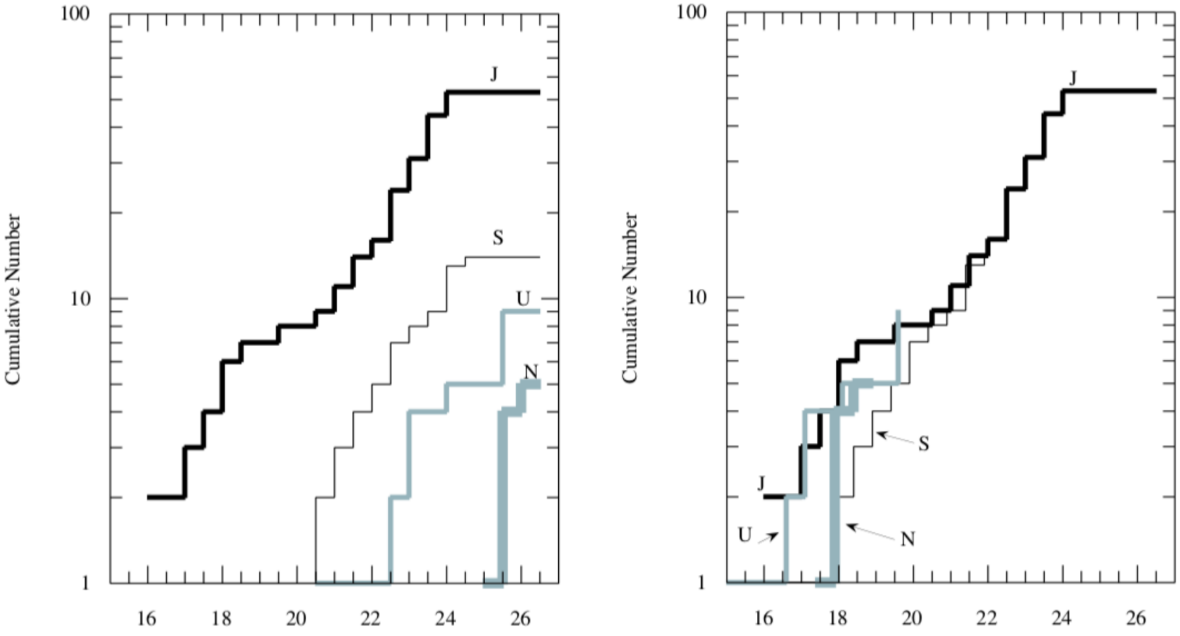

Figure 1.5: Irregular Satellite Size Distribution - (Left) Size distribution of the irregular satellites at each of the giant planets. (Right) Size distributions normalized to Jupiter. Adapted from Jewitt & Sheppard (2005)

focused on capture by three-body interactions, considered first by Colombo and Franklin (1971), since this mechanism is independent of the gas content and growth physics of the host planet. In three body reactions, gravitational scattering between two bodies in the circumplanetary environment can, statistically, lead to the ejection of one and the capture of the other.

It has been proposed that the irregular satellites were captured from the OPD during planetary migration (Morbidelli et al. 2005). Nesvorný et al. (2007) have shown that objects from the OPD could be captured by the giant planets through three-body interactions during planetary migration efficiently within the frameworks of the Nice model. The resulting captured bodies appeared to match the orbital distributions of the irregular satellites and estimated the size of the largest irregular satellites well (Nesvorný et al. 2007; 2013). However, the observed shallow distribution of the irregular satellites was not reproduced. An explanation to reconcile this is the subsequent collisional evolution of the irregular satellites after capture. Several Jovian irregular satellite families have been observed (Nesvorný, 2003). The shallow SFDs of the irregular satellites are evidence of heavy collisional evolution, as most of the larger bodies must have been completely destroyed (Bottke et al. 2010). Of the 71 known irregular Jovian satellites, 67 are members of a collisional family and are listed in Table 1.2. Families are identified by the clustering of their orbital parameters, and the Jovian irregular satellite families are visually clear in Figures 1.3 and 1.4.

	Family	n_F^a	D (km)^b
Prograde	Himalia	7	160
Retrograde	Ananke	22	28
	Carme	22	46
	Pasiphae	16	58

Table 1.2: Jovian Irregular Satellite Families

[a] Number of family members

[b] Diameter of the largest member of the family in km

Bottke et al. (2010) showed a stark contrast in the SFD slopes of the irregular satellite populations and the Jovian Trojans, which are also thought to originate from the OPD but have experienced very little collisional evolution since (Fig. 1.6). This observation brings the source region of the OPD for both the Trojans and the irregular satellites into question. If both populations originated from the same reservoir, where in their evolutionary history did they diverge to produce the different physical characteristics observed today? This stark contrast in slopes may be a result of the size range within which each SFD was measured. Bottke et al. (2010) display the SFD of the largest Jovian Trojans with radii $r > \sim 10$ km, whereas most of the Jovian irregular satellites have radii $r < \sim 10$km. The largest Trojans follow a steep SFD with differential index $q = 5.5 \pm 0.9$, while Jovian Trojans within the size range $2 < r < 20$ km have been measured to have a differential index of $q = 3.0 \pm 0.3$ (Jewitt et al. 2000). This is much closer to the differential index found for the irregular satellites of $q = 2.0$ (Sheppard & Jewitt 2003, Jewitt & Sheppard 2005).

Observations of these small-sized Jovian Trojans, however are incomplete, which also makes it difficult to estimate their collisional timescale, as small bodies dominate the collisional rate of the Trojans. The collisional timescale amongst known irregular satellites is longer than the age of the solar system for the retrograde satellites and on the order of the age of the solar system for the prograde satellites, which shows that current collisional evolution amongst the population is unlikely (Sheppard & Jewitt 2003). However, the flux of potential impactors was greater by an order of 10^5 around the location of the Earth in the early solar system based on lunar impacts. If this greater flux applies to the areas around the giant planets, then it is possible that collisional evolution of the irregular satellites was more efficient earlier in the solar system's evolution. It is then interesting to note the collisional probabilities of each population. Due to the small space taken up by the irregular satellites and their relatively short orbital periods, their collisional probabilities have been found to be several orders of magnitude greater than the Jovian Trojan populations in both the L_4 and L_5 regions (Marzari et al. 1996, Dell'Oro et al. 1998, Bottke et al. 2010). Collisional probabilities along with impact velocities calculated from past works can be seen in Table 1.3. This difference is consistent with the current observations that the irregular satellites appear to be more collisionally evolved than the Jovian Trojans. However, it should again be noted that the population of small Jovian Trojans is still incomplete, and continued observation of both the Trojans and faint irregular satellites (especially those at the furthest heliocentric distances) is needed to fully understand their early evolution.

Chapter 2 investigates the potential source region and early evolution of the irregular satellites further by examining physical characteristics: color and shape. We use colors as a proxy for surface composition, and compare our measurements to other solar system populations, including Kuiper belt populations (Graykowski & Jewitt, 2018).

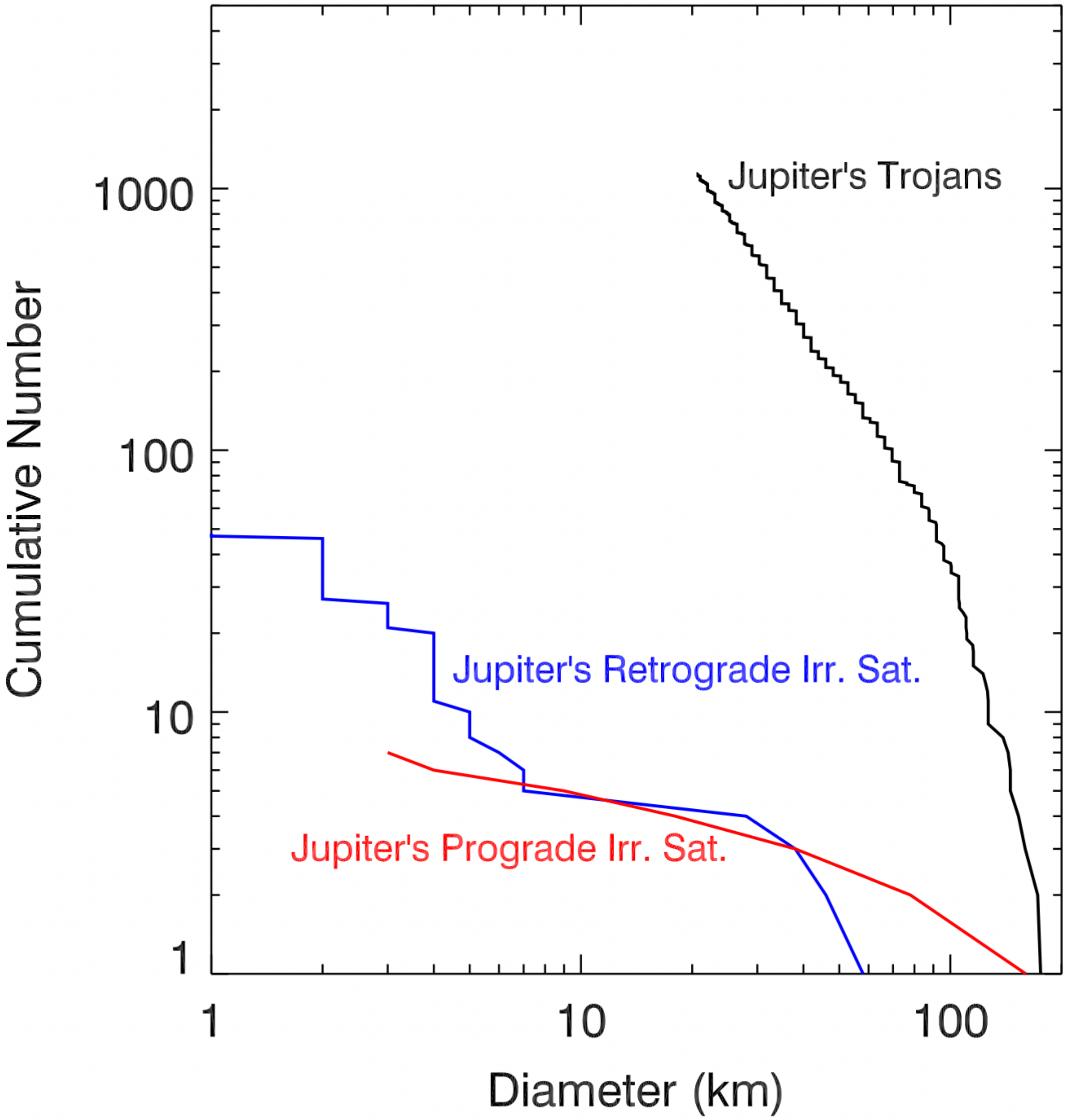

Figure 1.6: Irregular Satellite vs. Jovian Trojan SFDs - SFDs of the Jovian irregular satellites (prograde in red and retrograde in blue) and the Jovian Trojans (black). Adapted from Bottke et al. (2010)

Population	Collisional Probability	Impact Velocity	Source
	(10^{-15} yr^{-1}km^{-2})	(km s^{-1})	
Jupiter Isats			
Pro-Pro	6.5	3.1	Bottke et al. (2010)
Ret-Ret	3.8	3.1	
Pro-Ret	11	6.7	
Saturn Isats			
Pro-Pro	5.3	1.4	
Ret-Ret	5.4	1.4	
Pro-Ret	16	4.0	
Uranus Isats			
Pro-Pro	5.4	1.0	
Ret-Ret	4.6	1.0	
Pro-Ret	11	2.1	
	(10^{-18} yr^{-1}km^{-2})	(km s^{-1})	
Jovian Trojans			
L_4-L_4	6.46 ± 0.09	4.90 ± 0.07	Marzari et al. (1996)
L_5-L_5	5.30 ± 0.10	4.89 ± 0.10	
L_4-L_4	7.79 ± 0.67	4.66	Dell'Oro et al. (1998)
L_5-L_5	6.68 ± 0.18	4.51	

Table 1.3: Collisional Probabilities of the Jovian Trojans and Irregular Satellites

1.2 Fragmenting Comets

1.2.1 Defining and Classifying Comets

Comets are survivors from the formation phase of the solar system. The comets are broadly divided into two categories somewhat arbitrarily based on their orbital periods. Short-period comets (SPCs) are defined as having orbital periods $P < 200$ years, while long-period comets (LPCs) have periods $P > 200$ years. This distinction well identifies the two different source regions supplying the SPCs and LPCs: The Kuiper belt and the Oort cloud, respectively. There are direct observations of the SPC reservoir, the Kuiper belt, beginning with the discovery of the first Kuiper belt object (KBO) in 1992 (Jewitt & Lu, 1993). The Kuiper belt begins at a distance beyond the orbit of Neptune, $\sim$30 AU. Unlike the Kuiper belt objects, there do not exist direct observations of Oort cloud objects. However, along with their large semi-major axes that indicate they originate from much farther than the Kuiper belt, the orbits of the LPCs have randomly distributed inclinations. The isotropic nature of their inclinations shows that, prior to becoming a comet, the LPCs were not from a source that was largely constrained to the ecliptic, like the Kuiper belt. The Oort cloud is predicted to begin $\sim$1000 AU and end $\sim$100,000 AU. This structure of the Kuiper belt and Oort cloud as described in Stern (2003) can be seen in Figure 1.7. These orbital observations of the LPCs suggest the Oort cloud is a spherical structure of small-bodies beyond the Kuiper belt (e.g. Marsden et al. 1978; Wiegert & Tremaine 1999; Królikowska & Dybczyński 2010). Comets have been further categorized with the Tisserand parameter, T_J, which is an invariant value based on the three-body problem involving the comet and the Sun with respect to Jupiter, the most massive and therefore most gravitationally influential planet in the solar system (Levison, 1996). The Tisserand Parameter is described as:

$$T_J = \frac{a_J}{a} + 2\frac{a}{a_J}(1 - e^2)\cos i \tag{1.2}$$

where a, e, and i are the comet's semi-major axis, eccentricity and inclination respectively, and a_J is the semi-major axis of Jupiter. Comets with $2 \leq T_J \leq 3$ are known as Jupiter family comets and are a subset of the ecliptic SPCs. The isotropically distributed LPCs, on the other hand, have $T_J < 2$ (Vaghi, 1973) and semi major axes $a \geq 40$ AU. Halley type comets (HTCs) have also been identified as an intermediate group, which also have a Tisserand parameter $T_J < 2$, but semi-major axes $a < 40$ AU. Additionally, their inclination distribution is distinct from both the SPC and LPC populations.

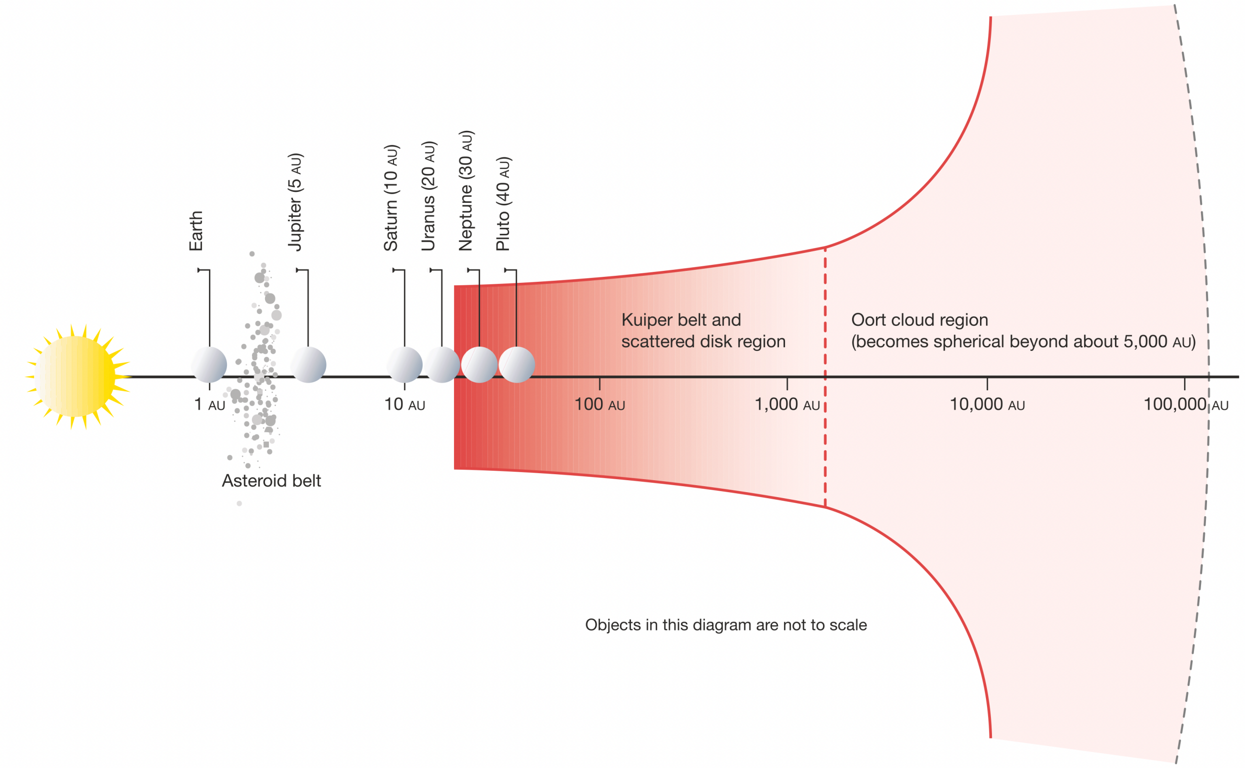

Figure 1.7: Schematic of the Kuiper belt and Oort cloud - The Kuiper belt begins just beyond the orbit of Neptune, ~30 AU, and most of its mass is estimated to existed between ~30 and ~50 AU, as indicated by the red shading in the diagram. It is difficult to predict the location and size of the Oort cloud, as the distant, faint bodies have never been directly observed, but is estimated to begin around ~1000 AU and end around ~100,000 AU. The Oort cloud disperses from the ecliptic with distance, eventually forming a spherical cloud towards the edge. Figure from Stern (2003).

1.2.2 Defining Fragmented Comets

Comets are widely recognized as the carriers of the most primitive, volatile-rich materials. When in the terrestrial planet region, comets quickly lose their material by sublimation. Observations suggest that fragmentation plays a central (possibly even leading) role in the destruction of cometary nuclei. Fragmented comets possess at least two pieces, a primary and a secondary. The primary contains the nucleus of the comet and therefore tends to remain intact longer than the secondary (Sekanina, 1981). The secondary can have a variable lifetime based on its size and composition. The primary is likely to experience multiple fragmentation events in its lifetime (Chen and Jewitt, 1994). Examples of fragmented comets (and one example of a fragmented asteroid) are displayed in Figure 1.8. It is possible that these fragmentation events lead to the eventual destruction of the comet nucleus. Comet fragmentation could be the main process of mass loss during the lifetime of the body with multiple fragmentation events ultimately leading to the destruction of the comet nucleus (Chen and Jewitt, 1994). Observation of a fragmented comet often occurs by chance due to the unpredictable nature of fragmentation events. The secondary fragments tend to be much fainter than the primary (nucleus) of the comet and are short-lived (Meech et al. 1995). For these reasons, fragmented comets are not well observed and the fragmentation mechanisms are therefore difficult to interpret and predict.

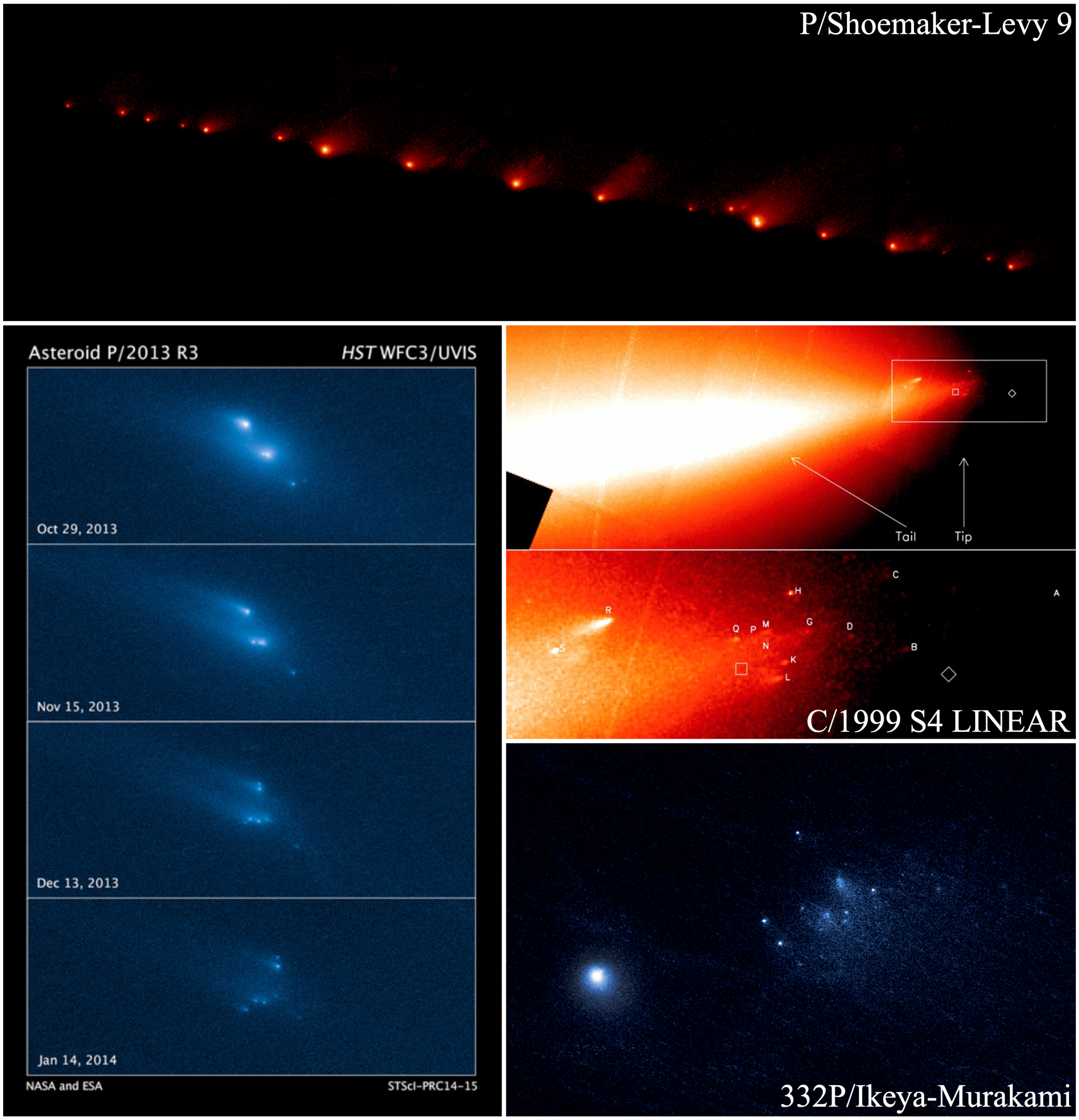

Figure 1.8: Examples of Fragmented Bodies - Top: Hubble Space Telescope (HST) image of comet P/Shoemaker-Levy 9 taken on May 17, 1994 with the Wide Field Planetary Camera 2 (WFPC2) by H. Weaver and E. Smith. Left: HST images of asteroid P/2013 R3 taken October 2013 through January 2014 with the Wide Field Camera 3 (WFC3) by D. Jewitt. Middle right: Adapted from (Weaver et al. 2001). HST images of comet C/1999 S4 LINEAR taken in August 2000 with the WFPC2. Bottom right: HST image of comet 332P/Ikeya-Murakami (P/2010 V1) taken in January 2016 with the WFC3 by D. Jewitt.

1.2.3 Fragmentation Mechanisms

Potential fragmentation mechanisms include tidal, rotational, thermal, outgassing pressure, and impact-induced fragmentation (Boehnhardt, 2004 and Sekanina, 1997). Tidal induced fragmentation is caused by a comet passing by a large enough mass that the gravitational gradient force exerted on the comet is greater than the cohesive strength of the comet material (Boehnhardt, 2004). The buildup of stress to achieve breakup is simplified and illustrated by Asphaug and Benz (1996) in Figure 1.9. Shoemaker-Levy 9 is one of the most spectacular examples of a comet that split into many fragments due to tidal interactions with Jupiter and eventually faced its demise by crashing into the planet (Weaver et al. 1995). Other mechanisms are more difficult to identify and the final fragmentation of a comet could be due to a combination of these mechanisms. For example, a comet could be weakened by its own rotational instability, but ultimately fragment due to internal pressure from outgassing as the comet's volatiles are sublimated (Samarasinha, 2001). However, it is observationally impossible to understand the sequence of events that occurred internally before fragmentation. The fragments provide some insight however, as they reveal the composition inside the nucleus. C/1999 S4 LINEAR and 73P/Schwassmann-Wachmann 3 (73P hereafter) both fragmented into many pieces allowing for this type of analysis. However, Weaver et al. (2001) found that C/1999 S4 LINEAR lacked the volatiles required to have undergone a significant outgassing process, and Dello Russo et al. (2007) found the same for 73P. This absence of volatiles could also be a result of observing the nucleus after the volatiles had sublimated. Therefore, the fragmentation mechanism still remained unclear.

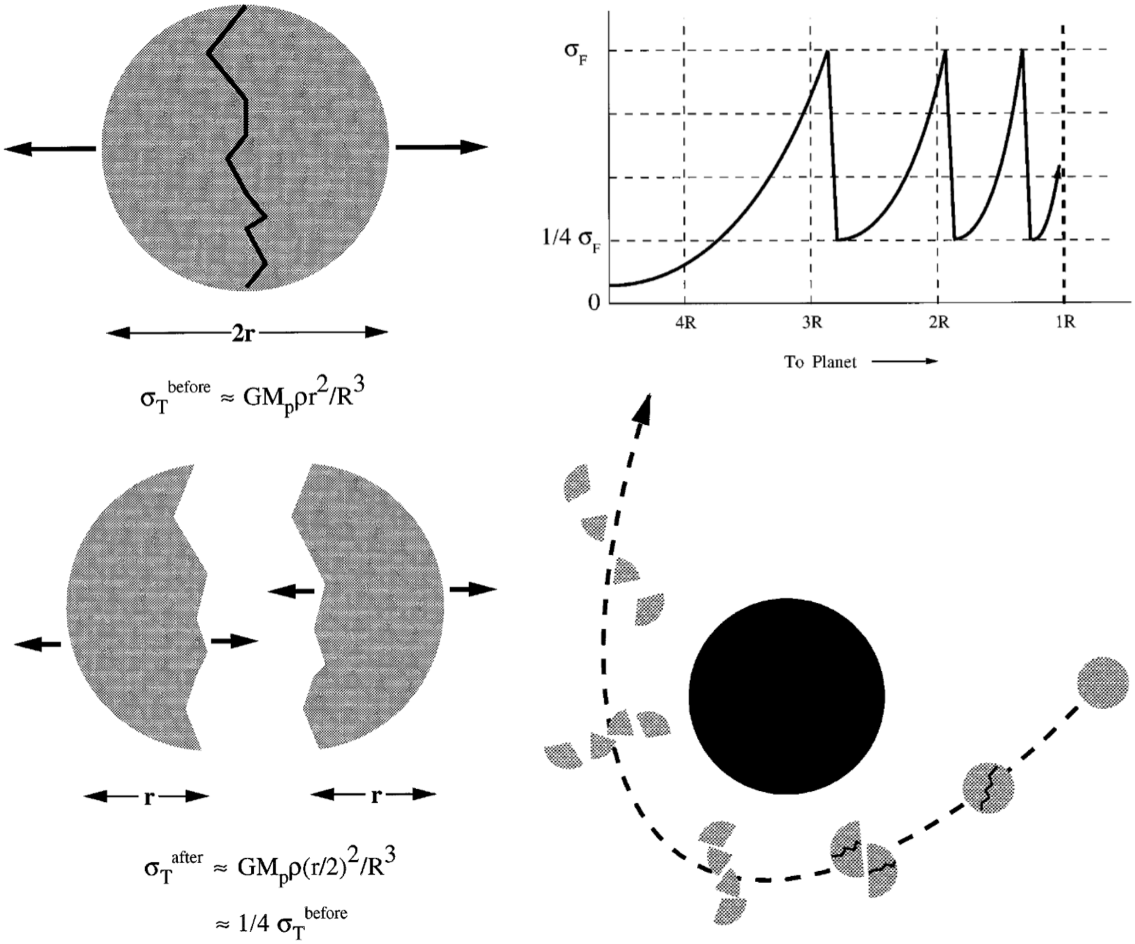

Figure 1.9: Tidal Fragmentation - A simplified illustration of tidal stress on a small body. Left: Illustration of stress, σ_T, on a sphere with radius, r, and density, ρ, due to the gravity of a larger body of mass M_p and radius R. G is the Gravitational constant. Top right: Graph of distance vs. stress. The stress drops each time the small body breaks apart, and grows again as the body approaches the larger mass as illustrated in the bottom right. Figure adapted from Asphaug and Benz (1996).

Recent studies have showed that rotational instability is proving to be a potentially dominating mass-loss mechanism for small bodies. For example, rotational instability has most recently been speculated to cause the fragmentation, outbursts, or disintegration of small bodies such as comets 332P/Ikeya-Murakami (Jewitt et al. 2016) and C/2019 Y4 (ATLAS) (Ye et al. 2021), interstellar comet 2I/Borisov (Jewitt et al. 2020), and active asteroids 6478 Gault (Jewitt et al. 2019) and 331P/Gibbs (Jewitt et al. 2021). There are several mechanisms that can cause spin-up to rotational instability. In general, outgassing can cause non-gravitational forces that result changes in the motion of the orbit of active small bodies, and can also affect their spin evolution (Whipple, 1950; Sekanina, 1981; Jewitt, 1997). As gas expands and is expelled from the body upon sublimation, a force is applied to a the body. This non-gravitational force has been measured for many comets and asteroids (for example: Szutowicz et al. 2008; Hui & Jewitt, 2017). Anisotropic outgassing then contributes to changes in spin due to the application of a torque on the body. Jewitt (2021) showed that these torques result in a spin-up timescale,

$$\tau_s \propto r_n^2/(f_A k_T P) \tag{1.3}$$

where r_n is the radius of a cometary nucleus, f_A is the active fraction on the surface of the nucleus, k_T is the dimensionless moment arm ($k_T = 0$ represents no applied torque and $k_T = 1$ would be representative of a tangential ejection jet), and P is rotational period of the nucleus. This dependence implies that small nuclei ($r_n < 1$ km) are quickly destroyed due to spin-up (Jewitt, 2021). We can then expect spin-up to lead to rotational instability, potentially resulting in the fragmentation of nuclei (Rafikov, 2018). This is supported by the recent observations of disintegration and fragmentation listed above.

On bodies that lack ice, like expected for the case of active asteroid 6478 Gault, rotational instability may be achieved through spin-up by the Yarkovsky-O'Keefe-Radzievskii-Paddack (YORP) effect. The YORP effect describes the spin-up of a small body because of the force due to the scattering of solar radiation and the emission of thermal radiation (Radzievskii, 1954; Paddack, 1969; 1973; Paddack and Rhee 1975; O'Keefe, 1976; Komarov and Sazanov 1994). This spin-up is simply illustrated in Figure 1.10. On an irregularly shaped, rotating body, this force applies a torque and cause spin-up on a timescale,

$$\tau_Y \propto r_n^2 r_h^2 \tag{1.4}$$

where r_h is the distance to the Sun. It is worth noting that, in the case of the active asteroids, it is possible that the activity seen is due to exposure of even a small amount of volatiles, which could then be the dominating factor causing spin-up over YORP (Jewitt 2021).

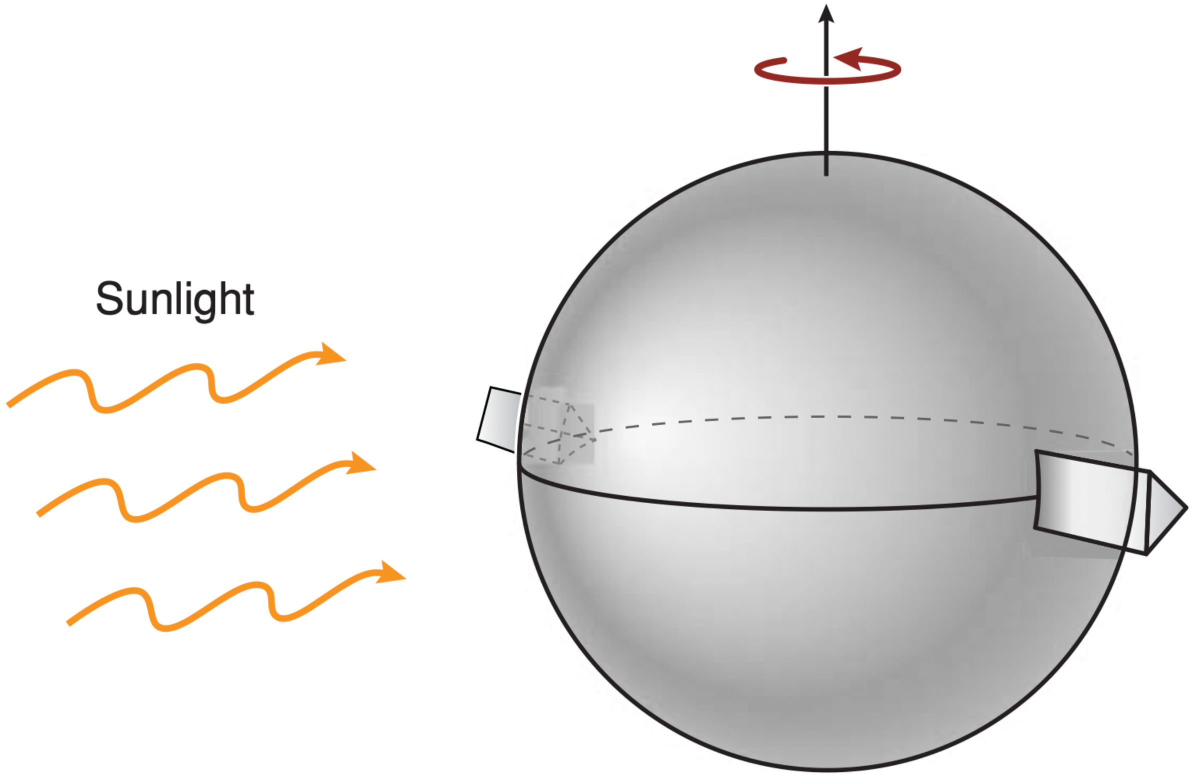

Figure 1.10: YORP Effect - An illustration on the YORP effect on a small, irregularly shaped body. Adapted from by Bottke et al. (2006).

Additionally, we consider fragmentation mechanism caused by thermal effects with high scrutiny, as most fragmentation events are concentrated at small heliocentric distances, when the comets are near perihelion and thus experiencing the highest temperatures they will experience along their orbits (Sekanina, 1981; Boehnhardt, 2004). However, comets are observed to fragment at large heliocentric distances as well, and there appears to be no preference for fragmentation events to occur pre- versus post-perihelion passage. These observations are exemplified in Figure 1.11. Also, according to the Deep Impact and Rosetta missions, it appears that the conductivity of a cometary nucleus is low relative to other solar system bodies (Sunshine et al. 2007; Groussin et al. 2007; 2019). A low thermal conductivity implies a small diurnal skin depth. Transporting heat is therefore thought to be very ineffective on cometary nuclei, and it seems unlikely for thermal stress to build enough to cause a fragmentation event. This may also imply that there is still much mystery surrounding the structure of a cometary nucleus, as perhaps this inefficiency could be overcome at localized structures on the nuclei where heat is more efficiently transported (Fernández, 2009).

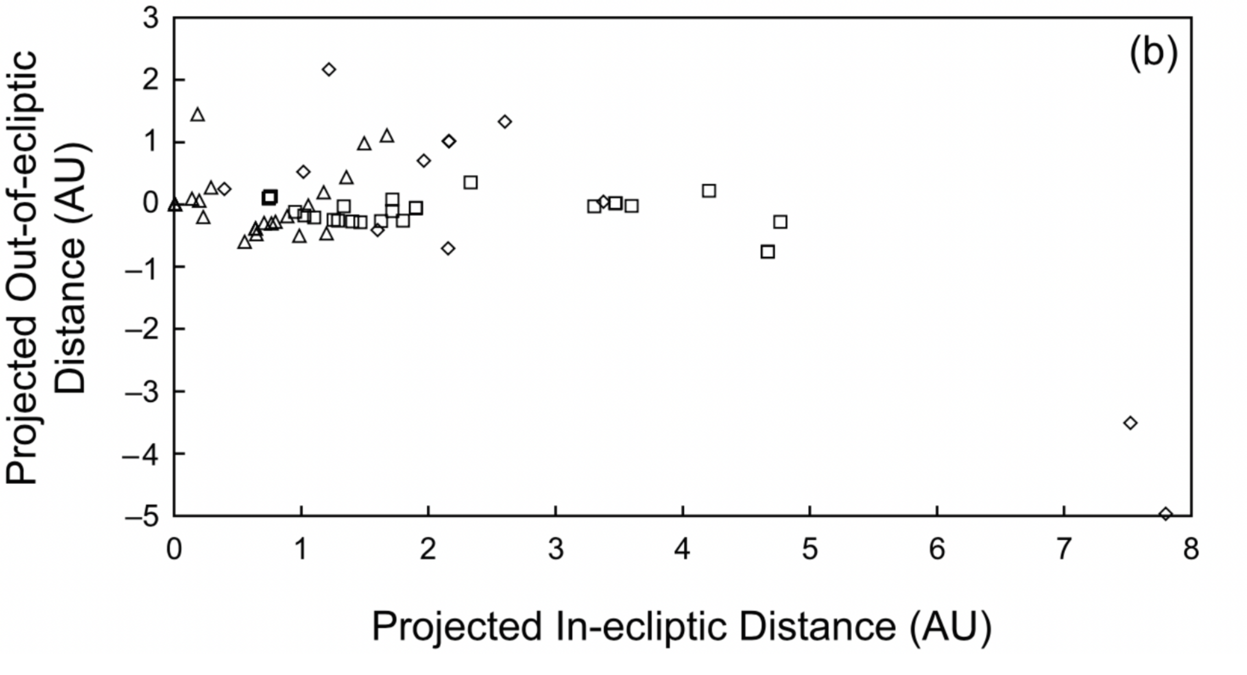

Figure 1.11: Comet Fragmentation Locations. Figure from Boehnhardt (2004).

At large heliocentric distances, beyond the water ice line $\sim 5-6$ AU (Whipple, 1950; Meech and Svoren, 2004), a process other than water ice sublimation must dominate activity. One mechanism for this is the sublimation of supervolatile ices such as carbon monoxide or carbon dioxide. This sublimation can lead to the build up of pressure until potential fragmentation. The flux of sublimation of various cometary volatiles can be estimated based on heliocentric distance with the radiative thermal equilibrium equation. Ignoring the conduction of heat to the interior of the comet, the power absorbed from the Sun is set equivalent to the power radiated into space and the power used to sublimate the ice as follows:

$$\frac{L_{\odot}}{4\pi r_H^2}(1-A) = \chi[\epsilon\sigma\ T^4 + L(T)f_s(T)] \tag{1.5}$$

where $L_{\odot}$ is the luminosity of the Sun in W, r_H is the heliocentric distance in m, A is the Bond albedo, ϵ is the emissivity of the comet, σ is the Stefan-Boltzmann constant with units W m^{-2} K^{-4}, $L(T)$ (J kg^{-1}) is the latent heat of sublimation of the volatile in question at temperature T in K, and $f_s(T)$ is the mass flux of the sublimated ice in kg m^{-2} s^{-1}. The value of χ can range from $\chi = 1$, which would represent the highest temperatures found at the subsolar point of a non-rotating nucleus, and $\chi = 4$ represented the temperature on a rotating, isothermal sphere. Figure 1.12 displays the results for the hot ($\chi = 1$) and cold ($\chi = 4$) sublimation fluxes as they vary with heliocentric distance for H_2O, CO_2, and CO using the latent heat of each volatile as reported by Brown & Ziegler (1980) and Washburn (1962), and assuming an albedo $A = 0.04$ and an emissivity $e = 0.9$ (Jewitt et al. 2017). This figure is useful, not only to estimate whether water ice could be the driver of activity in a comet, but also to estimate the level of expected activity given a certain volatile present at a given heliocentric distance. This can help determine whether gas build-up could potentially build up enough stress on a comet to cause fragmentation.

Another thermally driven mechanism for distant activity is the runaway crystallization of amorphous ice. At the low temperatures and pressures where comets form, Bar-Nun et al. (1985; 1986) demonstrated that ice takes an amorphous state. In this state, gas is trapped and subsequently released when the ice is heated to the point of crystallization, which is also an exothermic process (Prialnik & Bar-Nun 1990). To estimate the location where the crystallization of water ice can begin on a body in the solar system, the timescale of crystallization needs to be much lower than the free-fall timescale of the comet. Jewitt (2017) found that this is satisfied at the hot temperature limit ($\chi = 1$) at a heliocentric distance $r_H \leq 12.5$ AU, and satisfied at the cold limit ($\chi = 4$) at $r_H \leq 6.0$ AU. This is represented with yellow shading in Figure 1.12. The deeper the yellow shading, the more likely it is that crystallization of amorphous water ice can begin, according to the timescale and radiative thermal equilibrium calculations described above.

It is important to note that there are no direct observations of the crystallization of amorphous ice in comets. Despite the challenges presented by the effectiveness of these thermal processes to lead to a fragmentation event, thermal processes dominate cometary activity, so it is expected that outbursts and fragmentation events can be caused thermally as well, as supported by fragmentation events largely occurring near perihelion (Boehnhardt, 2004). There are also observations of repeated outbursts occurring in a comet over several apparitions such as 73P, which has repeatedly fragmented near perihelion (Crovisier et al. 1995; Fuse et al. 2007; Weaver et al. 2008). This does not confirm that thermal stress is the cause of fragmentation events of 73P, however it shows that thermal processes are worth considering along with non-thermal processes.

Chapters 3 and 4 investigate the 2006 fragmentation events of Comet 73P. In particular we examine the nucleus in Chapter 3 and two secondary fragments in Chapter 4.

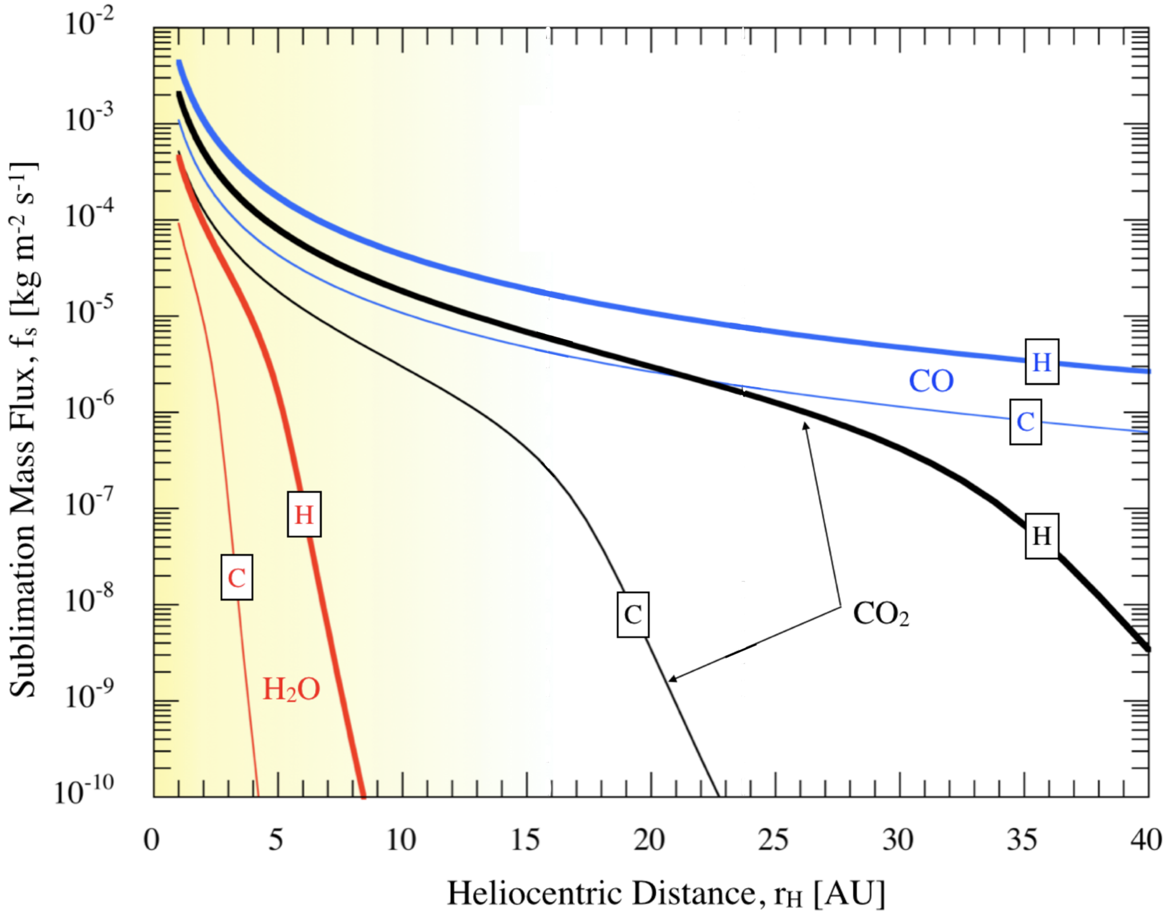

Figure 1.12: Sublimation Flux and H_2O Ice Crystallization with Heliocentric Distance - the hot and cold limits on the sublimation mass flux with heliocentric distance for H_2O, CO_2, and CO with heliocentric distance are labeled as "H" and "C" respectively. The yellow shading represents heliocentric distances where crystallization of water ice can begin. The deeper yellow color indicates a higher likelihood that crystallization can occur. Figure adapted from Jewitt et al. (2017).

REFERENCES

[1] Asphaug, E. & Benz, W. 1996, Icarus, 121, 225

[2] Bar-Nun, A., Herman, G., Laufer, D., et al. 1985, Icarus, 63, 317

[3] Bar-Nun, A., Prialnik, D., Laufer, D., et al. 1986, BAAS

[4] Benner, L. A. M. & McKinnon, W. B. 1995, Icarus, 114, 1

[5] Boehnhardt, H. 2004, Comets II, 301

[6] Bottke, W. F., Nesvorný, D., Vokrouhlický, D., et al. 2010, AJ, 139, 994

[7] Brown, G. N., Ziegler, W. T. 1980, Advances in Cryogenic Engineering, 662-670

[8] Canup, R. M. & Ward, W. R. 2002, AAS/Division of Dynamical Astronomy Meeting #33

[9] Carruba, V., Burns, J. A., Nicholson, P. D., et al. 2002,

[10] Carusi, A. & Valsecchi, G. B. 1979, Asteroids, 391

[11] Chen, J. & Jewitt, D. 1994, Icarus, 108, 265

[12] Colombo, G. & Franklin, F. A. 1971, Icarus, 15, 186

[13] Crovisier, J., Biver, N., Bockelee-Morvan, D., et al. 1995, IAU Circ., 6227

[14] Dello Russo, N., Vervack, R. J., Weaver, H. A., et al. 2007, Nature, 448, 172

[15] Dell'Oro, A., PAolicchi, F., Marzari, P., et al. 1998, A&A, 339, 272

[16] Dones, L. Weissman, P. R. Levison, H. F. et al. 2004, Comets II, 153

[17] Duncan, M. Quinn, T. & Tremaine, S. 1987, AJ, 94, 1330

[18] Fernández, Y. R. 2009, Planet. Space Sci., 57, 1218

[19] Fuse, T., Yamamoto, N., Kinoshita, D., et al. 2007, PASJ, 59, 381

[20] Graykowski, A. & Jewitt, D. 2018, AJ, 155, 184

[21] Graykowski, A. & Jewitt, D. 2019, AJ, 158, 112

[22] Groussin, O., A'Hearn, M. F., Li, J.-Y., et al. 2007, Icarus, 191, 63

[23] Groussin, O., Attree, N., Brouet, Y., et al. 2019, Space Sci. Rev., 215, 29

[24] Heisler, J. & Tremaine, S. 1986, Icarus, 65, 13

[25] Heppenheimer, T. A. & Porco, C. 1977, Icarus, 30, 385

[26] Hui, M.-T. & Jewitt, D. 2017, AJ, 153, 80

[27] Jewitt, D. 1997, Earth Moon and Planets, 79, 35

[28] Jewitt, D. & Haghighipour, N. 2007, ARA&A, 45, 261

[29] Jewitt, D., Hui, M.-T., Kim, Y., et al. 2020, ApJ, 888, L23

[30] Jewitt, D., Hui, M.-T., Mutchler, M., et al. 2017, ApJ, 847, L19

[31] Jewitt, D., Kim, Y., Luu, J., et al. 2019, ApJ, 876, L19

[32] Jewitt, D., Li, J., & Kim, Y. 2021, AJ, 162, 268

[33] Jewitt, D. & Luu, J. 1993, Nature, 362, 730.

[34] Jewitt, D., Mutchler, M., Weaver, H., et al. 2016, ApJ, 829, L8

[35] Jewitt, D. & Sheppard, S. 2005, Space Sci. Rev., 116, 441

[36] Jewitt, D. C., Trujillo, C. A., & Luu, J. X. 2000, AJ, 120, 1140.

[37] Kary, D. M. & Dones, L. 1996, Icarus, 121, 207

[38] Komarov, M. M., Sazanov, V. V. 1994, Sol. Syst. Res, 28, 16-23

[39] Królikowska, M. & Dybczyński, P. A. 2010, MNRAS, 404, 1886

[40] Levison, H. F. 1996, Completing the Inventory of the Solar System, 107, 173

[41] Levison, H. F. & Duncan, M. J. 1997, Icarus, 127, 13

[42] Lunine, J. I. & Stevenson, D. J. 1982, Icarus, 52, 14

[43] Marsden, B. G., Sekanina, Z., & Everhart, E. 1978, AJ, 83, 64

[44] Marzari, F., Scholl, H., & Farinella, P. 1996, Icarus, 119, 192

[45] Meech, K. J., Knopp, G. P., Farnham, T. L., et al. 1995, Icarus, 116, 46

[46] Meech, K. J. & Svoren, J. 2004, Comets II, 317

[47] Morbidelli, A. Levison, H. F. Tsiganis, K. et al. 2005, Nature, 435, 462

[48] Mosqueira, I. & Estrada, P. R. 2003, Icarus, 163, 198

[49] Nesvorný, D., Alvarellos, J. L. A., Dones, L., et al. 2003, AJ, 126, 398

[50] Nesvorný, D., Vokrouhlický, D., & Morbidelli, A. 2007, AJ, 133, 1962

[51] Nesvorný, D. Vokrouhlicý, D. Morbidelli, A. 2013, , 768, 45

[52] Nicholson, P. D., Cuk, M., Sheppard, S. S., et al. 2008, The Solar System Beyond Neptune, 411

[53] Okeefe, J. A. 1976, NASA STI/Recon Technical Report A, 77, 14534

[54] Paddack, S. J. & Rhee, J. W. 1976, Interplanetary Dust and Zodiacal Light, 453

[55] Pollack, J. B., Burns, J. A., & Tauber, M. E. 1979, Icarus, 37, 587

[56] Prialnik, D. & Bar-Nun, A. 1990, ApJ, 363, 274

[57] Radzievskii, V. V. 1954, Dissertation State Astronomical Observatory

[58] Rafikov, R. R. 2018, ApJ, 867, L17

[59] Samarasinha, N. H. 2001, Icarus, 154, 540

[60] Sekanina, Z. 1981, Annual Review of Earth and Planetary Sciences, 9, 113

[61] Sekanina, Z. 1997, A&A, 318, L5

[62] Sheppard, S. S. & Jewitt, D. C. 2003, Nature, 423, 261

[63] Stern, S. A. 2003, Nature, 424, 639

[64] Sunshine, J. M., Groussin, O., Schultz, P. H., et al. 2007, Icarus, 190, 284

[65] Szutowicz, S., Królikowska, M., & Rickman, H. 2008, A&A, 490, 393.

[66] Tremaine, S. 1993, Planets Around Pulsars, 36, 335

[67] Vaghi, S. 1973, A&A, 24, 41

[68] Washburn, E. 1926, International Critical Tables of Numerical Data, Physics, Chemistry and Technology, Vol. 3 (New York: McGraw-Hill)

[69] Weaver, H. A., A'Hearn, M. F., Arpigny, C., et al. 1995, Science, 267, 1282

[70] Weaver, H. A., Lisse, C. M., Mutchler, M., et al. 2008, Asteroids, Comets, Meteors 2008, 1405, 8248

[71] Weaver, H. A., Sekanina, Z., Toth, I., et al. 2001, Science, 292, 1329

[72] Whipple, F. L. 1950, ApJ, 111, 375

[73] Wiegert, P. & Tremaine, S. 1999, Icarus, 137, 84

[74] Ye, Q., Jewitt, D., Hui, M.-T., et al. 2021, AJ, 162, 70

CHAPTER 2

Colors and Shapes of the Irregular Planetary Satellites

This chapter is adapted from the peer-reviewed paper titled "Colors and Shapes of the Irregular Planetary Satellites", which has been published in the Astronomical Journal (Graykowski & Jewitt 2018).

2.1 Introduction

It is widely recognized that the irregular satellites of the giant planets were captured from initially heliocentric orbits. However, the mechanism of capture and the source region from which they were captured both remain unknown. We present an optical color survey of 43 irregular satellites of the outer planets conducted using the LRIS camera on the 10-meter telescope at the Keck Observatory in Hawaii. The measured colors are compared to other planetary bodies in search for similarities and differences that may reflect upon the origin of the satellites. We find that ultrared matter (with color index B-R ≥ 1.6), while abundant in the Kuiper belt and Centaur populations, is depleted from the irregular satellites. We also use repeated determinations of the absolute magnitudes to make a statistical estimate of the average shape of the irregular satellites. The data provide no evidence that the satellites and the main-belt asteroids are differently shaped, consistent with collisions as the major agent shaping both. In the present paper we present measurements of the magnitudes and colors of 44 irregular satellites of the four giant planets taken using the Keck I 10 m telescope. The number of irregular satellites observed at each giant planet in this survey are listed in Table 2.1). The new data are compared with published measurements of smaller samples (Grav et al. 2003, 2004, Grav and Bauer 2007, Rettig et al. 2001)

Planet	# iSats	# iSats in this Survey
Jupiter	71	20
Saturn	53	14
Uranus	9	6
Neptune	7	3
Total	140	43

Table 2.1: Number of Irregular Satellites in This Survey

2.2 Observations

The data were collected over nine nights between 2008 March and 2015 December at the W. M. Keck Observatory on Maunakea, Hawaii using the LRIS instrument on the 10 meter Keck I telescope (Oke et al. 1995, Table 2.2). The data used were all taken under photometric conditions with the telescope tracked at non-sidereal rates to follow the motion of each satellite. Most satellites were observed on multiple nights in order to check for repeatability of the measurements. We used the B, V, and R filters, for which the central wavelengths, λ_c, and full-widths at half maxima, FWHM, are B (4370Å, 878Å), V (5473 Å, 948 Å) and R (6417 Å, 1185 Å). The images were flat-fielded using composites of images recorded from an illuminated patch inside the Keck dome and photometrically calibrated using observations of stars with Sun-like colors from Landolt (1992).

Using IRAF, the images were reduced and aperture photometry was obtained using the APPHOT package. By trial and error, we used a photometry annulus with radius 1.35-2.03$''$, depending on the seeing, and obtained an estimate of the sky background from a contiguous annulus 1.35$''$ wide. For very faint satellites, we used two-aperture photometry.

With this method, we chose a small aperture based on the FWHM of the object, and used it to measure the targeted satellite as well as brighter field stars. Then we chose a larger aperture in order to measure the total flux from the selected field stars. We calculated the fraction of light that was left out of the measurement from the smaller aperture, and used it to correct the magnitude of the satellite to obtain its apparent magnitude. We observed satellites with apparent magnitude, R, as bright as ∼17.5 and as faint as ∼25.0 magnitude. To show the visual difference of this magnitude range, Figure (2.1) compares an image of a faint (∼23.6) and a bright (∼17.5) satellite observed in this work.

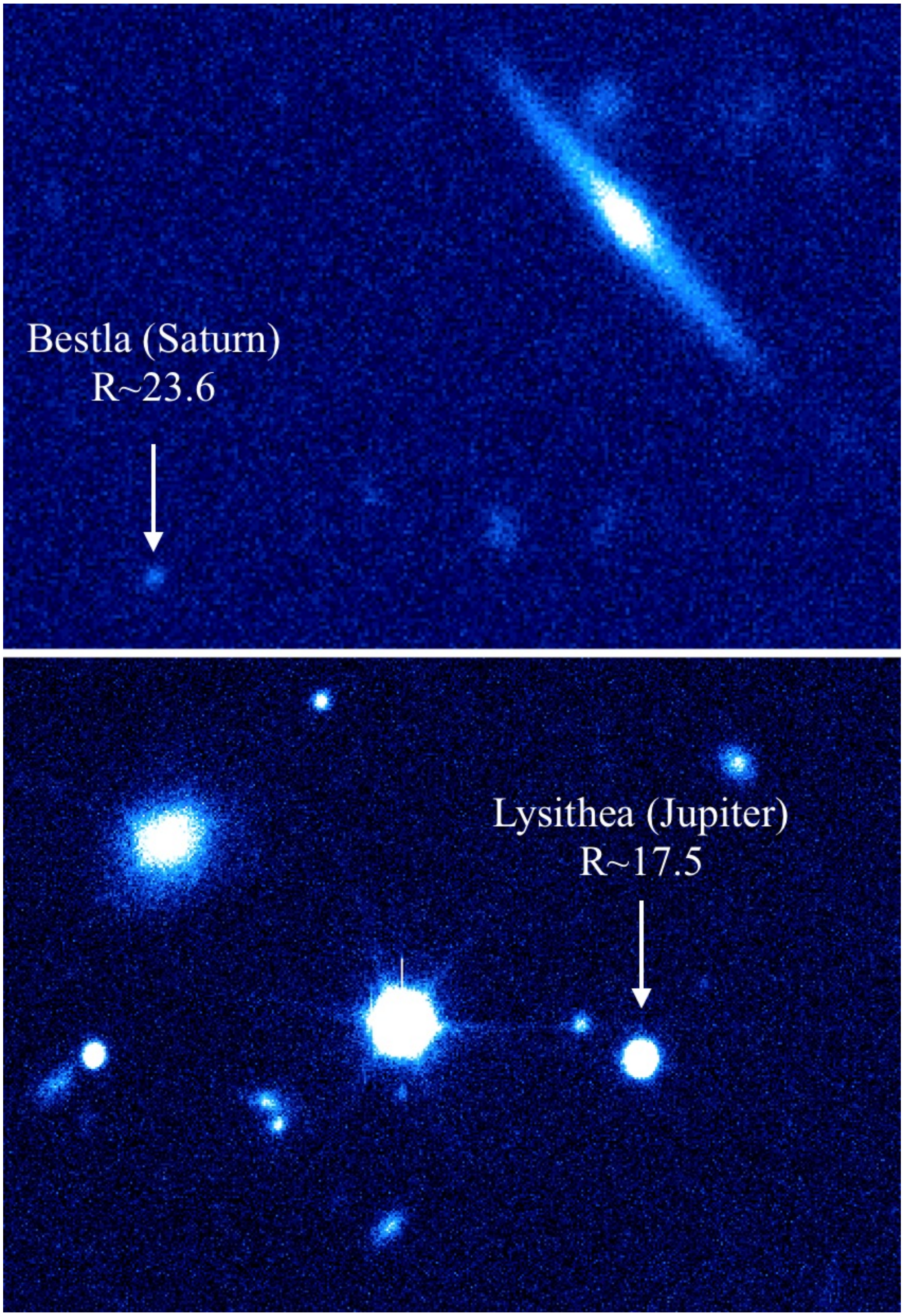

Figure 2.1: Bestla and Lysithea - Sample images of irregular satellites (top) Bestla, a faint irregular satellite of Saturn (bottom) Lysithea, a bright irregular satellite of Jupiter.

Satellite	UT Date and Time[a]	r_H (AU)b	Δ (AU)[c]	α ($\circ$)[d]	R[e]	B-V	V-R	B-R
Jupiter								
JIX Sinope	2008 Sep 30 05:43-05:48	5.00	4.80	11.50	18.42 ± 0.07	0.77 ± 0.08	0.48 ± 0.10	1.25 ± 0.08
JX Lysithea	2008 Sep 30 05:20-05:30	5.04	4.04	1.36	17.50 ± 0.01	0.72 ± 0.01	0.40 ± 0.01	1.12 ± 0.01
JXI Carme	2008 Sep 30 05:35-05:43	5.04	4.85	11.41	17.92 ± 0.07	0.76 ± 0.08	0.48 ± 0.08	1.24 ± 0.05
JXIII Leda	2009 Aug 19 07:28-07:43	5.05	4.04	1.32	19.03 ± 0.01	0.69 ± 0.01	0.36 ± 0.01	1.05 ± 0.01
	2009 Aug 21 13:37-13:44	5.05	4.05	1.89	18.84 ± 0.01	...	...	1.20 ± 0.02
JXVIII Themisto	2008 Sep 30 05:50-06:05	5.07	4.06	1.03	19.48 ± 0.01	0.79 ± 0.02	0.52 ± 0.02	1.32 ± 0.01
	2008 Sep 30 06:25-06:36	5.06	4.06	1.54	19.78 ± 0.04	...	...	0.83 ± 0.04
	2009 Aug 19 07:43-07:49	5.06	4.06	1.57	19.45 ± 0.05	...	...	1.22 ± 0.06
	2009 Aug 21 07:14-70:28	5.06	4.06	1.60	19.58 ± 0.01	...	...	1.31 ± 0.01
JXIX Megaclite	2009 Aug 19 09:49-09:55	5.15	4.14	1.25	21.55 ± 0.01	0.81 ± 0.07	0.44 ± 0.07	1.26 ± 0.02
	2009 Aug 21 07:28-07:32	5.15	4.15	1.77	21.52 ± 0.04	...		1.23 ± 0.07
	2009 Aug 21 10:33-10:43	5.15	4.15	1.79	21.76 ± 0.01	...		0.92 ± 0.03
	2009 Aug 21 11:09-11:19	5.15	4.15	1.81	21.76 ± 0.02	...	...	1.38 ± 0.05
JXX Taygete	2009 Aug 19 07:57-08:06	5.08	4.07	0.86	21.88 ± 0.02	0.77 ± 0.03	0.48 ± 0.02	1.26 ± 0.03
	2009 Aug 21 13:26-13:37	5.08	4.08	1.41	21.95 ± 0.01	...	...	1.35 ± 0.03
JXXI Chaldene	2009 Aug 19 08:16-08:27	5.06	4.05	0.57	22.19 ± 0.01	0.82 ± 0.05	0.50 ± 0.05	1.32 ± 0.03
JXXII Harpalyke	2009 Aug 19 08:59-09:08	4.92	3.91	1.30	22.02 ± 0.02	0.70 ± 0.02	0.42 ± 0.03	1.12 ± 0.02
JXXIII Kalyke	2009 Aug 19 09:17-09:27	5.15	4.14	0.67	21.61 ± 0.02	0.69 ± 0.03	0.46 ± 0.03	1.15 ± 0.03
JXXIV Iocaste	2009 Aug 19 09:36-09:42	4.93	3.92	0.95	21.72 ± 0.03	0.86 ± 0.08	0.38 ± 0.07	1.24 ± 0.05
JXXV Erinome	2009 Aug 21 12:06-12:13	4.89	3.89	1.45	22.11 ± 0.04	0.72 ± 0.01	0.43 ± 0.04	1.14 ± 0.04
JXXVI Isonoe	2009 Aug 19 10:59-11:16	5.14	4.14	1.46	22.63 ± 0.04	0.78 ± 0.05	0.53 ± 0.04	1.31 ± 0.06
JXXVII Praxidike	2009 Aug 19 11:16-11:36	4.93	3.92	1.10	21.48 ± 0.03	0.71 ± 0.05	0.32 ± 0.05	1.03 ± 0.03
JXXVIII Autonoe	2009 Aug 19 11:36-11:58	4.97	3.96	1.32	21.74 ± 0.02	0.81 ± 0.02	0.48 ± 0.03	1.29 ± 0.03
	2009 Aug 21 10:12-10:22	4.96	3.96	1.83	21.70 ± 0.03	...	...	1.25 ± 0.04
	2009 Aug 21 11:26-11:39	4.96	3.96	1.84	21.76 ± 0.03	...	...	1.15 ± 0.06
	2009 Aug 21 12:20-12:42	4.96	3.96	1.86	21.79 ± 0.02	0.73 ± 0.14	0.50 ± 0.07	1.22 ± 0.12
JXXIX Thyone	2009 Aug 19 11:58-12:28	5.12	4.11	0.90	22.10 ± 0.03	0.71 ± 0.06	0.46 ± 0.04	1.16 ± 0.05
JXXX Hermippe	2009 Aug 19 12:28-12:49	5.03	4.03	0.93	21.59 ± 0.03	0.72 ± 0.05	0.49 ± 0.04	1.22 ± 0.06
JXVII Callirrhoe	2009 Aug 19 13:21-13:30	5.16	4.15	1.20	20.90 ± 0.07	0.80 ± 0.11	0.24 ± 0.12	1.04 ± 0.08

JXLVII Eukelade	2009 Aug 21 12:52-13:20	4.94	3.94	1.25	21.79 ± 0.02	0.78 ± 0.07	0.50 ± 0.07	1.29 ± 0.02
JXLVIII Cyllene	2009 Aug 21 11:39-12:06	5.03	4.02	1.51	22.35 ± 0.01	0.73 ± 0.07	0.47 ± 0.07	1.19 ± 0.01
Saturn								
SIX Phoebe	2008 Mar 10 09:19-09-27	9.28	8.33	1.89	15.88 ± 0.01	0.58 ± 0.01	0.34 ± 0.01	0.91 ± 0.01
SXXI Tarvos	2008 Mar 10 10:33-11:13	9.25	8.30	1.84	22.28 ± 0.01	0.71 ± 0.04	0.42 ± 0.03	1.13 ± 0.03
SXXII Ijiraq	2008 Mar 11 06:49-07:19	9.31	8.36	1.94	22.73 ± 0.01	...	...	1.40 ± 0.03
SXXVI Albiorix	2008 Mar 10 08:26-09:19	9.25	8.25	0.34	20.43 ± 0.01	0.75 ± 0.02	0.48 ± 0.01	1.23 ± 0.02
	2008 Mar 10 11:13-11:25	9.28	8.33	1.88	20.48 ± 0.03	...	...	1.23 ± 0.06
	2008 Mar 11 06:07-06:28	9.28	8.33	1.96	20.46 ± 0.01	0.91 ± 0.02	0.50 ± 0.02	1.41 ± 0.01
SXXVIII Erriapus	2008 Mar 10 08:11-08:26	9.33	8.34	0.33	22.72 ± 0.02	0.77 ± 0.01	0.42 ± 0.02	1.19 ± 0.02
SXXXI Narvi	2008 Mar 11 06:28-06:33	9.34	8.38	1.81	23.52 ± 0.05	...	...	1.29 ± 0.08
SXXXVII Bebhionn	2008 Mar 10 09:40-10:05	9.30	8.34	1.77	23.78 ± 0.18	0.60 ± 0.10	0.51 ± 0.20	1.12 ± 0.18
	2008 Mar 11 08:40-08:45	9.29	8.34	1.87	23.74 ± 0.02	...	...	1.14 ± 0.05
SXXXVI Aegir	2008 Mar 11 07:19-07:24	9.26	8.14	2.03	24.49 ± 0.06	...	...	1.30 ± 0.06
SXXXVIII Bergelmir	2008 Mar 11 12:33-12:38	9.40	8.45	1.93	24.28 ± 0.04	...	...	1.10 ± 0.15
SXXXIX Bestla	2008 Mar 11 10:15-10:20	9.18	8.24	2.06	23.55 ± 0.03	...	...	1.32 ± 0.04
SXLII Fornjot	2008 Mar 11 08:05-08:10	9.37	8.42	2.02	24.34 ± 0.09	...	...	1.40 ± 0.09
SLII Tarqeq	2008 Mar 11 11:45-11:50	9.34	8.39	1.94	23.12 ± 0.02	...	...	1.23 ± 0.07
S/2007 S02	2008 Mar 11:55-12:30	9.27	8.33	2.01	23.74 ± 0.05	...	...	1.37 ± 0.06
S/2007 S02	2008 Mar 11:55-12:30	9.30	8.40	2.00	23.74 ± 0.05	...	...	1.37 ± 0.09
Uranus								
UXVI Caliban	2008 Sep 05 10:25-11:29	20.15	19.15	0.32	21.98 ± 0.01	0.87 ± 0.03	0.51 ± 0.01	1.39 ± 0.03
	2015 Dec 08 10:01-10:17	19.95	19.44	2.45	22.17 ± 0.01	0.73 ± 0.01	0.43 ± 0.01	1.16 ± 0.01
UXVII Sycorax	2008 Sep 04 11:29-11:47	20.06	19.05	0.08	20.17 ± 0.02	0.77 ± 0.02	0.52 ± 0.02	1.29 ± 0.03
	2008 Sep 05 09:21-10:08	20.06	19.05	0.28	20.24 ± 0.01	0.80 ± 0.01	0.56 ± 0.01	1.37 ± 0.01
	2015 Dec 08 08:16-08:33	20.01	19.48	2.44	20.50 ± 0.01	0.85 ± 0.02	0.53 ± 0.02	1.38 ± 0.01
UXVIII Prospero	2008 Sep 04 11:55-12:11	20.21	19.21	0.32	23.18 ± 0.09	0.62 ± 0.03	0.53 ± 0.09	1.15 ± 0.09
	2008 Sep 30 11:13-11:59	20.21	19.26	0.90	23.26 ± 0.04	0.96 ± 0.08	0.31 ± 0.08	1.26 ± 0.05
	2015 Dec 09 8:08-8:50	20.02	19.53	2.48	23.20 ± 0.01	0.86 ± 0.06	0.67 ± 0.06	1.54 ± 0.02
UXIX Setebos	2008 Sep 05 11:29-12:06	20.16	19.15	0.31	23.17 ± 0.04	0.78 ± 0.02	0.49 ± 0.04	1.27 ± 0.04
UXX Stephano	2008 Sep 04 12:31-13:24	20.15	19.15	0.26	24.03 ± 0.02	0.91 ± 0.12	0.71 ± 0.05	1.62 ± 0.11

	2008 Sep 05 12:12-12:39	20.15	19.15	0.35	23.80 ± 0.05	1.03 ± 0.09	0.61 ± 0.09	1.63 ± 0.07
UXXI Trinculo	2008 Sep 05 13:53-14:22	20.04	19.04	0.34	25.20 ± 0.15	...	...	...
Neptune								
NI Halimede	2008 Sep 04 09:39-10:22	30.06	29.13	0.73	23.72 ± 0.08	0.84 ± 0.18	0.72 ± 0.19	1.57 ± 0.09
	2008 Sep 05 07:47-08:49	30.06	29.13	0.73	24.16 ± 0.08	0.92 ± 0.10	0.38 ± 0.12	1.31 ± 0.09
NII Nereid	2008 Sep 04 06:36-06:57	30.02	29.07	0.66	18.94 ± 0.01	0.65 ± 0.02	0.39 ± 0.01	1.04 ± 0.02
	2008 Sep 05 06:21-06:40	30.02	29.08	0.69	19.04 ± 0.01	0.69 ± 0.01	0.37 ± 0.02	1.06 ± 0.01
NIV Neso	2008 Sep 05 06:45-07:47	30.01	29.07	0.66	24.66 ± 0.04	...	0.84 ± 0.12	...
	2008 Sep 30 08:54-10:12	30.01	29.31	1.38	25.34 ± 0.31	...	0.31 ± 0.42	...

Table 2.2: Irregular Satellite Geometry and Photometry.

[a] UT date and range of start times of the integrations

[b] Heliocentric Distance in AU

[c] Geocentric Distance in AU

[d] Phase Angle in degrees

[e] Apparent magnitude in the R filter

2.3 Results

The results of the photometry are listed in Table 2.2 with $\pm 1\sigma$ standard errors. Not all satellites were observed in all three filters (B, V, and R) and therefore not all have equal numbers of color measurements. In total, we measured 20 Jovian, 14 Saturnian, 6 Uranian, and 4 Neptunian satellites.

The apparent magnitudes were converted to absolute magnitudes, H_V, defined as the magnitude corrected to unit heliocentric and geocentric distance (r_H and Δ, respectively) and to phase angle $\alpha = 0\circ$. For the apparent V magnitude, this correction is

$$H_V = V - 5\log_{10}(r_H \Delta) - \beta\alpha \tag{2.1}$$

where β is the phase function representing the angular dependence of the scattered sunlight on α. For simplicity, we assumed $\beta = 0.04$ magnitudes degree^{-1}, consistent with values measured in low albedo solar system objects (Tedesco and Baker 1981, Jewitt et al. 1998, Rettig et al. 2001). Equivalent relations were also used to compute the absolute B and R filter magnitudes.

Figure (2.2) compares H_V magnitudes from this work with H_V magnitudes from previous surveys by Grav et al. (2003), Grav et al. (2004) and Grav and Bauer (2007). Measurements in perfect agreement should plot on the diagonal line in the figure. Some scatter about the line is expected because of measurement errors, and because each satellite possesses a rotational lightcurve, presenting a variable brightness to the observer. In fact, most satellites fall slightly below the diagonal line, indicating systematic differences between our measurements and those in the literature. Possible reasons for these systematic offsets include slight differences in the filters employed, as well as differences in the way the phase function (Equation 3.2) was treated.

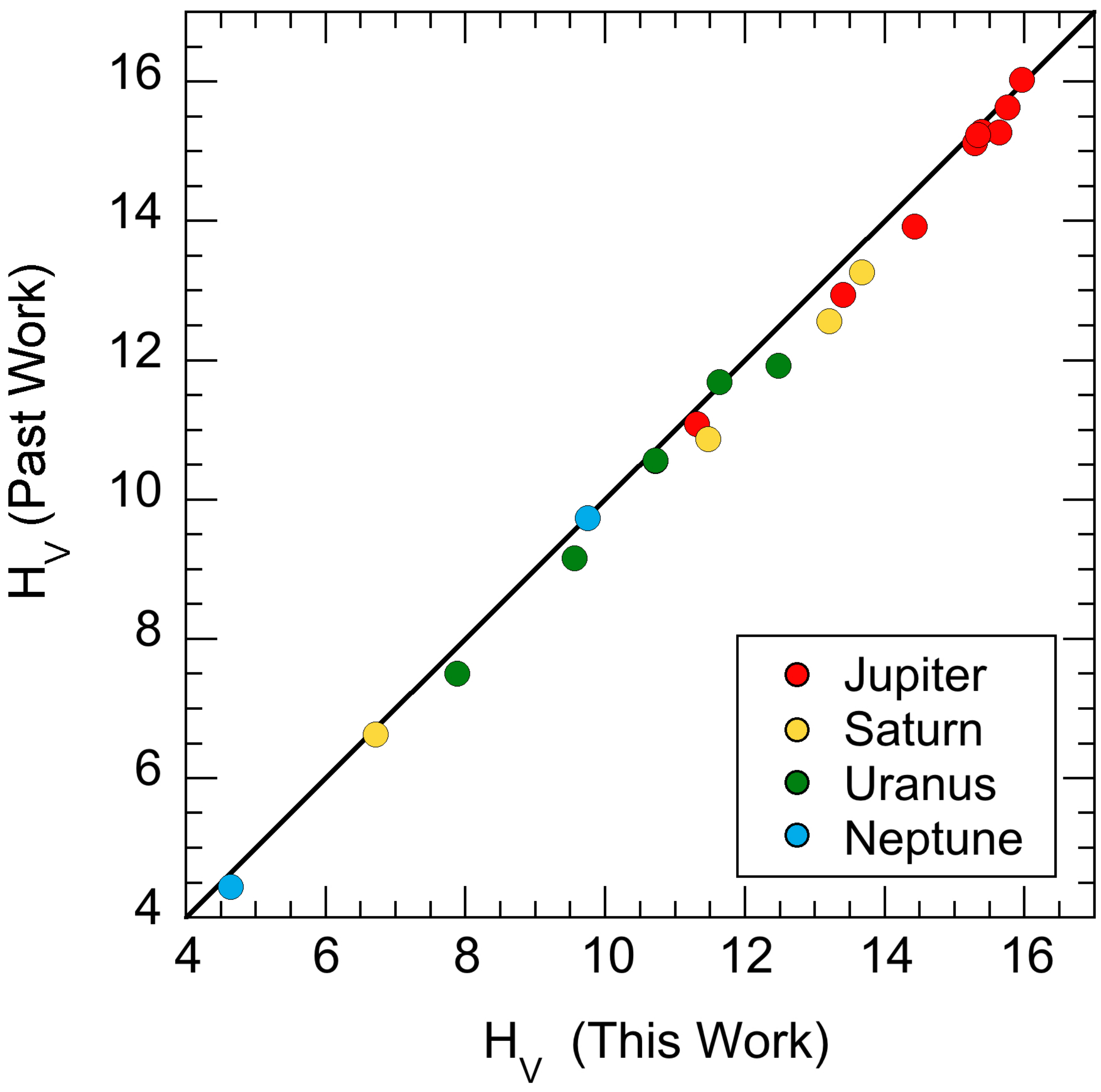

Figure 2.2: H_V values from this survey plotted against H_V values from Grav et al. 2003, 2004 and Grav and Bauer 2007. Only satellites measured in both surveys are plotted. The H_V from other surveys are systematically brighter than the present work.

The major uncertainty in the phase function correction lies in the treatment of the possible opposition surge. For example, Grav et al. (2004) assumed $\beta = 0.38$ magnitudes degree^{-1} for the satellites of Uranus and Neptune in order to account for small-angle brightening. Grav et al. (2003, 2007) and Rettig et al. (2001) instead used the Bowell et al. (1989) phase function with parameter $G = 0.15$, which provides for a more modest surge. Bauer et al. (2006) found that the magnitude of the opposition surge varies widely from satellite to satellite, meaning that we cannot adopt any universal value. To assess the impact of the various assumed phase functions, we recomputed the H_V magnitudes from the photometry of Grav et al. (2003, 2007) and Rettig et al. (2001) assuming $\beta = 0.04$ magnitudes degree^{-1} for all objects, consistent with the value used in the analysis of the current data. Figure (2.3) shows that the systematic differences of Figure (2.2) largely disappear, showing that the offsets result from phase and are not intrinsic to the data.

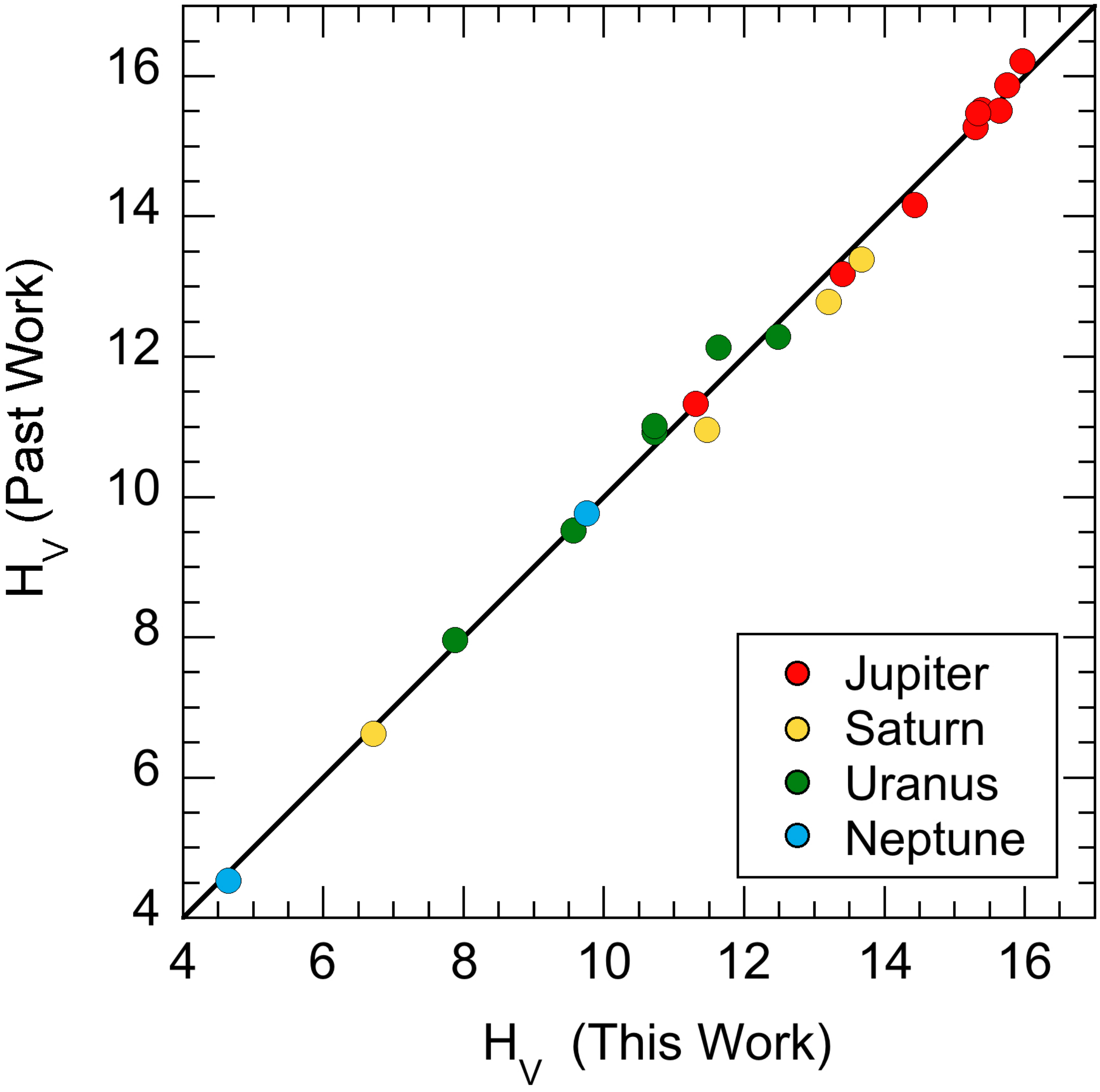

Figure 2.3: Same as Figure (2.2) except the values from Grav et al. 2003, 2004 and Grav and Bauer 2007 now reflect H_V values calculated with $\beta = 0.04$ rather than $\beta = 0.38$ or the Bowell et al. (1989) phase function where G $= 0.15$ as used in the original work. The data no longer consistently fall below the line as in Figure (2.2), showing that this systematic difference in H_V values is a result of the choice of phase function.

The measured colors, as opposed to the absolute brightnesses, should be independent of assumptions made about the phase functions (provided the latter are achromatic). The six panels in Figure (2.4) compare B-R values from this work and from previous surveys, with two panels included for the Jovian and Uranian satellites to compare colors from different authors. Considered as a whole, the panels show that the colors are scattered on both sides of the diagonal line, as expected from random errors of measurement and/or rotational lightcurve variations. There is a hint of a systematic error of unknown origin between the Rettig et al. (2001) measurements of Jovian satellites and those from the present work. However, amounting to 0.05 to 0.10 magnitudes in B-R, we consider this unimportant (and perhaps not even statistically significant) compared to the much larger random errors indicated by the wide scatter of points about the diagonal line. This scatter largely reflects the difficulty of photometric measurements on faint satellites observed against the complex scattered light field from the nearby parent planet. For example, the colors of bright object Lysithea (which has V $\sim$ 18) agree with the data from both Rettig et al. (2001) as well as Grav and Bauer (2007) to within $\sim \pm$ 0.01 magnitudes. The much fainter Stephano (V $\sim$ 25.4) shows color differences between this work and Grav et al. (2004) of $\sim$ 0.70 magnitudes in B-V. Figure (2.5) compares the color determined in this work with colors from published surveys. The final absolute magnitudes and colors are listed in Table 2.3.

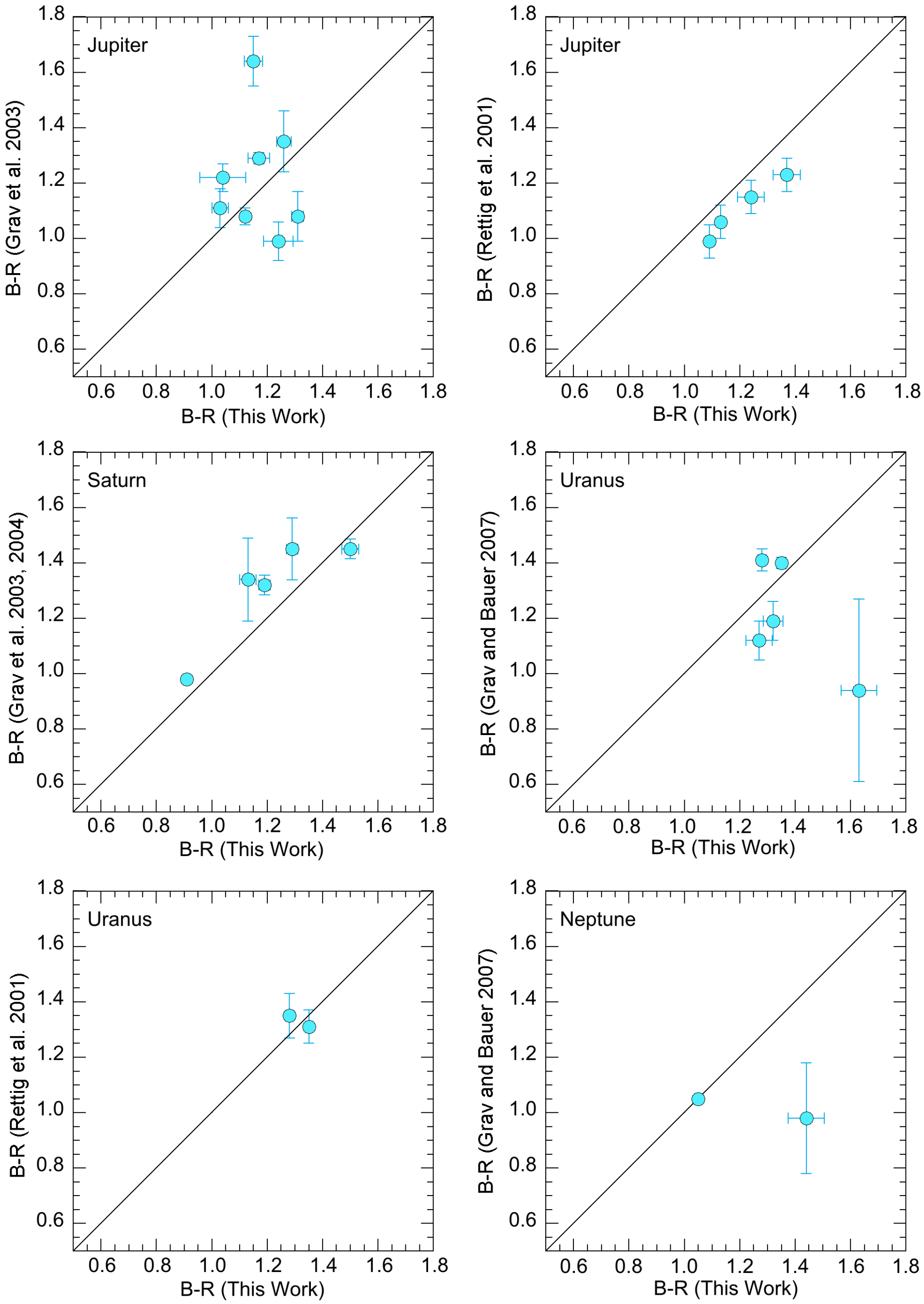

Figure 2.4: The horizontal axis on each graph shows our B-R data and the vertical axis shows B-R data from previous surveys. The diagonal line shows where the measurements are equal.

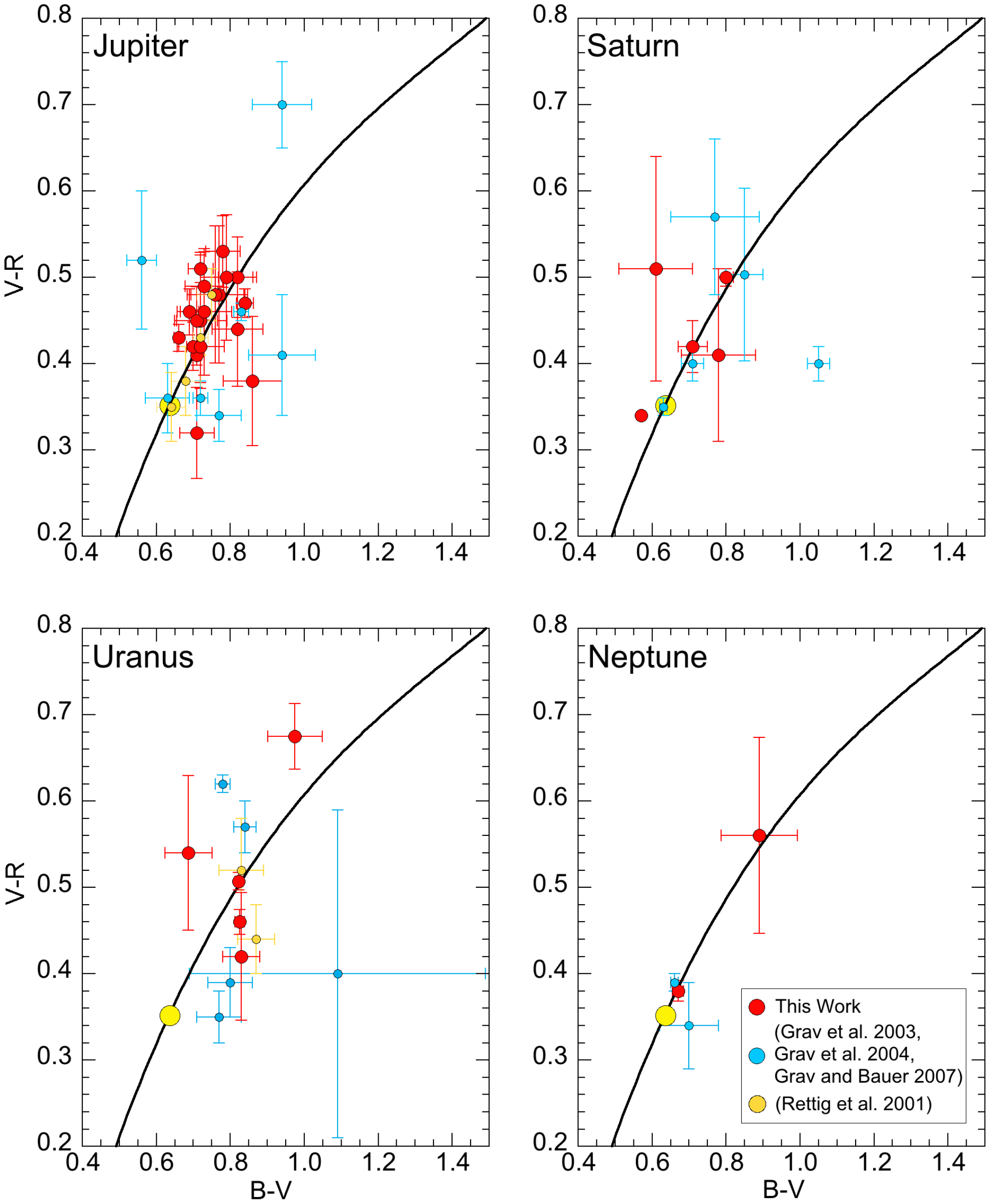

Figure 2.5: Color vs. color plots of the irregular satellites at each of the giant planets compared to previous studies. In the cases where multiple colors were reported across several nights for a single object, the colors were averaged. If colors were reported again in a later iteration of the survey, the most recent result was used

Satellite	H_R	B-V	V-R	B-R
Jupiter				
JIX Sinope	11.06 ± 0.04	0.77 ± 0.07	0.48 ± 0.08	1.25 ± 0.05
JX Lysithea	10.97 ± 0.01	0.72 ± 0.01	0.41 ± 0.01	1.13 ± 0.01
JXI Carme	10.51 ± 0.04	0.76 ± 0.08	0.48 ± 0.08	1.24 ± 0.05
JXIII Leda	12.36 ± 0.01	0.66 ± 0.01	0.43 ± 0.01	1.09 ± 0.01
JXVIII Themisto	12.86 ± 0.04	0.80 ± 0.07	0.48 ± 0.08	1.28 ± 0.04
JXIX Megaclite	14.85 ± 0.01	0.82 ± 0.07	0.44 ± 0.07	1.26 ± 0.03
JXX Taygete	15.28 ± 0.01	0.84 ± 0.02	0.47 ± 0.02	1.31 ± 0.02
JXXI Chaldene	15.61 ± 0.01	0.82 ± 0.05	0.50 ± 0.05	1.32 ± 0.03
JXXII Harpalyke	15.54 ± 0.02	0.70 ± 0.02	0.42 ± 0.03	1.12 ± 0.02
JXXIII Kalyke	14.93 ± 0.02	0.69 ± 0.03	0.46 ± 0.03	1.15 ± 0.03
JXXIV Iocaste	15.26 ± 0.03	0.86 ± 0.08	0.38 ± 0.07	1.24 ± 0.05
JXXV Erinome	15.66 ± 0.02	0.72 ± 0.06	0.42 ± 0.04	1.14 ± 0.06
JXXVI Isonoe	15.93 ± 0.04	0.78 ± 0.05	0.53 ± 0.04	1.31 ± 0.06
JXXVII Praxidike	15.01 ± 0.03	0.71 ± 0.05	0.32 ± 0.05	1.03 ± 0.03
JXXVIII Autonoe	15.21 ± 0.01	0.72 ± 0.03	0.51 ± 0.02	1.23 ± 0.04
JXXIX Thyone	15.46 ± 0.03	0.71 ± 0.06	0.45 ± 0.04	1.16 ± 0.05
JXXX Hermippe	15.02 ± 0.03	0.73 ± 0.05	0.49 ± 0.04	1.22 ± 0.06
JXVII Callirrhoe	14.20 ± 0.07	0.81 ± 0.11	0.23 ± 0.12	1.04 ± 0.08
JXLVII Eukelade	15.30 ± 0.02	0.79± 0.07	0.50 ± 0.07	1.29 ± 0.02
JXLVIII Cyllene	15.76 ± 0.01	0.73 ± 0.07	0.46 ± 0.07	1.19 ± 0.01
Saturn				
SIX Phoebe	6.37 ± 0.01	0.57 ± 0.01	0.34 ± 0.01	0.91 ± 0.01
SXXI Tarvos	12.78 ± 0.01	0.71 ± 0.04	0.42 ± 0.03	1.13 ± 0.03
SXXII Ijiraq	13.19 ± 0.01	...	...	1.40 ± 0.02
SXXVI Albiorix	10.97 ± 0.01	0.80 ± 0.02	0.50 ± 0.01	1.29 ± 0.02
SXXVIII Erriapus	13.26 ± 0.02	0.78 ± 0.10	0.41 ± 0.10	1.19 ± 0.02
SXXXI Narvi	13.98 ± 0.05	...	...	1.29 ± 0.08
SXXXVII Bebhionn	14.26 ± 0.09	0.61 ± 0.10	0.51 ± 0.13	1.12 ± 0.09
SXXXVI Aegir	15.02 ± 0.06	...	...	1.30 ± 0.06
SXXXVIII Bergelmir	14.70 ± 0.04	...	...	1.10 ± 0.15
SXXXIX Bestla	14.07 ± 0.03	...	...	1.32 ± 0.04

SXLII Fornjot	14.77 ± 0.09	...	...	1.40 ± 0.09
SXLIV Hyrrokkin	13.57 ± 0.01	...	...	1.23 ± 0.07
SLII Tarqeq	14.22 ± 0.05	...	...	1.37 ± 0.06
S/2007 S02	14.19 ± 0.05	...	...	1.37 ± 0.09
Uranus				
UXVI Caliban	9.09 ± 0.01	0.81 ± 0.02	0.47 ± 0.02	1.28 ± 0.02
UXVII Sycorax	7.34 ± 0.01	0.81 ± 0.01	0.54 ± 0.01	1.35 ± 0.01
UXVIII Prospero	10.21 ± 0.03	0.81 ± 0.04	0.51 ± 0.05	1.32 ± 0.04
UXIX Setebos	10.18 ± 0.03	00.78 ± 0.02	0.49 ± 0.04	1.27 ± 0.04
UXX Stephano	10.97 ± 0.02	0.97 ± 0.07	0.66 ± 0.05	1.63 ± 0.06
UXXI Trinculo	12.28 ± 0.15	...	...	...
Neptune				
NI Halimede	9.20 ± 0.06	0.89 ± 0.10	0.56 ± 0.11	1.44 ± 0.06
NII Nereid	4.26 ± 0.01	0.67 ± 0.02	0.38 ± 0.01	1.05 ± 0.01
NIV Neso	10.25 ± 0.10	...	0.58 ± 0.13	...

Table 2.3: Adopted Absolute Magnitudes and Colors

2.4 Discussion

2.4.1 Colors

The irregular satellite colors were averaged at each planet and are plotted in Figure (2.6) together with the mean colors of other small body populations from Jewitt (2015). The "reddening line" that spans Figure (2.6) (and is also present in the plots from Figure (2.5)) from bottom left to upper right shows the locus of colors of objects having linear normalized reflectivity gradients, $S'(\lambda)$ (measured in %/1000 Å), defined by $S'(\lambda) = (dS(\lambda)/d\lambda)/\overline{S} =$ constant, where $S(\lambda)$ is the ratio of the flux density at wavelength λ to the flux density of the Sun and $\overline{S}$ is the average value of S (Jewitt and Meech 1988). The reddening line is not a fit to the data and has no free parameters, other than being forced to pass through the B-V, V-R colors of the Sun. The figure shows that the satellite data all fall on the reddening line within the $\pm 1\sigma$ error bars, indicating that they collectively possess linear reflectivity spectra as, indeed, do most objects in the outer solar system (Jewitt 2015). The mean optical colors of the irregular satellite populations (B-V, V-R = 0.75 ± 0.01, 0.44 ± 0.02 at Jupiter, 0.69 ± 0.04, 0.44 ± 0.03 at Saturn, 0.84 ± 0.03, 0.53 ± 0.03 at Uranus, and 0.77±0.11, 0.50±0.09 at Neptune) are less red than either the hot (B-V, V-R = 0.89 ± 0.05, 0.54 ± 0.04) or cold (1.06 ± 0.02, 0.6 6± 0.02) components of the Kuiper belt, redder than the C-type asteroids (∼0.70, ∼0.38; Dandy et al. 2003) but most similar to the D-type asteroids (∼0.73, ∼0.46), as shown in Figure (2.6). The D-types are especially abundant in the Jovian Trojan population but have a minor presence also in the main belt.

Figure (2.6) shows that the irregular satellites of Jupiter, Saturn, Neptune and Uranus are clustered near each other in color-color space, and are red-grey in color implying that the color of the irregular satellites does not depend on distance from the Sun. The color of each individual satellite is independent of its magnitude, as shown in Figure (2.7). This lack of dependency of magnitude and similarity in color further signifies a common origin.

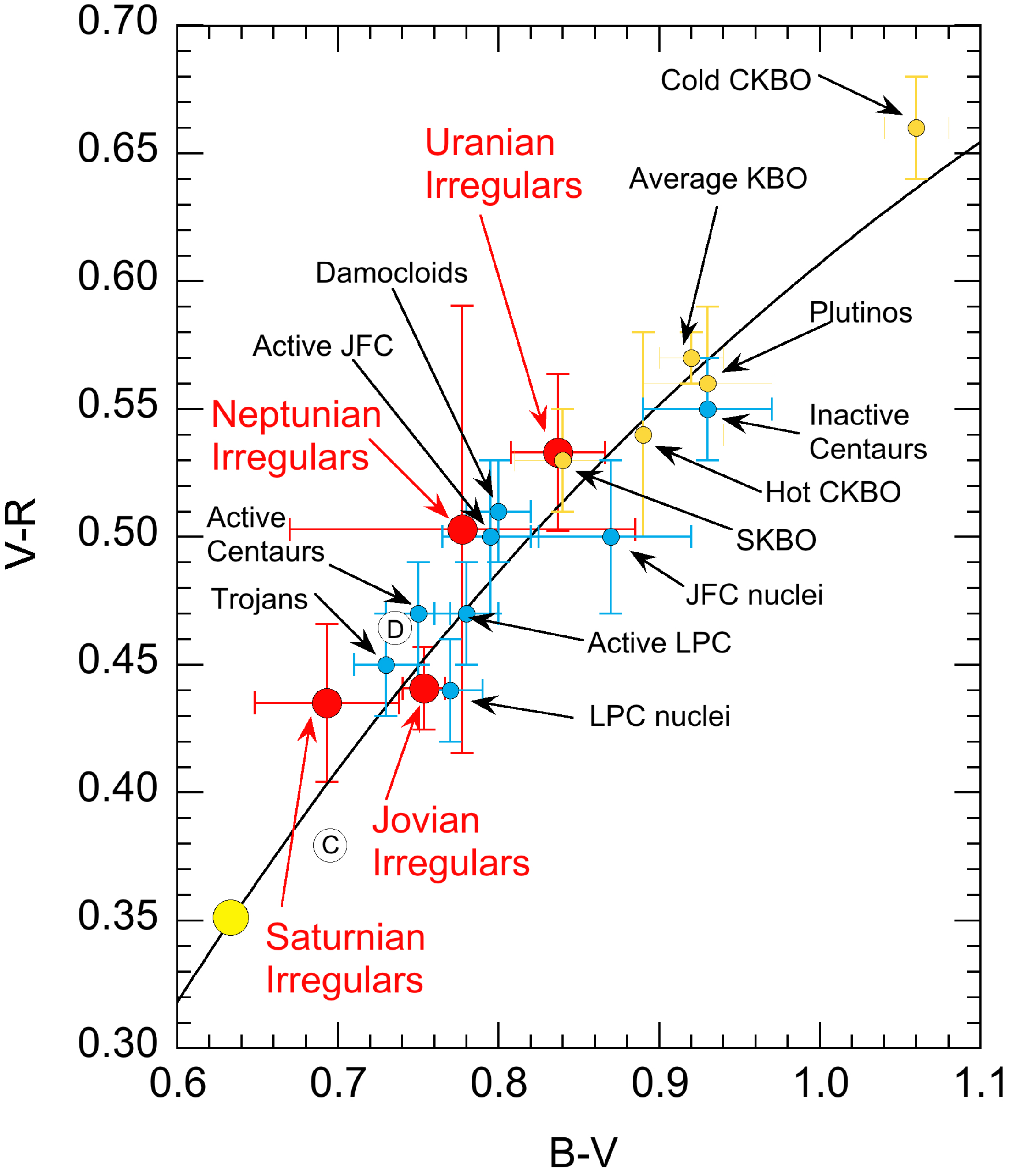

Figure 2.6: Color vs. color plot of small body populations in the solar system. Yellow data points represent Kuiper belt objects and blue data points represent comet, or comet-like objects. The circles labeled "C" and "D" represent the average color of the C-class and D-class asteroid populations respectively. The red data points are the average colors of the irregular satellites for each of the four giant planets. The color of the Sun is represented by the large yellow circle (Holmberg et al. 2006).

We used the Kolmogorov-Smirnov test as well as the Anderson-Darling (1954) test to assess the likelihood that the B-R colors of the different satellite populations could be drawn by chance from a common parent population. The Anderson-Darling test is more sensitive to the differences of the tails of the compared populations resulting mostly in lower probabilities than produced by the Kolmogorov-Smirnov test. The most discrepant colors, as suggested visually from Figure (2.8), occurs between the Jupiter and Uranus satellite color distributions, which have a probability of sharing a common parent $\sim$1.0% according to the Kolmogorov-Smirnov test (Table 2.4), and 0.5% according to the Anderson-Darling test (Table 2.5). Even the more stringent of these still does not meet the nominal 99.7% probability associated with a 3σ detection in a Gaussian distribution. Given this, and the very small Uranus satellite sample size we do not regard the difference as significant. We also compared the irregular satellite colors with the Jovian Trojan color distribution (from Peixinho et al. 2015), finding no evidence for a significant difference.

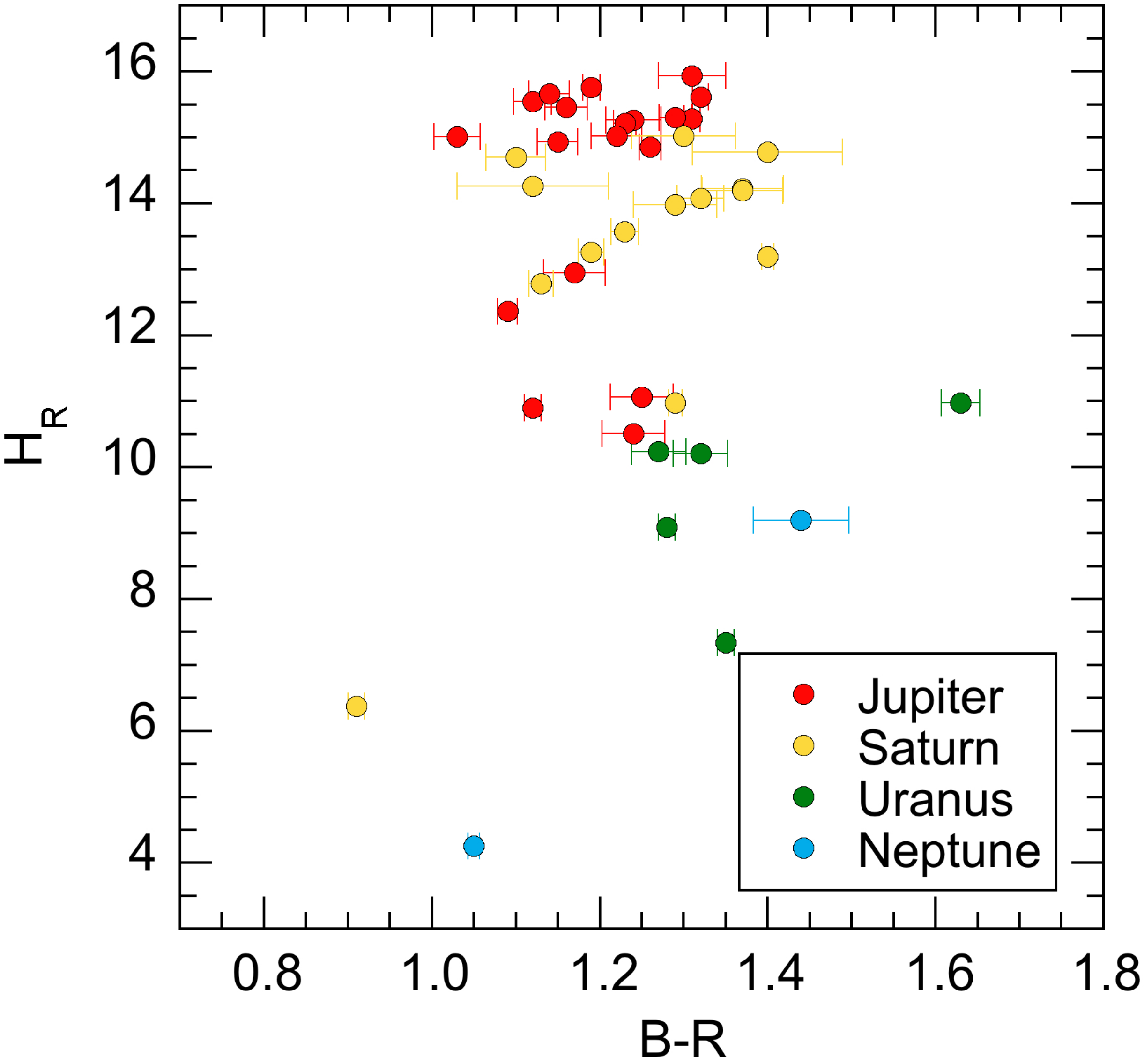

Figure 2.7: B-R color versus absolute R magnitude. There are no apparent correlations, implying that the color does not depend on magnitude

Group	Jsat	Ssat	Usat	Nsat	JTro
Jsat	1.000	0.300	0.010	0.585	0.848
Ssat		1.000	0.395	0.605	0.100
Usat			1.00	0.705	0.007
Nsat				1.000	0.657
Jtro					1.000

Table 2.4: Kolmogorov-Smirnov Probabilities - probability that any two given color distributions could be drawn from the same parent population. The lower half of the diagonally symmetric matrix is not shown.

Group	Jsat	Ssat	Usat	Nsat	JTro
Jsat	1.000	0.130	0.005	0.008	0.704
Ssat		1.000	0.310	0.087	0.261
Usat			1.00	0.319	0.389
Nsat				1.000	0.142
Jtro					1.000

Table 2.5: Anderson Darling Probabilities - Probability that any two given color distributions could be drawn from the same parent population. The lower half of the diagonally symmetric matrix is not shown.

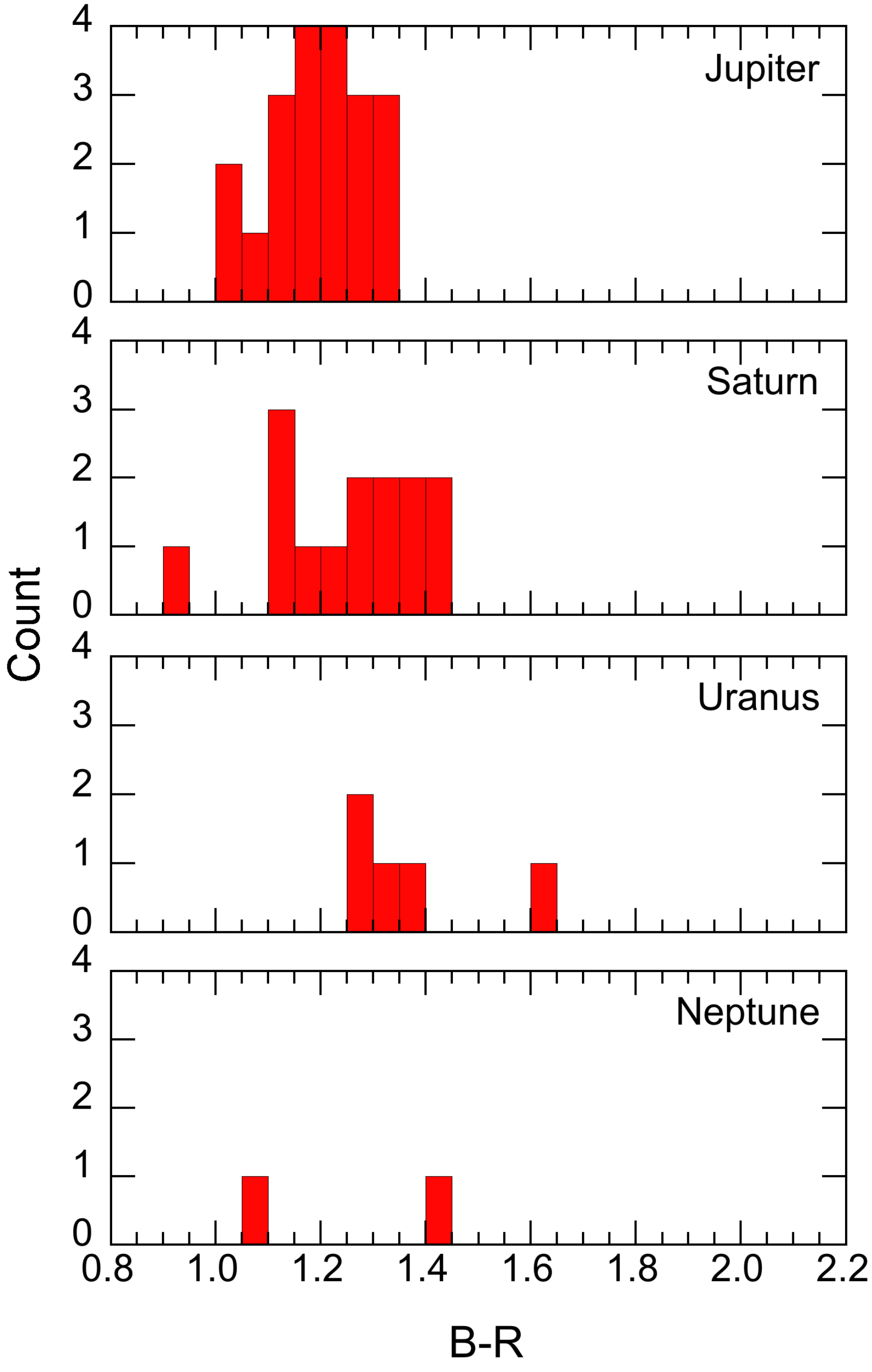

Figure 2.8: Histograms of B-R magnitudes of the irregular satellites observed in this survey at each of the giant planets. Error bars on the colors are mostly comparable to, or smaller than, the bin size.

Jarvis et al. (2000) suggested that asteroids ejected from the Kirkwood gaps in the main belt might have been captured by Jupiter. Vilas et al. (2006) reported spectral similarities between the irregular satellites and main belt asteroids (specifically the C- and D-class asteroids in the classification system of Tholen 1989) and, on this basis, also suggested that the main-belt is the source region for the Jovian irregular satellites. However, a main-belt source seems hard to support for two reasons. First, the number of Jovian Trojans larger than 5 km in size are similar (Shoemaker et al. 1989). However, while most Trojans are D- or P-types, such spectral classifications are rare in the main-belt asteroids. Second, the asteroid belt at $\sim$2 to 3 AU hardly seems a good source for the irregular satellites of Saturn (10 AU), Uranus (20 AU) or Neptune (30 AU).

A currently popular suggested source region for the irregular satellites is the Kuiper belt, with the suggestion being that the irregular satellites could have been scattered from the Kuiper belt during planetary migration (Morbidelli et al. 2005). However, it is clear from Figure (2.6) that the average colors of the irregular satellites at each planet are all bluer than any of the Kuiper belt sub-populations, as are the Jovian Trojans. If the irregular satellites were captured from a trans-Neptunian source, then their optical colors must have been modified after capture. The specific difference is that the Kuiper belt population contains ultrared matter (B-R $>$ 1.6, Jewitt 2002) while only one irregular satellite (UXX Stephano, with B-R = 1.63±0.06, see Table 2.3) is marginally consistent with ultrared color. Some evidence in seeming support of color modification is provided by observations of the Centaurs, which show a broad distribution of colors for large perihelion distances, $q \gtrsim 8$ to 10 AU, but which lack ultrared members at smaller perihelion distances. Similarly, the nuclei of Jupiter family comets also lack ultrared matter, even though they were extracted from the Kuiper belt via the Centaurs. A plausible mechanism is resurfacing, caused by the ejection of particles at sub-orbital velocities in response to sublimation (Jewitt 2002). Also, the dynamical families of irregular satellites are likely collisionally produced (Nesvorný, 2003). Bottke et al. (2013) explored the possibility that collisions between the irregular satellites cause dark material to be distributed onto the surfaces of the inner regular satellites. Though some of the dust from collisions can be lost, a portion could fall back and cover the surface, similar to the slow, sublimated particles of the Centaurs and comets. Another possibility is a chemical change caused by volatilization of trace species as objects approach the Sun (Wong and Brown 2017). However, the critical distances for resurfacing (8 to 10 AU in the resurfacing hypothesis, where outgassing activity is first triggered by crystallization of amorphous ice; Jewitt 2002, 2009, 2015; and ∼17 AU in the H_2S model of Wong and Brown; 2017) are too small for the satellites of Uranus (at 20 AU) and Neptune (30 AU) to be affected. If Centaur-like color modification were the operative process, then we should expect to find ultrared matter in the satellites of Uranus and Neptune and, possibly even Saturn with an abundance ∼1/3, as in the dynamically hot populations of the Kuiper belt.

2.4.2 Shapes

Our data also offer statistical information about the average shapes of the irregular satellites. Figure (2.9) shows the difference in the absolute magnitudes of satellites that were observed on two different days. According to the Anderson-Darling test, the measured distribution of differences (blue histogram in the figure) is consistent with derivation from a Gaussian parent population (the probability that a larger Anderson-Darling statistic could be obtained by chance is 0.032). The least-squares fit of a Gaussian is also shown in the Figure. The fit has mean -0.001±0.003 magnitudes, consistent with zero, and FWHM = 0.32±0.01 magnitudes.

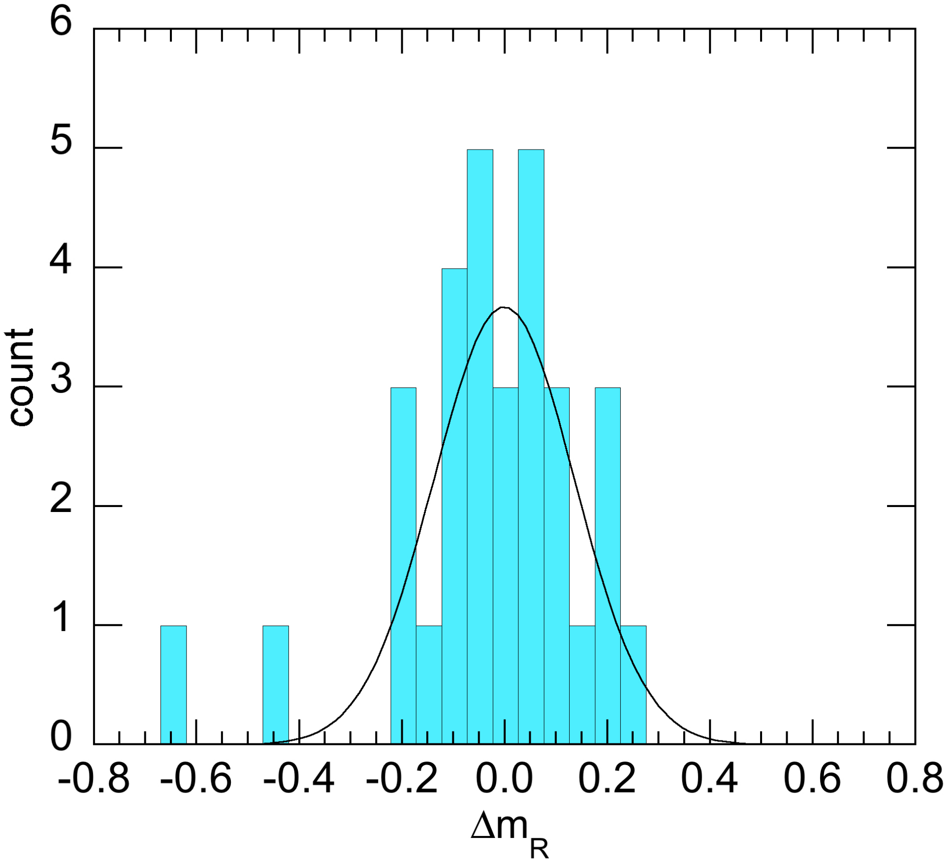

Figure 2.9: The distribution of differences in absolute magnitude of the irregular satellites measured on different days (blue histogram) compared with a least-squares fitted Gaussian (black line). The width of the distribution indicates that the irregular satellites have a sky-plane axis ratio $b/a = 1.16$, similar to the mean projected shape of the main-belt asteroids. Collisional control is likely responsible for the shapes of objects of both types.

The shape can be estimated from the lightcurve range, Δm_R, using

$$\Delta m_R = 2.5 \log(b/a) \tag{2.2}$$

where the body is taken to be elongated in shape with long and short axes b and a, respectively, both projected into the sky-plane. We assume that the pair-wise observations of each satellite are uncorrelated with the rotational phase. Then, our estimate of the average photometric range is Δm_R = FWHM/2 = 0.16±0.01 magnitudes and substitution into Equation (2.2) gives a sky-plane axis ratio b/a = 1.16±0.01. Szabó and Kiss (2008) made a statistical analysis of 11,735 asteroids and found that b/a peaks at 1.2, with 80% of the data falling in the range of b/a = 1.1-1.2, which we regard as consistent with the average irregular satellite value. The normalized cumulative distributions of the brightness differences of the irregular satellites (red circles) are compared with those of asteroids (black line) from Szabó and Kiss (2008) in Figure (2.10). We conclude that there is no observational evidence for a difference between the average shapes of the irregular satellites and the asteroids. Given that the shapes of the asteroids are collisionally determined, we likewise conclude that irregular satellites are also shaped by collisions, and this is consistent both with the existence of dynamical families in the Jovian satellite population, and with the inference by Bottke et al. (2013) that irregular satellites are, as a group, highly collisionally processed.

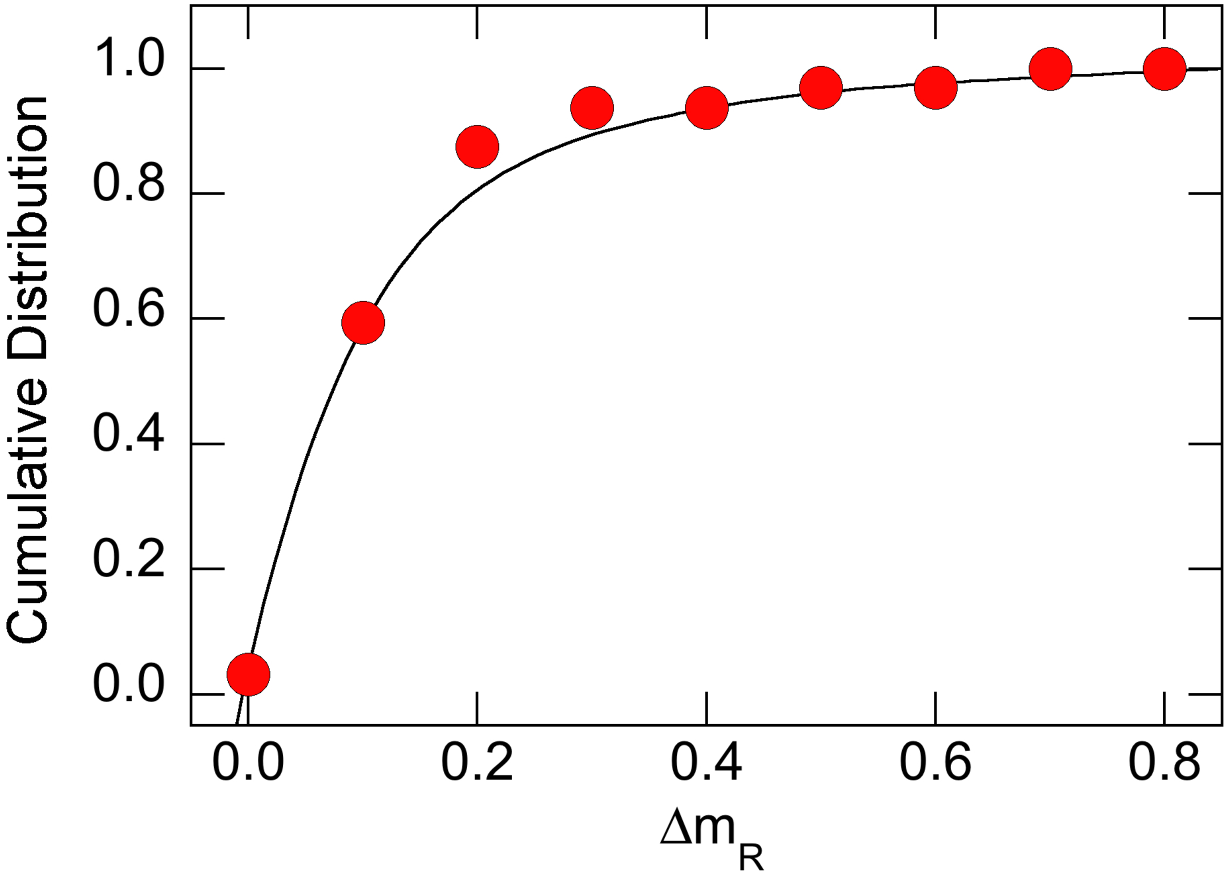

Figure 2.10: Comparison of the normalized cumulative distribution of brightness differences of the irregular satellites from this work (red circles) with the same distribution for main-belt asteroids (black line) reported by Szabó and Kiss (2008). The distributions match well, consistent with a common origin by collisions.

2.5 Conclusion

We present the absolute magnitudes and colors of the irregular planetary satellites at each of the giant planets and used their average population colors to compare them to other populations in the solar system in search for a common origin.

- The optical colors of the irregular satellites of the four giant planets are statistically similar to each other and independent of heliocentric distance.
- The satellites lack the ultrared matter that colors the surfaces of many Kuiper belt objects. About 80% of the cold-classical and 30% to 40% of the hot classical Kuiper belt objects have B-R $>$ 1.60, whereas only one of the measured irregular satellites (UXX Stephano, with B-R = 1.63±0.06) might fall in the same range.
- If the irregular satellites were captured from the Kuiper belt, then their surface colors must have been modified. The lack of ultrared surfaces even on the (cold) irregular satellites of Uranus and Neptune suggests that such modification cannot have been by any plausible thermal process.
- The means and the distributions of the shapes of the irregular satellites (average projected axis ratio b/a = 1.16±0.01) and main-belt asteroids (b/a = 1.1-1.2, Szabo and Kiss 2008) are similar. Collisional shattering likely determines the shapes in both types of object.

REFERENCES

[1] Anderson, T.W.; Darling, D.A. 1954. Journal of the American Statistical Association. 49, 765.

[2] Bauer, J. M. Grav, T. Buratti, B. J. Hicks, M. D. 2006, Icarus, 184, 181-197

[3] Bottke, W. F. Vokrouhlický, D. Nesvorný, D. Moore, J. M. 2013, Icarus, 223, 775-795

[4] Bowell, E., Hapke, B., Domingue, D., et al. 1989, in Asteroids II, ed. R. Binzel, T. Gehrels, S. Matthews (Tucson, AZ: Univ. Arizona Press), 524

[5] Colombo, G. Franklin, F. A. 1971, Icarus, 15, 186-189

[6] Dandy, C. L. Fitzsimmons, A. & Collander-Brown, S. J. 2003, Icarus, 163, 363

[7] Grav, T. Bauer, J. 2007, Icarus, 191, 267-285

[8] Grav, T. Holman, M. J. Fraser, W. C. 2004, ApJ, 613, L77-L80

[9] Grav, T. Holman, M. J. Gladman, B. J. & Aksnes, K. 2003, Icarus, 166, 33

[10] Heppenheimer, T. A. Porco, C. 1977, Icarus, 30 385-401

[11] Holmberg, J. Flynn, C. Portinari, L. 2006, MNRAS, 367, 449-453

[12] Jarvis, K. S. Vilas, F. Larson, S. M. Gaffey, M. J. 2000, Icarus, 145, 445-453

[13] Jewitt, D. C. 2002, AJ, 123, 1039

[14] Jewitt, D. C. 2009, AJ, 137, 4296

[15] Jewitt, D. 2015, AJ, 150, 201

[16] Jewitt, D. Haghighipour, N. 2007, ARA&A, 45, 261-295

[17] Jewitt, D. Luu, J. Trujillo, C. 1998, AJ, 115, 2125-2135

[18] Jewitt, D. Meech, K. J. 1988, AJ, 96, 1723-1730

[19] Jewitt, D. Mutchler, M. Weaver, H. Hui, M.-T. Agarwal, J. Ishiguro, M. Kleyna, J. Li, J. Meech, K. Micheli, M. Wainscoat, R. Weryk, R. 2016, ApJ, 829, L8

[20] Jewitt, D. Sheppard, S. 2005, Space Sci. Rev., 116, 441-455

[21] Jewitt, D. C. Trujillo, C. A. & Luu, J. X. 2000, AJ, 120, 1140

[22] Landolt, A. U. 1992, AJ, 104, 340-371

[23] Morbidelli, A. Levison, H. F. Tsiganis, K. Gomes, R. 2005, Nature, 435, 462-465

[24] Nesvorný, D. Alvarellos, J. L. A. Dones, L. Levison, H. F. 2003, AJ, 126, 398-429

[25] Nicholson, P. D. Cuk, M. Sheppard, S. S. Nesvorný, D. Johnson, T. V. 2008, The solar system Beyond Neptune, 411-424

[26] Oke, J. B. Cohen, J. G. Carr, M. Cromer, J. Dingizian, A. Harris, F. H. Labrecque, S. Lucinio, R. Schaal, W. Epps, H. Miller, J. 1995, PASP, 107, 375

[27] Peixinho, N. Delsanti, A. & Doressoundiram, A. 2015, A&A, 577, A35

[28] Pollack, J. B. Burns, J. A. Tauber, M. E. 1979, Icarus, 37, 587-611

[29] Rettig, T. W. Walsh, K. Consolmagno, G. 2001, Icarus, 154, 313-320

[30] Sheppard, S. S. & Jewitt, D. C. 2003, Nature, 423, 261

[31] Shoemaker, E. M., Shoemaker, C. S., & Wolfe, R. F. 1989, in Asteroids II, ed. R. P. Binzel, T. Gehrels, S. Matthews (Tucson, AZ: Univ. Arizona Press), 487

[32] Szabó, G. M. Kiss, L. L. 2008, Icarus, 196, 135-143

[33] Tedesco, E. F. Barker, E. S. 1981, in IAU Colloquium 61, Comets: Gases, Ices, Grains, and Plasma ed. L. Wilkening (Tucson: University of Arizona Press)

[34] Tholen, D. J. 1989 Asteroids II, 1139-1150

[35] Vilas, F. Lederer, S. M. Gill, S. L. Jarvis, K. S. Thomas-Osip, J. E. 2006, Icarus, 180, 453-463

[36] Wong, I. Brown, M. E. 2016, AJ, 152, 90

CHAPTER 3

Fragmented Comet 73P/Schwassmann-Wachmann 3

This chapter is adapted from the peer-reviewed paper titled "Fragmented Comet 73P/Schwassmann-Wachmann 3", which has been published in the Astronomical Journal (Graykowski & Jewitt 2019).

3.1 Introduction

73P is a Jupiter family comet with a semimajor axis a = 3.063 AU, orbital inclination i = 11.4°, and eccentricity e = 0.692. The comet was first reported to have fragmented into at least four pieces on September 12, 1995 (Crovisier et al. 1995), shortly before its perihelion passage at 0.94 AU on September 22. While fragments A and D were not seen during its following apparition, fragments B and C are long-lived, continuing to appear in subsequent apparitions every 5.36 years. Fragment 73P-C is the brightest of the fragments and is also the leading fragment in the orbit. These characteristics generally describe the primary fragment of a split comet according to Boehnhardt (2004), so 73P-C is therefore considered the primary nucleus. While its 2001 apparition provided a less than ideal observing geometry, the comet approached to within 0.08 AU of the Earth in 2006, providing an excellent opportunity for high resolution observations with the Hubble Space Telescope (HST). 73P fragmented again during this apparition, releasing fragments G, H, J, L, M and N, with fragments B and G famously shedding dozens of smaller pieces (Weaver et al. 2008 and Fuse et al. 2007).

Potential causes of cometary fragmentation include tidal disruption (Asphaug and Benz

1994), rotational instability (Jewitt 1997), internal build-up of thermal gas pressure (Samarasinha 2001), and impact induced fragmentation (Sekanina 1997 and Boehnhardt 2004). In the case of 73P-C, tidal disruption can be discounted since the orbit of the comet does not pass within the Roche spheres of any of the major planets or the Sun. Impacts are intrinsically unlikely and offer an even less credible explanation given that the comet has exhibited multiple breakup episodes in different orbits. Estimates of the rotational period of 73P-C (c.f. Table 3.1) are widely spread over the range from 3.019 hours (Drahus et al. 2010) to 27.2 hours (Storm et al. 2006). The lower end of this range is suggestive of fragmentation due to rotational instability (Marzari et al. 2011). However, the upper end of the range is completely inconsistent with this possibility.

In this paper, our motivation is to obtain a deeper understanding of how 73P fragmented. We focus on 73P-C and examine HST images from April, 2006 and measure the rotation period of 73P-C in order to reduce the ambiguity behind the cause of its fragmentation.

3.2 Observations

The images were taken under HST program GO 10625, with P. Lamy as the principal investigator using the Advanced Camera for Surveys (ACS) in the High Resolution Channel (HRC). The field of view of the HRC is $29'' \times 26''$ with a pixel scale of $0.028'' \times 0.025''$/pixel (Ford et al. 1998 and Ryon et al. 2019). A total of 84 images were analyzed in four filters: F475, F555, F606, F625 (Table 3.2). The observations started on 2006 April 10, 21:35 UT and ended 2006 April 11, 19:06 UT, providing a span of $\sim$21.5 hours. The observing geometry is listed in Table (3.3) for the two days on which the comet was observed.

Rotation Period (Hours)	Author(s)	Method
3.019 ± 0.001, 3.349 ± 0.002, 3.392 ± 0.002	Drahus et al. (2010)	HCN production rate. The method produces many possible periods, including solutions in the range of 10.174 to 13.567 hours, but is insensitive to periods >14 hours.
3.2 ± 0.2	Toth et al. (2006)	Photometry
3.5 - 4.0	Toth et al. (2008)	Photometry
8.8 ± 0.3, 13.2 ± 0.3, 27.2 ± 0.3	Storm et al. (2006)	Dust morphology
>10.0	Nolan et al. (2006)	Radar
> 15	Dykhuis et al. (2012)	Dust morphology

Table 3.1: Reported Period of 73P-C

Filter	λ^a	FWHM^b	N^c	t^d
F475	4760	1458	12	10-20
F555	5346	1193	12	20
F606	5907	2342	36	180
F625	6318	1442	24	20

Table 3.2: HST Image Information

[a] The central wavelength of the filter in Å

[b] The full-width-half-maximum of the filter in Å according to the Space Telescope Science Institutes instrument handbook

[c] Number of images

[d] Integration time, seconds

UT Date^a	ΔT_p^b	ν^c	r_H^d	Δ^e	α^f	$\theta_{-\odot}^g$	θ_{-V}^h	$\delta_\oplus^i$
2006 Apr 10	-60	2.9	1.240	0.292	31.2	222.1	290.6	-30.8
2006 Apr 11	-59	2.9	1.231	0.283	31.8	221.0	290.4	-31.5

Table 3.3: Observing Geometry

[a] date of observations at 22:00 UTC

[b] Number of days from perihelion (UT 2006-Jun-09) Negative numbers indicate pre-perihelion observations

[c] True anomaly, in degrees

[d] Heliocentric distance, in AU

[e] Geocentric distance, in AU

[f] Phase angle, in degrees

[g] Position angle of the projected anti-Solar direction, in degrees

[h] Position angle of the projected negative heliocentric velocity vector, in degrees

[i] Angle between Earth and target orbital plane, in degrees

3.2.1 Nucleus Measurements

The morphology of the parent body, 73P-C, can be seen in Figure (3.1). It displays an obvious coma elongated towards the southwest direction, approximately aligned with the antisolar direction (marked -$\odot$). We used aperture photometry to measure the apparent magnitude in the 84 images and accounted for the zeropoint of each filter given by `http://www.stsci.edu/hst/acs/analysis/zeropoints/old_page/localZeropoints`. We chose an aperture radius of ~0.13″ (~FWHM of the PSF), which corresponds to a distance of 27 km at the comet. We then subtracted the background flux caused by the sky and coma through an annulus immediately outside the aperture, extending out another ~0.26″. In order to analyze the data from each filter all together, we calculated the average colors with respect to filter F555 (equivalent to the Johnson V filter) and used the colors to shift the magnitudes in each filter such that they are equivalent to the F555 filter (Table 3.4). The nucleus aperture magnitudes are plotted as a function of time in Figure 3.2.

Color	Nucleus (0 - 27 km)	Coma (27 km - 136 km)	Coma (136 - 245 km)
F475-F555	0.43±0.04	0.42±0.18	0.42±0.26
F555-F606	0.25±0.04	0.26±0.05	0.26±0.06
F555-F625	0.47±0.04	0.49±0.04	0.49±0.06

Table 3.4: Nucleus and Coma Colors

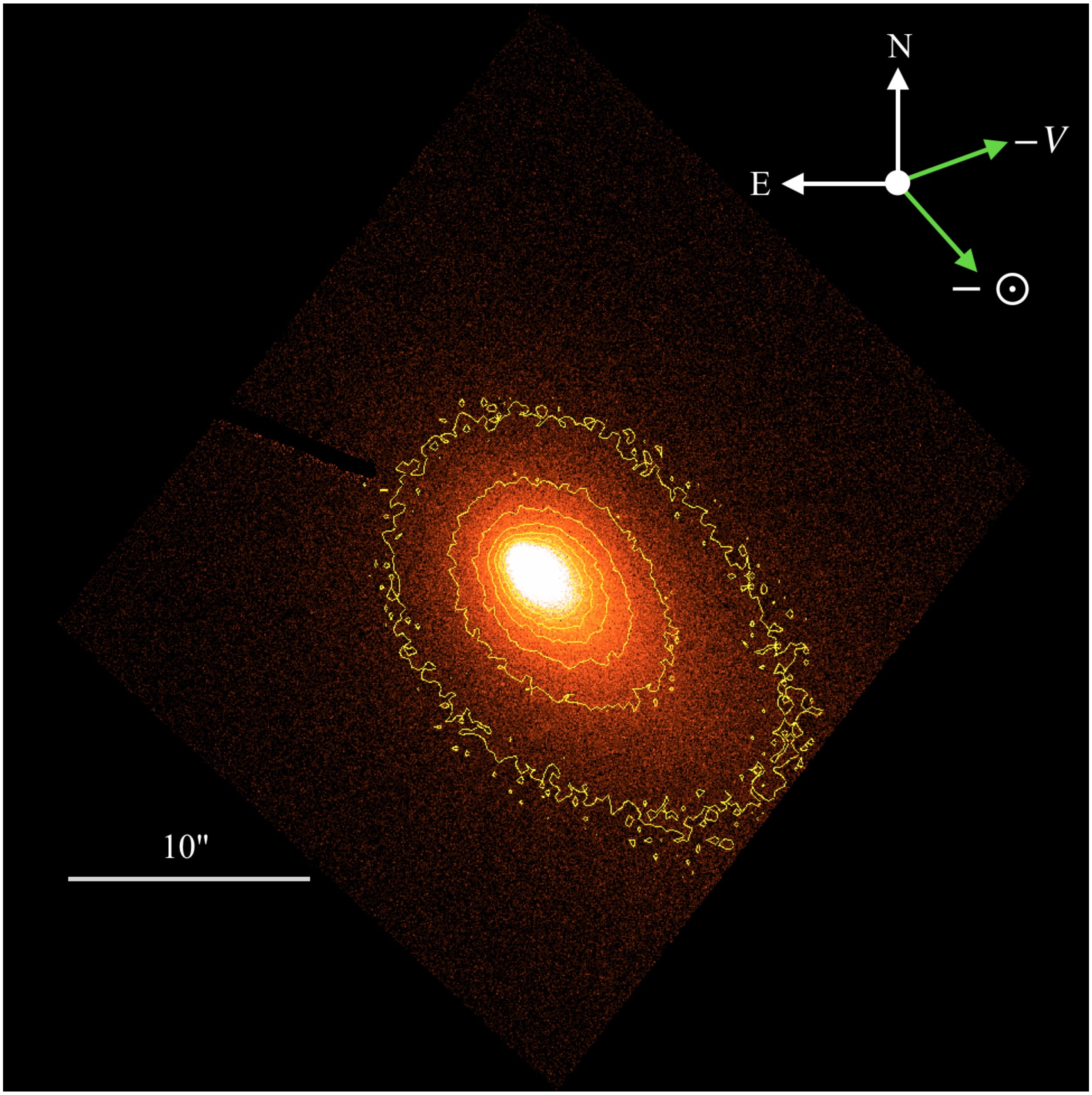

Figure 3.1: Sample single image of 73P taken with HST's ACS HRC instrument in the F555 filter with a 20 second exposure on April 10, 2006. The pixel scale is $0.028'' \times 0.025''$ / pixel. At a distance of 0.288 AU from the Earth, $1''$ corresponds to 208.9 km. The projected antisolar direction and negative velocity are represented by the vectors labeled -$\odot$ and $-V$ respectively.

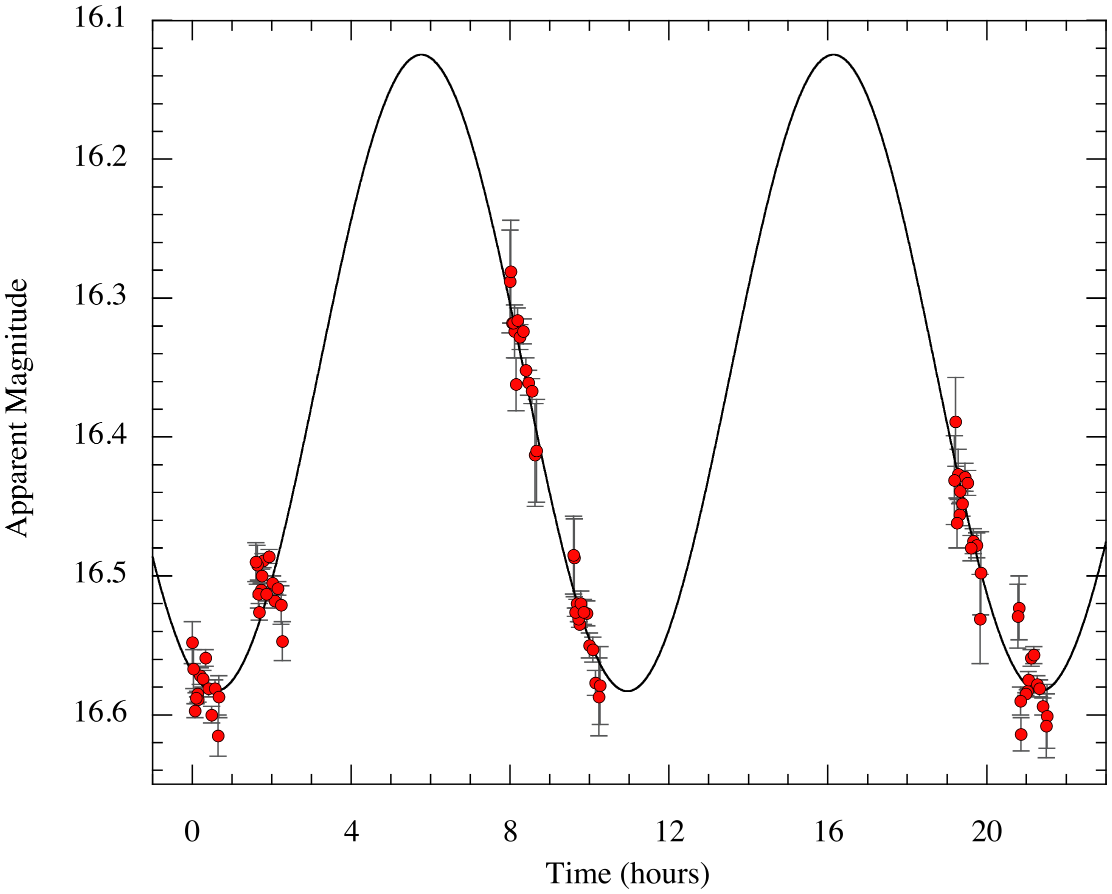

Figure 3.2: 73P-C apparent magnitude versus time plotted as red circles with 1σ error bars. The solid line shows a best-fit sinusoidal lightcurve with a period $P = 10.38 \pm 0.04$ hours and a rotation period $2P = 20.76 \pm 0.08$ hours.

3.2.2 Coma Measurements

Next, we compared the lightcurve of the central aperture (containing the nucleus and near-nucleus dust) to lightcurves of the coma annuli (containing only dust). We used the same aperture radius to obtain the lightcurve for the nucleus. We then measured the flux within the coma within two annuli extending from $\sim 0.13''$ to $\sim 0.65''$ and from $\sim 0.65''$ to $\sim 1.17''$. Instead of subtracting the background flux from an annulus immediately outside these regions, we only subtracted the flux from the sky background. For this purpose, we chose an annulus with inner and outer radii of $\sim 5.7''$ and $\sim 6.5''$ respectively, and subtracted this flux from all measurements. The aperture and annuli are drawn on an image of the comet in Figure (3.3). Colors were again calculated in the coma regions with respect to filter F555 as seen in Table (3.4) with error estimates representative of the signal-to-noise ratio (S/N). The S/N decreased further out in the coma, where the sky background had a larger effect. The resulting apparent magnitudes are plotted in Figure (3.4).

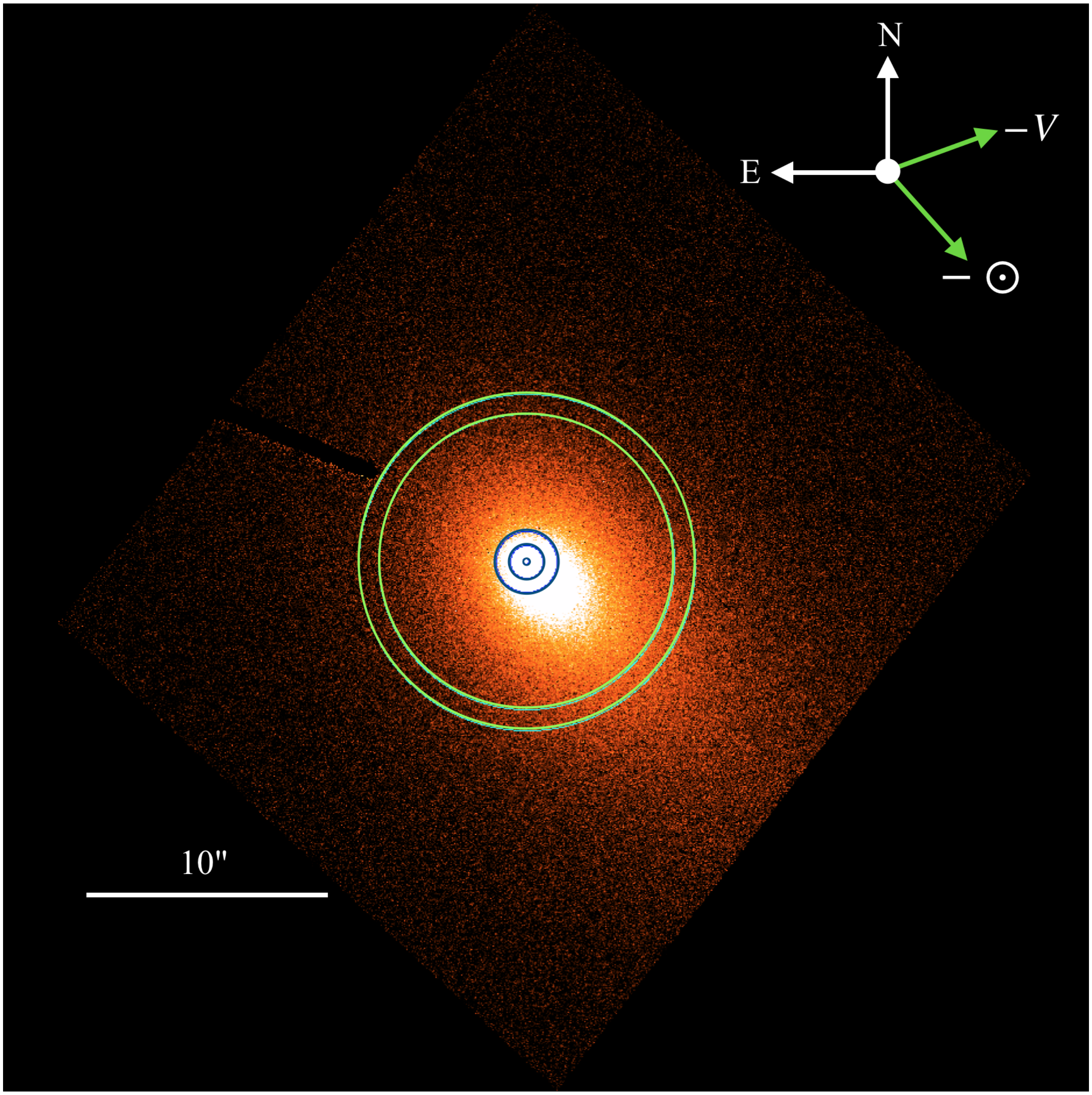

Figure 3.3: Same as Figure (3.1) but with blue circles to show photometric apertures with radii 27, 136, and 245 km and green circles to represent the inner and outer edges of the background annulus corresponding to radii ∼1190 and 1360 km.

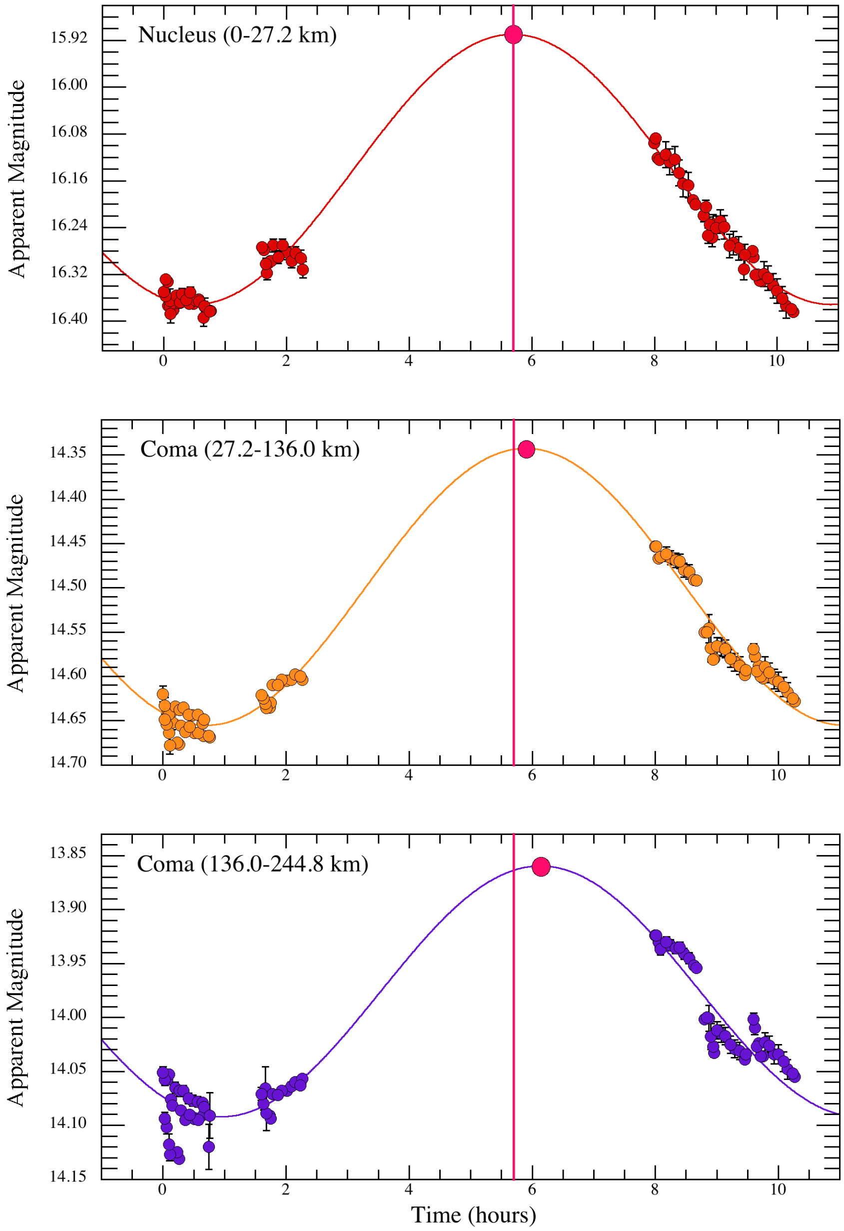

Figure 3.4: Phase folded lightcurves of the nucleus (top), the coma with inner and outer annulus radius of 27 and 136 km (middle), and the coma with an inner and outer annulus radius of 136 and 245 km (bottom). The magenta, vertical line is placed at the peak of the nucleus lightcurve, and is unmoved in the subsequent coma lightcurves. The magenta circle marks the fitted peak of each lightcurve. A phase shift is clearly visible from the nucleus to greater distances in the coma.

3.3 Results

3.3.1 Rotational Period of the Nucleus

We measured the rotation period of the nucleus by fitting a lightcurve to the time-varying magnitudes. For convenience of presentation, the time plotted in Figures (3.2) and (3.4) was calculated from

$$T = (JD - 2453836.399) \times 24 \tag{3.1}$$

where T is time in hours and JD is the Julian date obtained from the image header. We used IRAF's phase dispersion minimization (PDM) program to search for likely periods in the data, and used these values as a guide to create the best fit sinusoid curves by least squares. Figure (3.2) shows our best fit for the lightcurve of the nucleus. This sinusoidal least-squares fitted curve has a single-peaked period $P = 10.38 \pm 0.04$ hours. The lightcurves of most solar system small bodies are dominated by variation in the cross-section due to aspherical shape, rather than by surface albedo variations (Burns and Tedesco, 1979). In these cases the lightcurves are doubly periodic (two maxima and minima per rotation) owing to rotational symmetry. For 73P-C, this would imply a rotational period $2P = 20.76 \pm 0.08$ hours. This relatively long period is consistent with a lower limit $P > 10$ hours set using radar observations by Nolan et al. (2006), but disagrees with shorter periods obtained using less direct methods (Table 3.1). Incomplete sampling of the lightcurve leads to aliasing in the period determination and, therefore, we cannot exclude the possibility that other periods might fit the data. The shortest plausible period from our PDM analysis is $P = 5.01$ hours and thus we can rule out shorter periods proposed by Drahus et al. (2010), Toth et al. (2006, 2008) listed in Table (3.1).

3.3.2 Dust Outflow Speed

We next repeated the analysis for the lightcurves of the nucleus and coma regions measured from the sky-subtraction technique. Specifically, we aim to detect a phase lag in the lightcurves from the three apertures caused by the finite speed of outflow of the dust. Keeping the same period found in our best fit of the nucleus lightcurve in the previous section, we fit curves with the lightcurve period $P = 10.38 \pm 0.04$ hours to the phase-folded data in Figure (3.4). The figure shows that there is a phase lag from the nucleus to the dust regions of the coma. The phase lags fit are listed in Table (3.5). From the central aperture to the inner coma annulus there is a $\Delta T = 0.21 \pm 0.05$ hour lag while from the center to the outer coma annulus the lag is $\Delta T = 0.46 \pm 0.08$ hour. Figure (3.5) shows the phase lag versus the effective radius of each photometry annulus, computed by determining the center of light of the photons hitting the CCD in each aperture or annulus according to the surface brightness profile plotted in Figure (3.6). With a surface brightness $\propto r^{-1}$ (where r is the radial distance from the center), the effective radius, r_e, is given simply by $r_e = (r_i + r_o)/2$, where r_i and r_o are the inner and outer radii of each annulus. The speed of the dust is given by the gradient of a straight line fitted to the data in Figure (3.5). We find $v_g = 107 \pm 9$ m/s. At this speed, dust released from the nucleus would escape from the central photometry aperture of projected radius $r_o = 27$ km (Table 3.5) in a time $t \sim r_o/V_g \sim 250$ s. This time is very short compared to the nucleus rotational period and, therefore, we can neglect the effects of averaging in the interpretation of the lightcurve data.

Aperture	r_i^a	r_o^b	r_e^c	$\mid \Delta$ Phase $\mid^d$
1	0	27	13	0
2	27	136	82	0.21 ± 0.05
3	136	245	190	0.46 ± 0.08

Table 3.5: 73P-C Nucleus and Coma Lightcurve Phase and Phase Shift

[a] Inner radius of annulus in km, $1'' \sim 208.9$ km

[b] Outer radius of annulus in km

[c] Effective radius of annulus in km

[d] Phase lag relative to the lightcurve of the nucleus (hours)

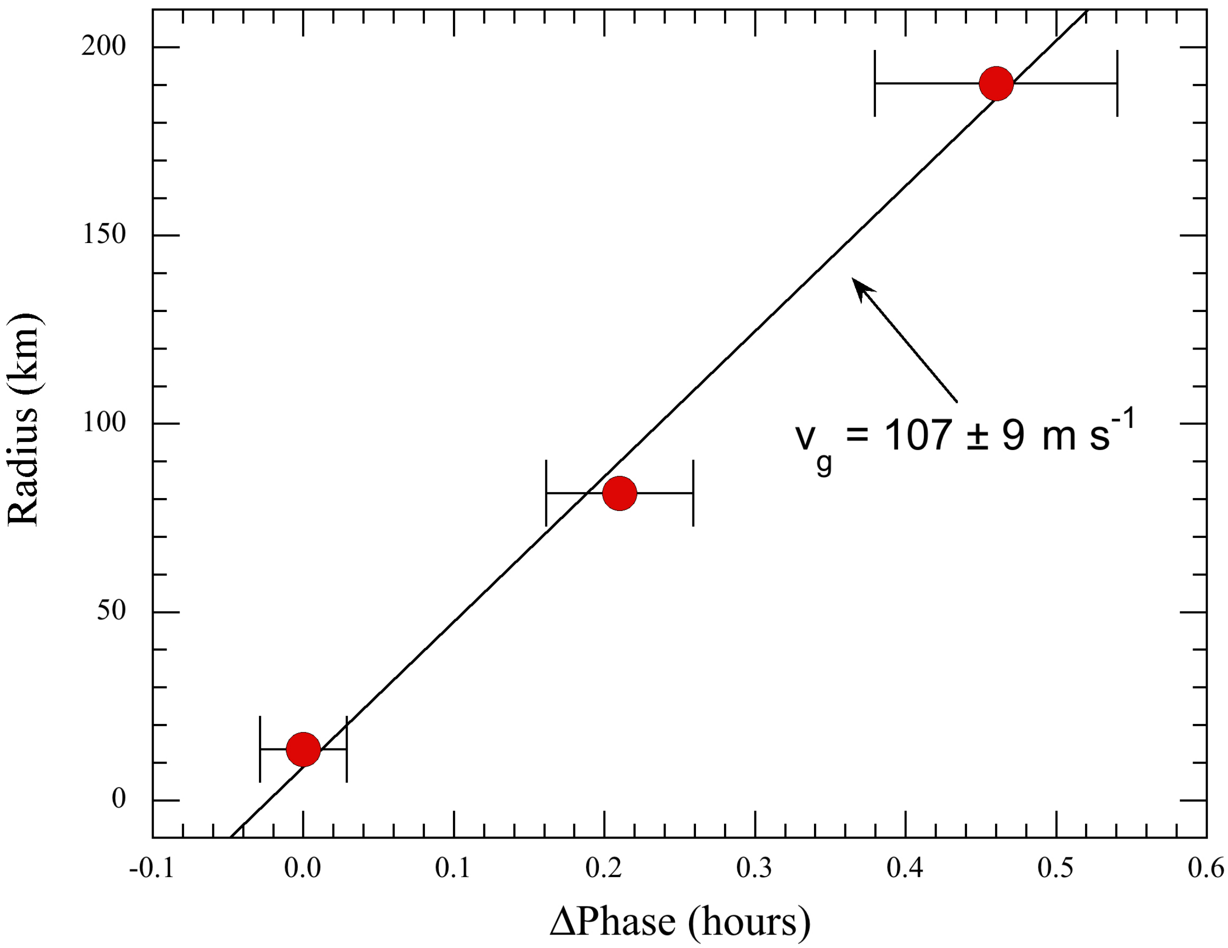

Figure 3.5: The relative phase shift plotted against the distance from the center of the nucleus, where the reference phase measured from the lightcurve of the nucleus is set to zero. From left to right, the red points then represent the relative phase at the nucleus, 82 km from the nucleus into the coma, and 190 km from the nucleus into the coma. The error bars represent the one sigma error on the phase obtained from each fit. From this, we obtain a dust speed $v_g = 107 \pm 9$ m s^{-1}.

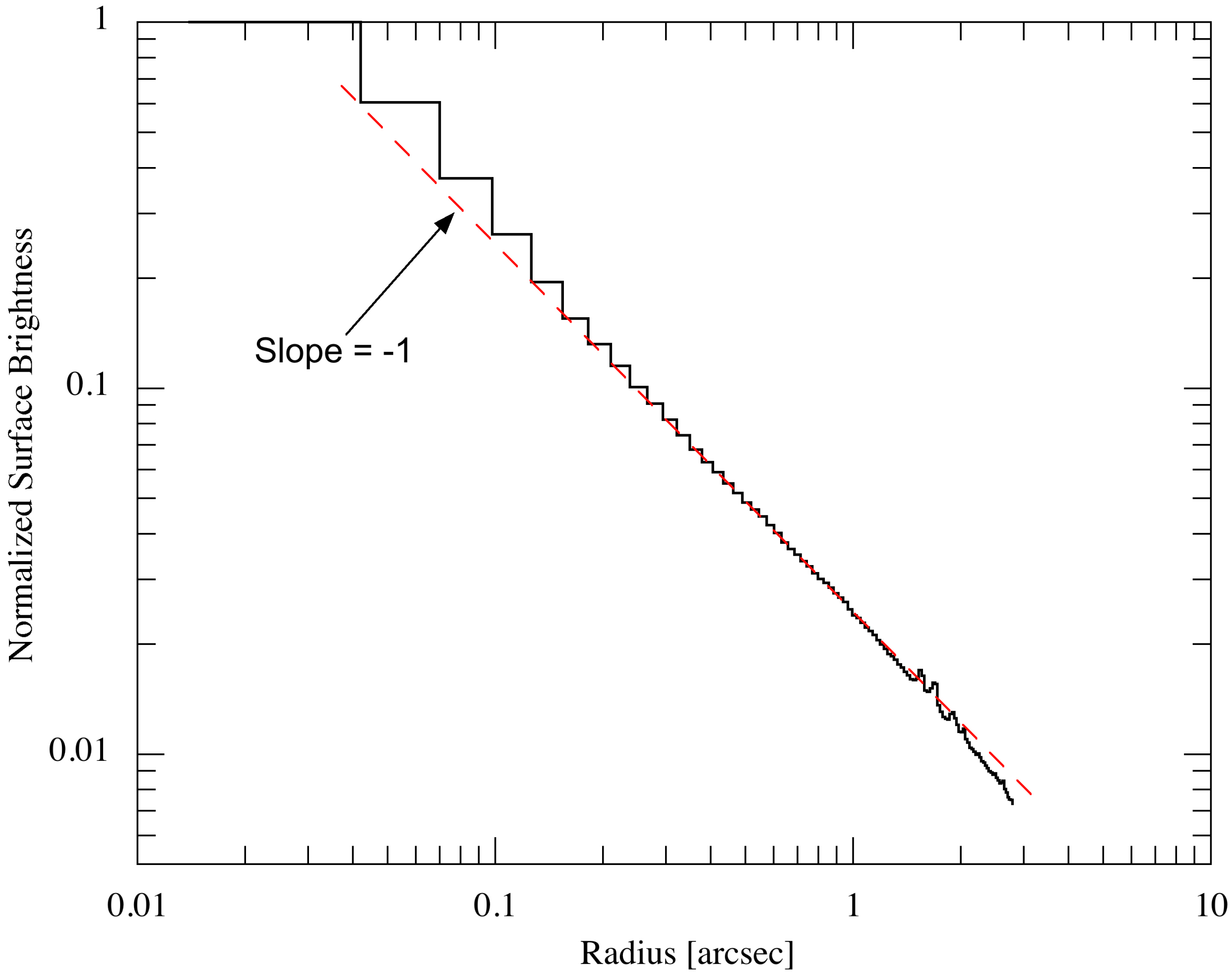

Figure 3.6: The surface brightness profile of 73P-C. The red line represents a surface brightness profile $\propto r^{-1}$, where r is the radial distance from the center of the nucleus. The surface brightness profile follows this line closely except $r \lesssim 0.15''$ where the PSF has an effect, and $r \gtrsim 1.5''$, where the background subtraction systematics are important.

3.3.3 Size of the Nucleus

We converted from apparent to absolute magnitude, H_V, defined as the magnitude corrected to unit heliocentric and geocentric distance (r_H and Δ, respectively) and to phase angle $\alpha = 0°$. For the apparent magnitude, m_V, the correction is

$$H_V = m_V - 5\log_{10}(r_H\Delta) - f(\alpha) \tag{3.2}$$

where $f(\alpha)$ is the phase function representing the angular dependence of the scattered sunlight at phase angle α in degrees. We assume a linear phase function

$$f(\alpha) = (0.046 \pm 0.017)\alpha \tag{3.3}$$

based on measurements of 37 Jupiter family comets reported by Kokotanekova (2017). We find the absolute magnitude of 73P-C to be $H_V = 17.3 \pm 0.1$.

We estimated the size of the nucleus using

$$C_e = \frac{\pi(2.25 \times 10^{16})}{p_V} 10^{-0.4[H_V - V_\odot]} \tag{3.4}$$

where p_V is the geometric albedo, which we assume to be 0.04 (Hartmann et al. 1987, Lamy et al. 2004, Fernández et al. 2013), H_V is the absolute magnitude and $V_\odot \sim$ -26.77 is the apparent magnitude of the Sun. The effective nucleus radius is then $r_n = \sqrt{(C_e/\pi)}$ and we find $r_n = 1.2 \pm 0.1$ km. This is consistent with the pre-breakup radius $r_n \sim 1$ km as reported by Sekanina (1989) and $r_n \sim 1.1$ km as reported by Boehnhardt et al. (1999). In both of these studies, as well as our calculation of the radius, coma contamination was not accounted for, and therefore these values all represent an upper limit on the size of the nucleus.

Toth et al. (2005) accounted for coma contamination by modeling the expected brightness profile of the coma and nucleus, and calculating the residual flux associated with just the nucleus. From this, Toth et al. (2005) find that as of 2001 November 26, 73P-C had decreased in radius to $r_n = 0.68 \pm 0.04$ km (i.e. to only 25% of the original volume). However, the smaller size is likely a result of accounting for dust contamination rather than the nucleus physically shrinking over time. We then conducted a similar analysis by extrapolating the surface brightness profile in the coma to the center aperture. We subtracted the estimated flux of the coma within the center aperture from the flux value we measured using aperture photometry. The residual flux represents that of the isolated nucleus. In the measured region of the coma, Figure (3.6) shows the surface brightness profile $\propto r^{-1}$, where r is the radial distance from the center of the nucleus. This implies that the integrated flux within an annulus is simply proportional to the width of the annulus, i.e. flux $\propto r_o - r_i$. Therefore, if there is no nucleus present, we expect to find flux ratios in the different apertures $A1/A2$ = 27/(136-27) = 0.25 and $A1/A3$ = 27/(245 - 136) = 0.25 (c.f. Table 3.5). Instead, the average flux measured through the center aperture is $\sim$ 29% ± 2.5% of the average flux in the indicated coma annuli. The residual flux corresponds to an apparent magnitude $m_V \sim 18.7 \pm 0.7$, absolute magnitude $H_V \sim 19.7 \pm 0.7$, and radius $r_n \sim 0.4 \pm 0.1$ km. This estimate (diameter 0.8±0.2 km) is comparable, within the uncertainties, to Arecibo (12.6 cm) and Goldstone (3.5 cm) radar data reported to show that fragment C is at least 1 km in diameter (Nolan et al. 2006).

3.4 Discussion

3.4.1 Stability of the Nucleus Rotation

Is rotational instability a plausible mechanism of fragmentation for 73P? We compare the minimum period we derived with the critical rotational period of the body given by

$$P_C = k \left[\frac{3\pi}{G\rho} \right]^{\frac{1}{2}} \tag{3.5}$$

where G is the gravitational constant, ρ is the density, k is a dimensionless constant that depends on the shape of the body. For a sphere, k reduces to 1. We assume that a prolate shaped nucleus generates the lightcurve, so $k = a/b$ where $a > b$. We also assume a density $\rho = 600$ kg/m^3, as representative for comets (Britt et al. 2006). With photometric variations of $\sim 0.31 \pm 0.01$ magnitudes in the nucleus, we infer $k = 1.33 \pm 0.01$, and a critical period $P_C = 5.67 \pm 0.04$ hours for a prolate spheroid of this density, which is far shorter than our 10.38 hour best-fit single-peaked lightcurve period. Therefore, we can confidently rule out the possibility of break up due to rotational instability.

3.4.2 Coma Dust Speed and Particle Size

From the measured speed of the dust in the coma, we can estimate the average dust grain size and mass loss rate from the nucleus. We assume the inverse relationship between ejection velocity and grain size

$$v = v_0 \beta^{\frac{1}{2}} \tag{3.6}$$

where β is the ratio of the acceleration due to solar radiation pressure to the acceleration due to solar gravity and v_0 is the reference velocity for a particle 1 μm in radius (Lisse et al. 1998; Reach et al. 2000; Ishiguro et al. 2007) and $\beta \sim 1/a$ where a is the grain radius in μm. We then can evaluate the average velocity of particles by weighting the velocity by the size distribution and the cross-section of the particles. The average velocity is then

$$\bar{v} = \frac{\int_{a_{min}}^{a_{max}} v_0 \pi a^{\frac{3}{2}} n(a) da}{\int_{a_{min}}^{a_{max}} \pi a^2 n(a) da} \tag{3.7}$$

where n(a)da is the size distribution of dust. This power law distribution is defined as

$$n(a)da = \Gamma a^{-\gamma} da \tag{3.8}$$

where Γ is a constant that does not affect the resulting velocity, and we take $\gamma = 3.5$, as found in other active bodies (e.g. Jewitt et al. 2014). Then, assuming $a_{max} \gg a_{min}$, the resulting average velocity is

$$\bar{v} = \frac{v_0}{2\sqrt{a_{min}}} \tag{3.9}$$

Equation (3.9) shows that, with these assumptions, the average velocity only depends on the minimum particle size. The smallest particles that can be seen in the visible spectrum are limited by diffraction. The scattering efficiency of a particle depends on the size parameter, $x = 2\pi a/\lambda$, where λ is the wavelength of observation. The scattering efficiency approaches 0 as $x \to 0$, and oscillates around and approaches unity as $x \to 1$ (Van de Hulst 1957). In the visible spectrum (λ ~0.5 μm), $x = 1$ corresponds to $a \sim 0.1$ μm. These tiny particles are likely to be dynamically well coupled to the gas and ejected with a velocity that is comparable to the average thermal velocity, given by integrating the Maxwell Boltzman distribution of particle speeds;

$$v_{th} = \sqrt{\frac{8k_BT}{\pi m}}. \tag{3.10}$$

Here the blackbody temperature at ~1.23 AU from the Sun is $T \sim 257$ K, k_B is the Stefan-Boltzmann constant, and m is the mass of an H_2O molecule. Equation (3.10) gives $v_{th} \sim 550$ m s^{-1}, which is our best estimate of the outflow speed in gas. If we assume that the smallest particles, $a \sim 0.1$ μm, are dynamically well coupled to the gas and traveling at v_{th}, then the mean speed $\bar{v}$ ~107 ± 9 m s^{-1} corresponds to effective particle radius $a \sim 3$ μm, by Equation (3.9).

This particle size estimate is clearly approximate, given that we do not know the actual gas flux from the nucleus and that v_{th} is only an approximation to the outflow speed. However, the sunward extent of the coma provides an independent estimate of the particle ejection speed (Jewitt 1991). A particle launched towards the Sun and experiencing a constant anti-solar acceleration of magnitude $\beta g_\odot$ will reach a turn-around distance given by

$$L = \frac{v^2}{2\beta g_\odot}. \tag{3.11}$$

Substituting $v = v_0\beta^{1/2}$, Equation (3.11) simplifies to $L = v_0^2/(2g_\odot)$, where $g_\odot = 4 \times 10^{-3}$ m s^{-2} is the solar gravity at $r_H = 1.23$ AU. We see from Figure (3.1) that the sunward angular extent of the coma is $\sim 10''$ corresponding to $2{\times}10^6$ m at the comet, neglecting the effects of projection. We infer $v_0 \sim (2g_\odot L)^{1/2} \sim 125$ m s^{-1}, corresponding to the speed of a 1 μm particle. This is close enough, given the many approximations involved, that we consider this independent estimate to be in strong support of the result from aperture photometry.

3.4.3 Mass Loss Rate

A simple mass loss rate estimate can be obtained from

$$\frac{dM}{dt} = \frac{4\rho\bar{a}C_e\bar{v}}{3d} \tag{3.12}$$

where ρ is the dust grain density, which we assume again to be 600 kg m^{-3}, $\bar{a}$ is the average particle radius, C_e is the total cross section of all the particles in the measured portion of the coma as given by Equation (3.4), $\bar{v}$ is the average velocity of particles in the coma, and d is the distance traveled. For d, we use the distance from the nucleus to the midpoint of the outer defined region of the coma, d ~190 km. Substituting into Equation (3.12) gives the order of magnitude average mass loss rate $dM/dt \sim 50 \pm 17$ kg s^{-1} where the error is largely dominated by the error on particle size. Finally, we solved the energy balance equation for a patch of perfectly absorbing ice exposed at the subsolar point on the nucleus of 73P. The equilibrium mass loss rate at $r_H = 1.23$ AU is $f_s = 2.9 \times 10^{-4}$ kg m^{-2} s^{-1} (ice temperature 202 K). The measured sublimation rate can thus be supplied by a circular patch of area

$$\pi r^2 = \frac{1}{\delta f_s}\frac{dM}{dt} \tag{3.13}$$

where δ is the dust-to-ice mass ratio. If δ is equal to unity, then $\pi r^2 \sim 0.17 \pm 0.05$ km^2 and $r \sim 0.2$ km, which sets a strong lower limit to the radius of 73P-C. Published estimates of δ vary considerably, but there is now a consensus that $\delta > 1$. For example, Reach et. al (2000) found $\delta \sim$ 10-30 in 2P/Encke, while Fulle et al. (2017) find $\delta = 7.5$ for Comet 67P/Churyumov-Gerasimenko. These larger values would imply an active patch of radius $r \sim$0.04-0.08 km on 73P-C. Evidently, very localized activity on 73P can drive the coma.

3.5 Conclusion

We analyzed 84 images of comet 73P/Schwassmann-Wachmann 3 taken with HST on 2006 April 10 and 11 to find

- The best-fit lightcurve period is $P = 10.38 \pm 0.04$ hours ($2P = 20.76 \pm 0.08$ hours for a double-peaked lightcurve expected for an irregularly shaped body). This eliminates the possibility of rotational instability as a fragmentation mechanism, because the rotation period is above the critical period for breakup due to rotational instability.
- Accounting for dust contamination, our best estimate of the absolute magnitude is $H_V \sim 19.7 \pm 0.7$ corresponding to a nucleus radius $r_n \sim 0.4 \pm 0.1$ km, assuming an albedo of 0.04.
- Phase-lagged brightness variations in the coma show that the dust outflow speed is $v_g = 107 \pm 9$ m s^{-1}, corresponding to average dust particle radius $\bar{a} \sim 3 \pm 1$ μm. The mass loss rate, $dM/dt \sim 50$ kgs^{-1}, is consistent with sublimation of an exposed, ice patch of radius only $\sim$0.2 km.

REFERENCES

[1] Fernández, Y. R. Kelley, M. S. Lamy, P. L. et al. 2013, Icarus, 226, 1138

[2] Ford, H. C. Bartko, F. Bely, P. Y. et al. 1998, Proc. SPIE, 3356, 234

[3] Fulle, M. Della Corte, V. Rotundi, A. et al. 2017, MNRAS, 469, S45

[4] Fuse, T. Yamamoto, N. Kinoshita, D. Furusawa, H. & Watanabe, J.-I. 2007, PASJ, 59, 381

[5] Hartmann, W. K. Tholen, D. J. & Cruikshank, D. P. 1987, Icarus, 69, 33

[6] Ishiguro, M. Sarugaku, Y. Ueno, M. et al. 2007, Icarus, 189, 169

[7] Jewitt, D. C. 1990, 24th ESLAB Symposium, Formation of Stars and Planets and the Evolution of the Solar System, ed. B. Battrick (Friedrichshafen, Germany: ESA) 315, 113

[8] Jewitt, D. 1991, in IAU Colloq. 116: Comets in the Post-Halley Era, ed. R. L. Newburn, Jr. M. Neugebauer, & J. Rahe (Astrophysics and Space Science Library, Vol. 167; Cambridge: Cambridge Univ. Press), 19

[9] Jewitt, D. 1997, Earth Moon and Planets, 79, 35

[10] Jewitt, D. Luu, J. & Trujillo, C. 1998, AJ, 115, 2125

[11] Jewitt, D. Ishiguro, M. Weaver, H. et al. 2014, AJ, 147, 117

[12] Kokotanekova, R. Snodgrass, C. Lacerda, P. et al. 2017, MNRAS, 471, 2974. doi:10.1093/mnras/stx1716

[13] Lamy, P. L. Toth, I. Fernandez, Y. R. & Weaver, H. A. 2004, in Comets II, ed. Festou, M. et al. (Tucson, AZ: University of Arizona Press), 223

[14] Lisse, C. M. A'Hearn, M. F. Hauser, M. G. et al. 1998, ApJ, 496, 971

[15] Marzari, F. Rossi, A. & Scheeres, D. J. 2011, Icarus, 214, 622

[16] Nolan, M. C. Harmon, J. K. Howell, E. S. et al. 2006, DPS Meeting #38, Bulletin of the American Astronomical Society, (Pasadena, CA: DPS) Vol. 38, 504.

[17] Reach, W. T. Sykes, M. V. Lien, D. & Davies, J. K. 2000, Icarus, 148, 80

[18] Ryon, J. E. et al. 2019, ACS Instrument Handbook, Version 18.0 (Baltimore: STScI)

[19] Samarasinha, N. H. 2001, Icarus, 154, 540

[20] Sekanina, Z. 1989, AJ, 98, 2322

[21] Sekanina, Z. 1997, A&A, 318, L5

[22] Storm, S. Samarasinha, N. Mueller, B. et al. 2006, AAS Meeting #209, Bulletin of the American Astronomical Society, (Seattle, WA: AAS) Vol. 38, 935

[23] Tedesco, E. F. 1989, in Asteroids II, ed. Binzel R. et al. (Tucson, AZ: University of Arizona Press),1090

[24] Toth, I. Lamy, P. & Weaver, H. A. 2005, Icarus, 178, 235

[25] Toth, I. Lamy, P. Weaver, H. et al. 2006, DPS Meeting #38, Bulletin of the American Astronomical Society, (Pasadena, CA: DPS) Vol. 38, 489

[26] Toth, I. Lamy, P. L. Weaver, H. A. Noll, K. S. & Mutchler, M. J. 2008, DPS Meeting #40, Bulletin of the American Astronomical Society, (Ithaca, NY: DPS) Vol. 40, 394

[27] van de Hulst, H. C. 1957, Light Scattering by Small Particles (New York: John Wiley & Sons)

[28] Weaver, H. A. Lisse, C. M. Mutchler, M. et al. 2008, Asteroids, Comets, Meteors 2008, 1405, 8248

CHAPTER 4

Hubble Space Telescope Investigation of Fragmenting Comet 73P/Schwassmann-Wachmann 3: 73P-B and -G

This chapter is adapted from the paper titled "Hubble Space Telescope Investigation of Fragmenting Comet 73P/Schwassmann-Wachmann 3: 73P-B and -G", which is in preparation to be submitted to the Astronomical Journal (Graykowski & Jewitt, In Prep.).

4.1 Introduction

Comet 73P/Schwassmann-Wachmann 3 (73P) has been observed to fragment on several occasions. 73P is a Jupiter family comet with a period P = 5.36 years, a semimajor axis a =3.091 AU, inclination i=11.4, and eccentricity e = 0.686. The perihelion distance is q = 0.972 AU. The first reported breakup was observed on UT 1995 September 12, only 10 days before the comet reached perihelion on UT 1995 September 22 (Crovisier et al. 1995). The comet went unobserved during its 2001 perihelion passage, however during its 2006 apparition, it broke into 4 large fragments named 73P-A, -B, -C, and -D. Of these, only fragments 73P-B and 73P-C were long-lived, appearing again at the comet's 2006 apparition. Fragment 73P-C was identified with the primary nucleus of the comet, as it was both the brightest fragment and leading the others in heliocentric orbit (Boehnhardt 2004). During this apparition, while approaching its perihelion (which occurred UT 2006 June 9), the comet disintegrated further into fragments 73-G, -H, -J, -L, -M, and -N. Fragments 73P-B and -G shed hundreds of sub-fragments themselves (Fuse et al. 2007 and Weaver et al. 2008).

Several mechanisms have been proposed to cause comet fragmentation, including tidal disruption (Asphaug and Benz 1994), rotational instability (Jewitt 1997, 2021), the build up of gas pressure in sub-surface pockets (Samarasinha 2001), thermal stress and impact induced fragmentation (Sekanina 1997, Boehnhardt 2004). Tidal disruption is not a viable mechanism for the breakup of 73P, since the comet does not pass within the Roche spheres of any major planet or the Sun. Impacts are statistically improbable and, considering that 73P has fragmented on multiple occasions, the likelihood of multiple impacts is even lower. The rotation period of the primary nucleus, 73P-C, at 20.76 ± 0.08 hr (Graykowski and Jewitt 2019) is too long for rotational instability to be viable. These considerations point to a thermal fragmentation mechanism as the likely mechanism causing 73P's fragmentation. Understanding the fragmentation mechanism of 73P and fragmenting comets in general aids in the understanding of their mass loss and lifetime. Also, for 73P, fragmentation seems to affect the ejection speed of the debris in the dust tail. Due to it's history of fragmenting, Vaubaillon & Reach (2010) showed that the debris of 73P had ejection speeds of up to 2 times higher than predicted by sublimation of water ice. Ye et al. (2022) found that if the ejection speeds of sub-millimeter particles in the dust tail following 73P's 1995 fragmentation event are just 40% higher than predicted, the associated meteor shower in 2022 May could be visible. The magnitude of the meteor showers produced by the tail of 73P can then reveal a lot about the history of the comet, and the effect of fragmentation on mass loss.

In this chapter, we use high angular resolution imaging data from the Hubble Space Telescope in 2006 April to identify hundreds of sub-fragments surrounding fragments 73P-B and G. We measure physical properties including the speed and ejection time of the sub-fragments in order to shed light on the fragmentation mechanism that acted on B and G, and compare our findings to previous work. The HST observations were taken under General Observer program GO 10992 with Harold Weaver as principal investigator and obtained from the MAST archive. These observations have been published only in abstract form (Weaver et al. 2008).

4.2 Observations

The images were taken with the Wide Field Channel (WFC) of the Advanced Camera for Surveys (ACS). The ACS has a field of view of $202'' \times 202''$ and a pixel scale $0.05''$ pixel^{-1} (Ryon et al. 2022), corresponding to about 167 km pixel^{-1} at the distance of the comet. All observations were taken using the F606W filter, centered at wavelength 5922 Å with a full width at half maximum (FWHM) of 2323 Å. In total, 15 images were obtained of 73P-B over three consecutive days: 2006 April 18, 19, and 20 (hereafter referred to as day 1, 2 and 3), with five images taken each day. The first image on each day was exposed for 20 s and the subsequent four images had exposure times of 425 s, all with the telescope tracked to follow the non-sidereal motion of the comet. An additional 5 images of 73P-G were recorded on 2006 April 18, the first again with 20 s exposure time and the subsequent four with 400 s. We used images geometrically-corrected, dither-combined and calibrated in units of electrons/s, created by AstroDrizzle.

Table 4.1 lists the observing geometry for the three days of HST observations of 73P-B and one day of HST observations of 73P-G. Figure 4.1 shows combined images of 73P-B on each day, while 73P-G is shown in Figure 4.2.

UT Date	# Images	t[a]	ΔT_p^b	ν^c	r_H^d	Δ^e	α^f	$\theta_{-\odot}^g$	θ_{-V}^h	$\delta_\oplus^i$
73P-B										
2006 Apr 18	1	20	-49	300.0	1.180	0.227	25.1	208.5	287.0	-35.2
	4	425								
2006 Apr 19	1	20	-48	300.8	1.174	0.220	25.3	207.9	286.8	-35.8
	4	425								
2006 Apr 20	1	20	-47	301.7	1.166	0.211	25.6	207.3	286.5	-36.8
	4	425								
73P-G										
2006 Apr 18	1	20	-49	299.5	1.185	0.231	24.9	207.5	286.8	-34.7
	4	400								

Table 4.1: 73P-B and -G Observing Geometry

[a] Image integration time, in seconds

[b] Number of days from perihelion (UT 2006-Jun-09). Negative numbers indicate pre-perihelion observations

[c] True anomaly, in degrees

[d] Heliocentric distance, in AU

[e] Geocentric distance, in AU

[f] Phase angle, in degrees

[g] Position angle of the projected anti-Solar direction, in degrees

[h] Position angle of the projected negative heliocentric velocity vector, in degrees

[i] Angle between Earth and target orbital plane, in degrees

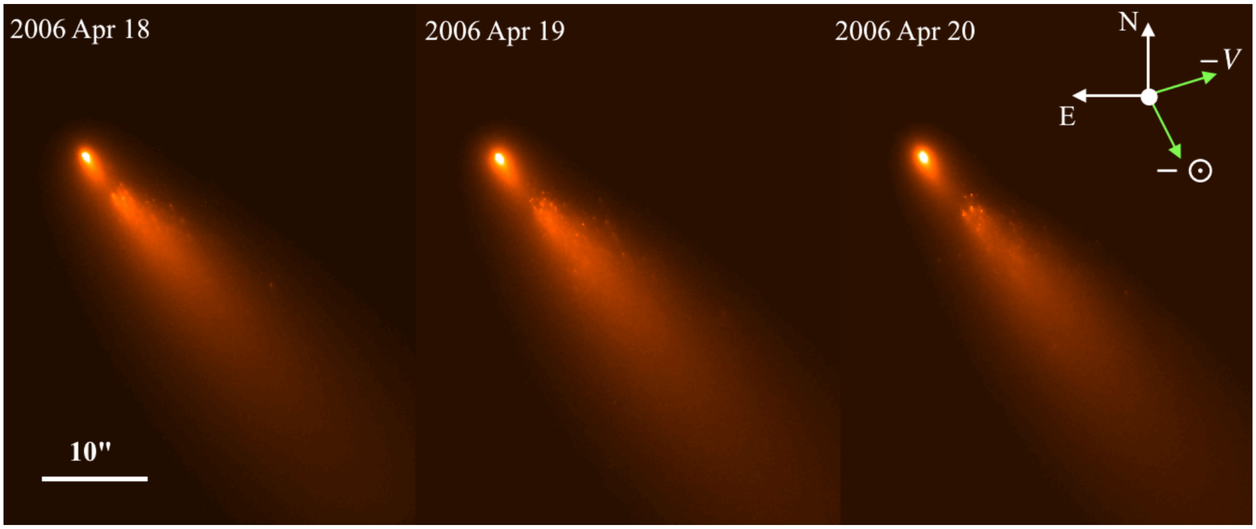

Figure 4.1: 73P-B on 2006 April 18, 19, and 20 - The motion of the fragments in 73P-B is visually evident. Each image is the combination of five images taken with HST's ACS WFC instrument in the F606 filter. The pixel scale is 0.05 x 0.05 square arcseconds. At a distance of 0.23 AU from the Earth, 1 arcsecond corresponds to 167 km. The projected anti-solar direction and negative velocity are represented by the vectors labeled -⊙ and -V respectively.

4.2.1 Fragment Measurements

We identified a total of 461 fragments in addition to the primary fragment (B) near 73P-B and 50 fragments in addition to the primary fragment (G) near 73P-G. Figure 4.3 shows the identified fragments of 73P-B in Days 1, 2 and 3 separately, as well as overlaid on each other. We conducted aperture photometry on each of these fragments. We measured the flux through an aperture of radius 0.15, which corresponds to ∼24 km at the distance of the comet. We chose this aperture size based on the simulated point spread function (PSF) generated using Tiny Tim (Krist et al. 2011), which produced a model PSF with a full-width-half-maximum (FWHM) of about this size. This aperture size allowed us to measure most of the flux (80%), while also avoiding the flux from nearby fragments, and is larger than the measured FWHM (∼ 0.09) of a PSF on the ACS/WFC CCD at the time (Hartig et al. 2002). We subtracted the flux of the sky background and the immediately surrounding coma using a contiguous annulus, which extended another 0.08. It was crucial to use an annulus

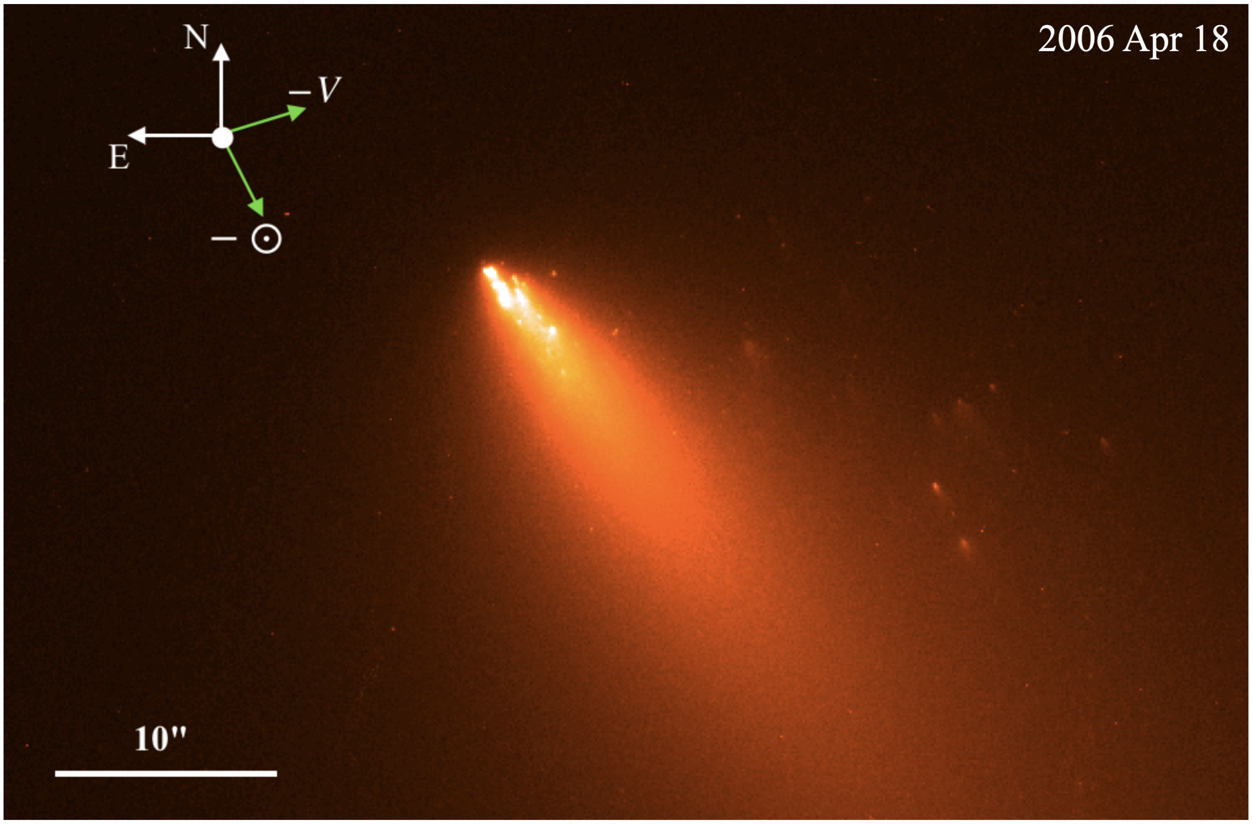

Figure 4.2: 73P-G on 2006 April 18 - Telescope, instrument, and image details are the same as in Figure 4.1

as small as possible, since the fragments were so close together, and embedded in different locations in the coma. Also, some fragments appear to be active themselves, displaying their own coma and tail. For these reasons, it was important to measure the local flux of the surrounding coma of each fragment very carefully. Choosing larger annulus sizes caused the median value of the flux through the annulus to change significantly, especially for fragments closely clustered.

Most fragments appeared faint and shrouded in dust. The faintest have the largest photometric errors and have the highest chance of being confused with incorrectly identified noise in the coma. In order to reconcile this, we identified the number of fragments that are more likely to be noise. The fragments that are most likely to be real are those than can be followed between multiple days of observations. The overlaid data in Figure 4.3 aided

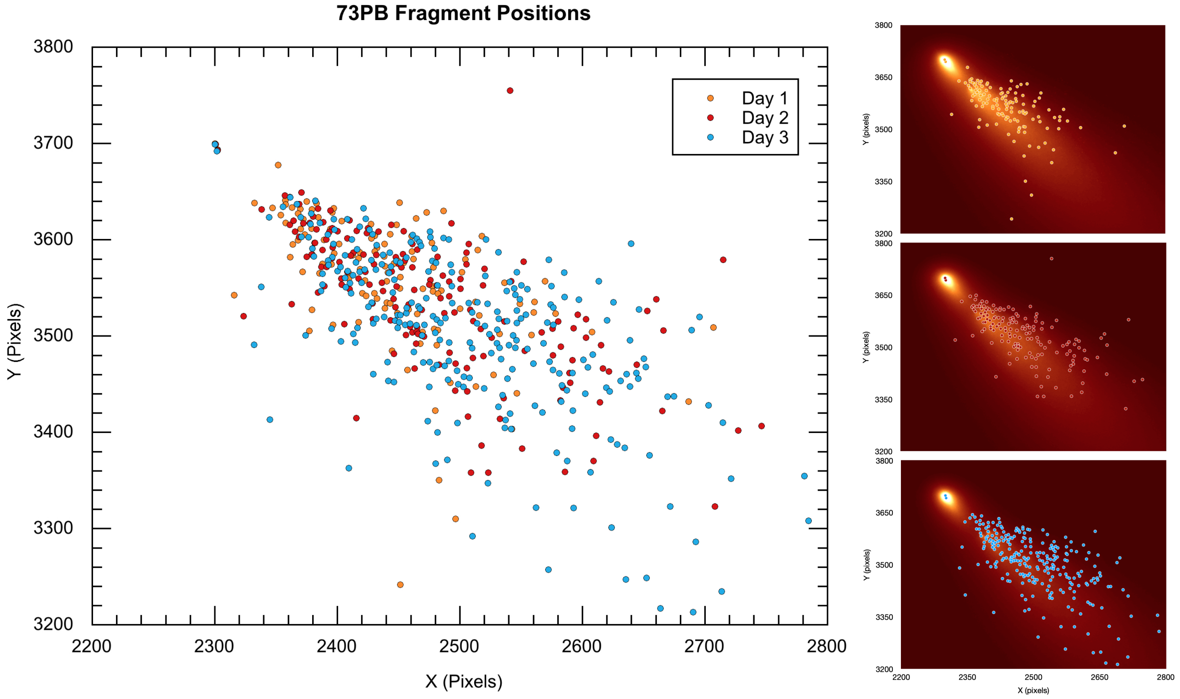

Figure 4.3: 73P-B Fragments - The three images on the right are the same as Figure 4.1 overlaid with a scatter plot of circles representing the pixel location of identified fragments within 73P-B on the CCD. Some fragments persist between all three days while others persist for only one or two days. The scatter plots from each day are overlayed in the image on the left. Orange circles represent fragments identified in the image taken on 2006 April 18 (Day 1), red represents those in the image taken on 2006 April 19 (day 2), and blue represents 2006 April 20 (Day 3). It is visually clear that some fragments persist and relatively move away from the primary fragment from days 1 to 2 to 3, while other fragments appear more ephemeral.

in identifying fragments that appear in multiple days. The faintest fragment that can be observed in at least two days of data has a magnitude of $m_V = 24.71$. Additionally, this fragment was identified in images taken on all three days. We then emphasize that fragments observed on a single day, and fainter than $m_V = 24.71$ are less likely to be real than those brighter. Table 4.2 lists the number of fragments brighter than this minimum.

UT Date[a]	# Fragments[b]	# $m_V < 27.41 \pm 0.39$[c]	Parent Fragment m_V^d
73P-B			
2006 Apr 18 (Day 1)	125	120	18.34 ± 0.06
2006 Apr 19 (Day 2)	160	154	18.32 ± 0.03
2006 Apr 20 (Day 3)	256	231	18.28 ± 0.03
Days 1, 2, and 3	30	-	-
Days 1 and 2	35	-	-
Days 2 and 3	41	-	-
Days 1 and 3	33	-	-
73P-G			
2006 Apr 18 (Day 1)	50	46	22.24 ± 0.09

Table 4.2: 73P-B and -G Fragment Statistics

[a] Date of observations

[b] Number of fragments observed

[c] Number of fragments brighter than the faintest fragment within 73P-B that was observed all three days

[d] Apparent magnitude of the parent fragment (B or G), which is always the brightest fragment

4.3 Results

4.3.1 Dynamics

For Fragment 73P-B, we have time-resolved data, with images taken on 3 consecutive days. This allowed us to measure the velocity of the secondary fragments with relation to primary fragment, B. First we measured the position of each fragment. For each day's worth of images, we measured the positions using a median-combined image. We identified the location of the peak in flux of the fragments based on their radial profiles, as well as their vertical and horizontal linear cross-sections. Using these positions, we measured the distances between the primary and secondary fragments between days 1-2, days 2-3, and days 1-3. The relative velocities of each are shown in Figure 4.4. The larger the distance from the primary fragment, the higher velocity of the secondary fragments, indicating the higher ejection velocity of these fragments. The range of relative velocities measured are ∼0.95 - 6.58 ms^{-1}, not including the closest fragment to parent fragment, B, which measured a low velocity of ∼0.09 ± 0.01 ms^{-1}. These fragments are all assumed to be secondaries, though it is possible that some are tertiary. The best-fit line calculated for each set of data was forced through the origin (representative of the parent fragment, B). The slope of the line then represents the time of fragment ejection. The data are very close to their respective best-fit lines, indicating that the fragmentation mechanism of this event was impulsive and occurred 7.4 ± 0.2 days prior to the observations (prior to 2006 April 20). Also, Figure 4.5 shows histograms of the range of ejection times of the fragments as measured from days 1-2, 2-3, 1-3, and 1-2-3. We find that the histograms, on average, peak at the same ejection time of 7.4 ± 0.2 days prior to 2006 April 20. Between fragments that were observed all three days, we checked for a change in velocity from days 1 and 2 to days 2 and 3. There is no indication of acceleration of the fragments.

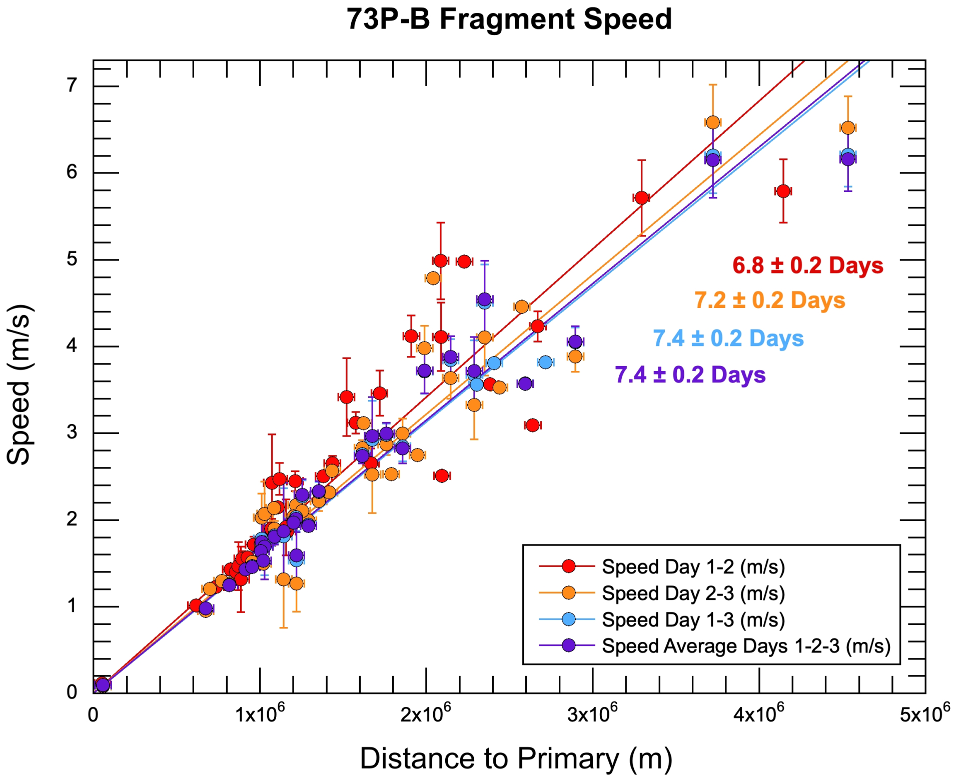

Figure 4.4: Distance of the identified fragments within 73P-B to the primary fragment (B) versus the relative speed of the fragment. Red circles represent the distance and speed of fragments identified in both days 1 and 2. Orange circles represent the fragments identified in both days 2 and 3. Blue represents fragments identified in both days 1 and 3. Purple represents fragments identified in all days 1, 2 and 3. A line was fit to each set of data. The slope of the line then represents the time since ejection of fragments that lie on this line. The data are grouped closely to their corresponding best fit line indicating that the fragments were all released around the same time.

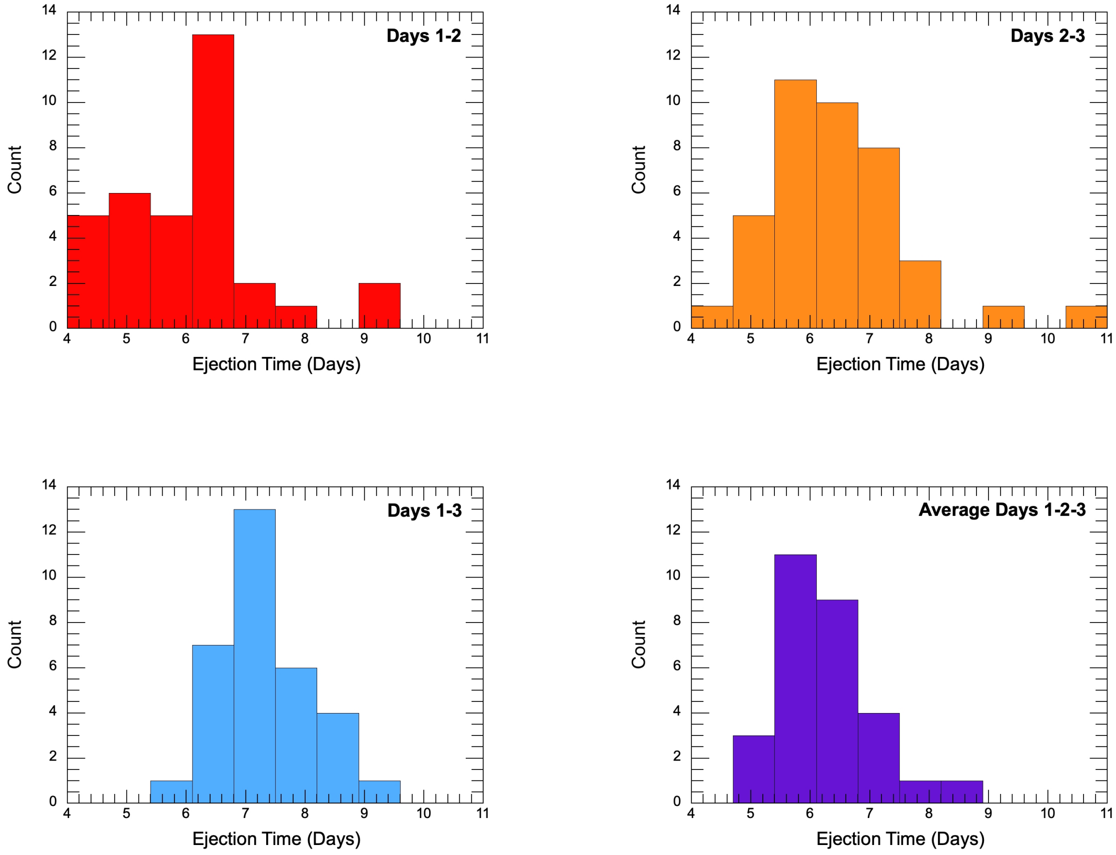

Figure 4.5: Histogram of ejection times of the identified fragments within 73P-B calculated using the speeds and distances from Figure 4.4. Red represents the distance and speed of fragments identified in both days 1 and 2. Orange represents the fragments identified in both days 2 and 3. Blue represents fragments identified in both days 1 and 3. Purple represents fragments identified in all days 1, 2, and 3. The mean ejection times are 6.8 ± 0.2, 7.2 ± 0.2, 7.4 ± 0.2, and 7.4 ± 0.2 days prior to the observations for the red, orange, blue, and purple histograms respectively. This indicates that the fragmentation event occurred ∼UT 2006 April 12-13.

4.3.2 Size Frequency Distribution of Fragments

The calculation of absolute magnitude from apparent magnitude depends on the heliocentric distance, r_H, the geocentric distance, Δ (both in AU) and the phase angle at the observer's location, α (degree). We obtained this information from the JPL Horizons Ephemeris System (`https://ssd.jpl.nasa.gov/horizons.cgi`) to calculate the absolute magnitude of each fragment in every set of observations. The absolute magnitude H_V is calculated as follows:

$$H_V = m_V - 5\log_{10}(r_H \Delta) - f(\alpha) \tag{4.1}$$

where $f(\alpha)$ is the phase function, which represents the angular dependence of the scattered sunlight on α. We assume a linear phase function

$$f(\alpha) = (0.046 \pm 0.017)\alpha \tag{4.2}$$

based on a survey of Jupiter family comets reported by Kokotanekova et al. (2017). We then estimate the cross section of the fragments using

$$C_e = \frac{\pi(2.25 \times 10^{16})}{p_V} 10^{-0.4[H_V - V_\odot]} \tag{4.3}$$

where p_V is the geometric albedo, which we assume to be 0.04 (Hartmann et al. 1987, Lamy et al. 2004, Fernàndez et al. 2013) and $V_\odot \sim$ -26.77 is the apparent magnitude of the Sun. The effective radii of the fragments are then $r = \sqrt{C_e/\pi}$. For parent fragments 73P-B and 73P-G, we find r_B = 353.8 ± 9.7 m and r_G = 58.2 ± 2.4 m respectively. We also measure the effective radius of each fragment and display the results as size frequency distributions (SFDs) in Figures 4.6, 4.7, 4.8, 4.9, and 4.10. Note that, because of the presence of dust surrounding each object, the calculated radii are strictly upper limits to the true radii of the individual fragments. The differential and cumulative size distributions of the cometary fragments can be described by simple power laws within a certain size range. We describe the differential distribution as

$$n(r)dr \propto r^{-q}dr \tag{4.4}$$

where q is the differential index, a constant we aim to calculate. It is then expected that the cumulative size distribution can be described as

$$n(r) \propto r^{1-q} \tag{4.5}$$

We fit power law regressions to the differential SFDs plotted in Figures 4.6, 4.7, 4.8, 4.9, and 4.10 to obtain the differential index, q. We also plot the cumulative SFDs, and overlay variously sloped lines (in log-log space) to guide the eye. We find that the slopes of cumulative SFDs tend to follow ∼1-q as expected from Equation 4.5. There is a stochastic issue with the smaller fragments and an issue with large uncertainties associated with larger fragments, so we limit the power law fits to the differential SFD between sizes r∼10-60 m.

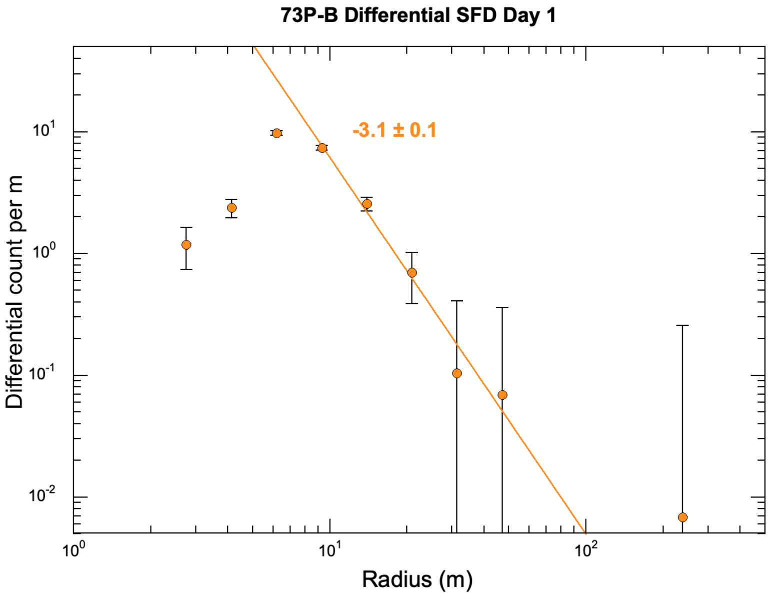

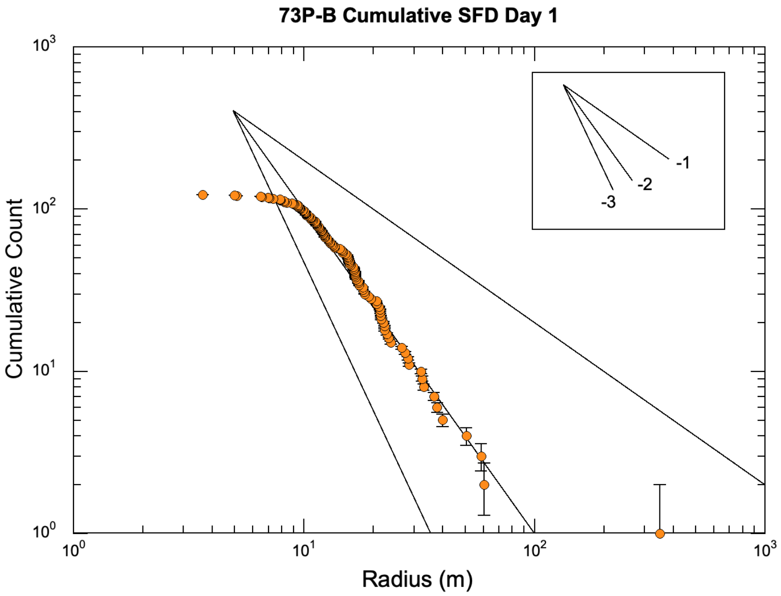

Figure 4.6: 73P-B SFD Day 1 - Top: differential SFD of 73P-B's identified fragments in day 1. A regression power law is fitted to the differential distribution of fragments between radii ∼10-60 meters. We found a differential index of -3.1 ± 0.1 for day 1. Bottom: the cumulative SFD of 73P-B's identified fragments in day 1. The cumulative SFD appear to follow a slope around -2.0, which agrees with the fitted differential indices.

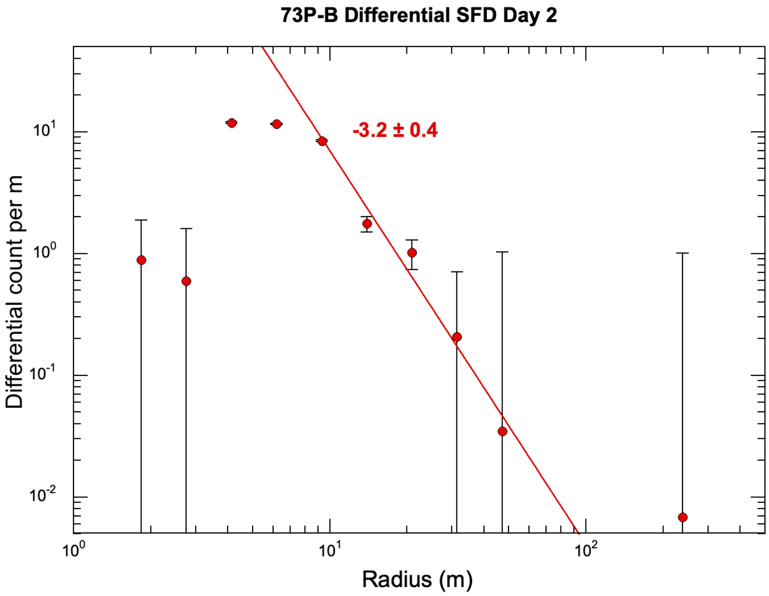

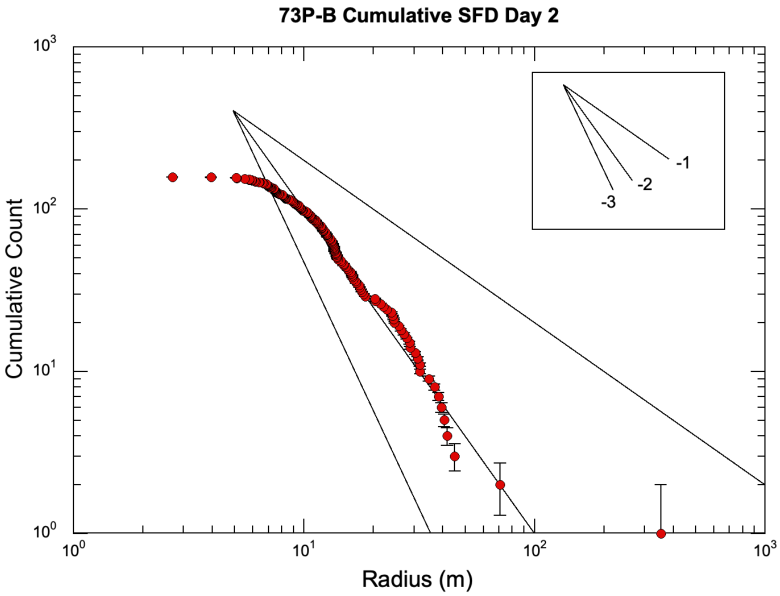

Figure 4.7: 73P-B SFD Day 2 - Top: differential SFD of 73P-B's identified fragments in day 2. A regression power law is fitted to the differential distribution of fragments between radii ∼10-60 meters. We found a differential index of -3.2 ± 0.4 for day 2. Bottom: the cumulative SFD of 73P-B's identified fragments in day 2. The cumulative SFD appear to follow a slope around -2.0, which agrees with the fitted differential indices.

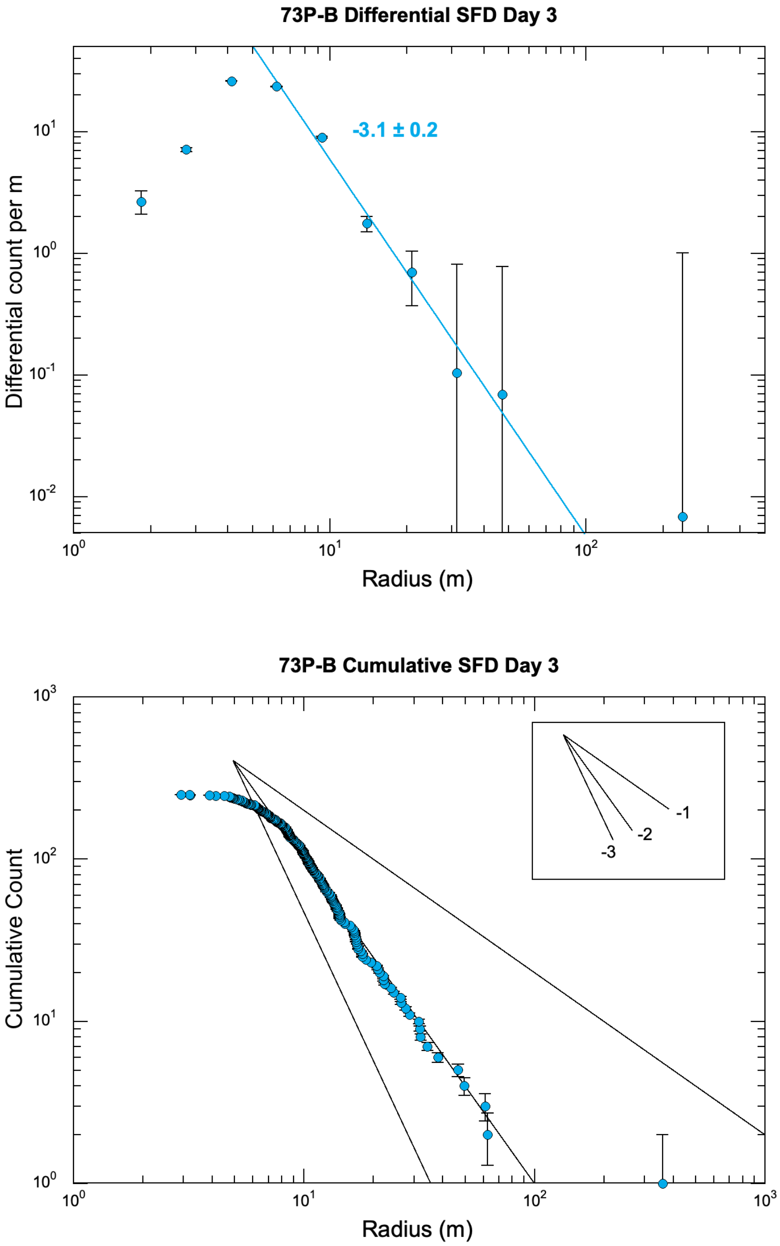

Figure 4.8: 73P-B SFD Day 3 - Top: differential SFD of 73P-B's identified fragments in day 3. A regression power law is fitted to the differential distribution of fragments between radii ∼10-60 meters. We found a differential index of -3.1 ± 0.2 for day 3. Bottom: the cumulative SFD of 73P-B's identified fragments in day 3. The cumulative SFD appear to follow a slope around -2.0, which agrees with the fitted differential indices.

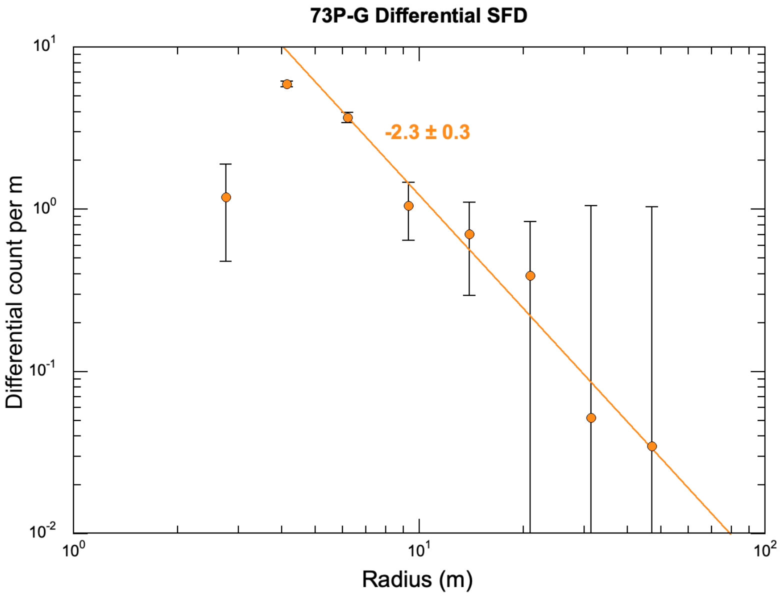

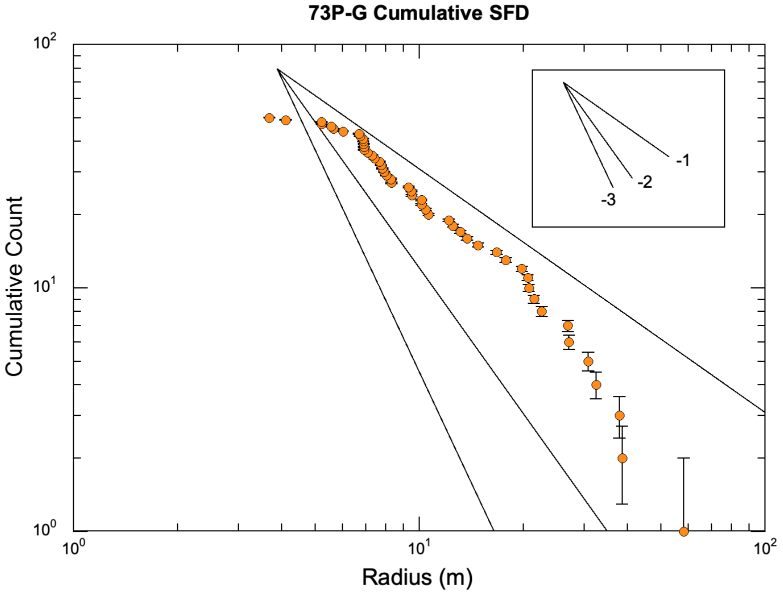

Figure 4.9: 73P-G SFD - Top: the differential SFD of 73P-G's identified fragments. Bottom: same as left except the cumulative SFD instead of differential SFDs. A regression power law was fitted to the differential SFD of fragments between radii ∼6-50 meters. We found a differential index of -2.3 ± 0.3. Bottom: the cumulative SFD appear to follow a slope between -1 and -2, which agrees with the fitted differential index.

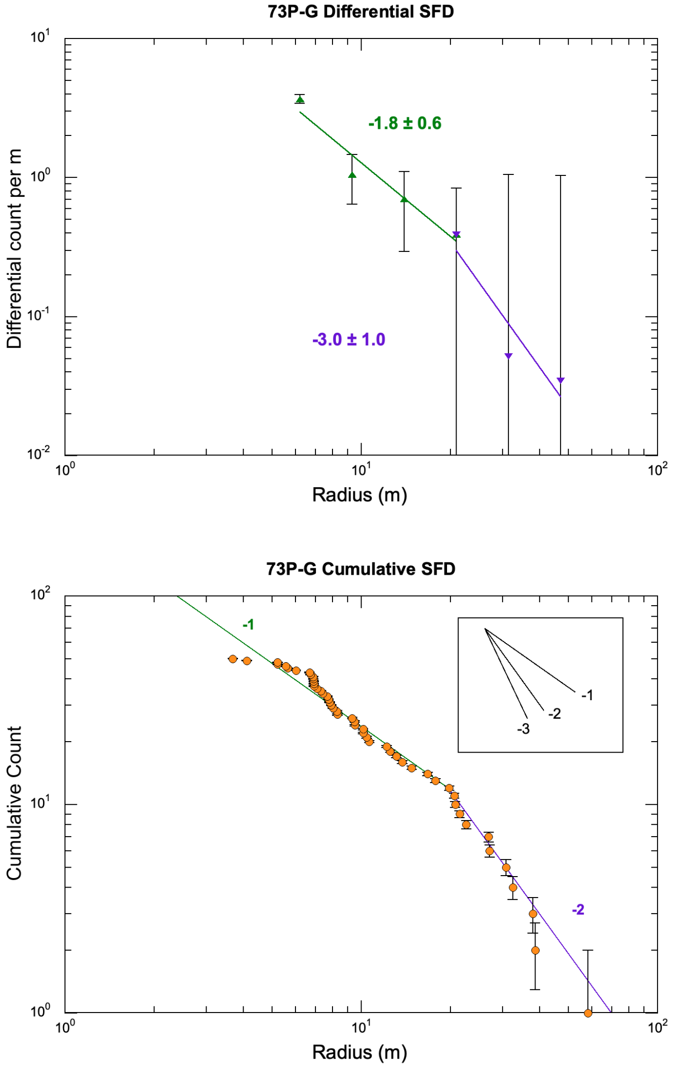

Figure 4.10: 73P-G SFD Assuming a Cusp - Same as Figure4.9, except the ranges of radii within which the power laws were fit are different since both the differential and cumulative SFDs appear to have a possible cusp where the slope changes. This cusp occurs at a radius r∼20 m. Top: the differential SFDs fitted to the distribution of fragments before the cusp in green (smaller fragments) and to the right of the cusp in purple (larger fragments). Bottom: Same as the bottom panel of Figure 4.9, but only slopes of -1.0 (green) and -2.0 (purple) are overlayed on the data, intersecting at the supposed cusp r∼20 m. The fitted differential index of small fragments (green) is -1.8 ± 0.6, which differs significantly from the fitted differential index of large fragments (purple) of -3.0 ± 1.0. The respective cumulative SFDs on either side of the cusp appear to follow slop of -1.0 and -2.0, which agrees with the fitted differential indices.

For 73P-B, the sorted cumulative SFD is plotted for fragments observed on days 1, 2 and 3, displayed on the bottom panels of Figures 4.6, 4.7, and 4.8. Each data point represents the number of fragments with a radius equal or larger than the radius value of that data point. Similarly, the top panels of Figures 4.6, 4.7, and 4.8 display the differential SFDs for the fragments observed on days 1, 2, and 3. The bin sizes were determined by $B_{edge} = N^{B_{\#}}$ where N is a constant which we chose by trial and error, B_{edge} defines the edge of each bin, and $B_{\#}$ is the number of that bin. We started with $B_{edge} = 1$ and $B_{\#} = 0$, and we chose $N = 1.5$. We plotted each data point using the geometric mean of the corresponding bin. We then determined the incremental count within each bin and divided by the bin size, giving the Y-axis units of count/m. The number of fragments with radii between r and $r + dr$ is given by Equation 4.4. We obtain the differential power law index, q, by fitting a power law to the data. We applied a least squares fit of the data within the radius range $r = 9 - 47$ m and found differential indices of $q =$ -3.1 ± 0.1, -3.2 ± 0.4, and -3.1 ± 0.2 for fragments identified in days 1, 2 and 3 respectively. These fits are in good agreement with each other, and are consistent with the cumulative SFDs, which have indices $q + 1 \sim$ -2 in each case, as shown in Figures 4.6, 4.7, and 4.8.

We follow the same methodology for 73P-G, omitting fragments with radii $r < 7$ m where under-counting is significant. For fragments with effective radii in the range $r \sim 7 - 47$ m we obtain a less steep differential index, $q = -2.3 \pm 0.3$. This value is consistent with the cumulative SFD as seen in Figure 4.9. Additionally, both the differential and cumulative SFDs for 73P-G appear to have a cusp, where the slope changes. This cusp occurs at a radius r$\sim$20 m. To investigate this, we fit two power laws to the differential data: one to the smaller fragments to the left of the cusp (radii $r \sim 6 - 20$ m), and one to the larger fragments to the right of the cusp (radii $r \sim 20 - 47$ m). The fitted differential index of small fragments is q = -1.8 ± 0.6, and the differential index of large fragments is q = -3.0 ± 1.0. Although the errors are large, especially for the fit to the small number of larger fragments, the respective cumulative SFDs on either side of the cusp appear to follow power law indices of -1.0 and -2.0, which agrees with the fitted differential indices. The power laws fitted to the SFDs, assuming the cusp is real, are shown in Figure 4.10. Figure 4.11 shows the positions of identified fragments within 73P-G, and distinguishes between the smaller fragments (radii $r \sim 6 - 20$ m) and larger fragments (radii $r \sim 20 - 47$ m) with green and purple circles respectively. It is clear that the small fragments are dominated by fragments that are less shrouded in dust than the larger fragments, and constitute the fragments that are furthest from the parent fragment, 73P-G. The larger fragments are concentrated close to the parent fragment, where the coma is the brightest. Thus this cusp may be a result of observational bias. We emphasize caution in interpreting this potential cusp. The low number of fragments leads to low statistics, and therefore large errors on the differential SFD. In Section 4.4 we compare differential indices to other fragmenting comets and small body populations, and find that there is no trend of index with fragment size. We therefore do not expect to see a cusp, and consider that the cusp may solely be due to observational bias.

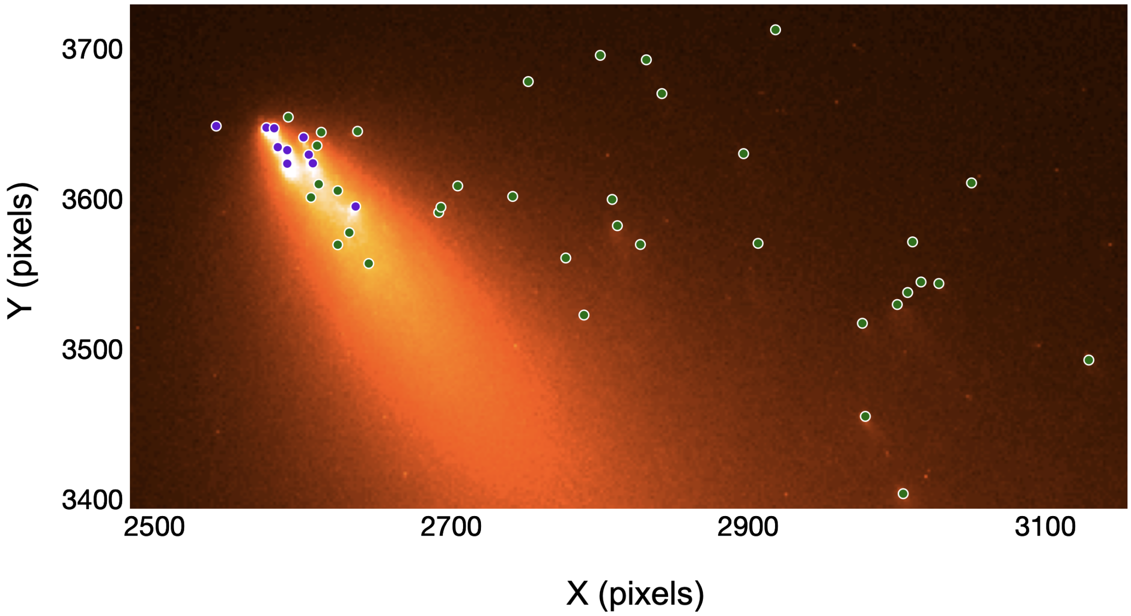

Figure 4.11: The positions of the fragments within 73P-G. The fragments to the right of the cusp (brighter fragments) in the differential SFD from Figure 4.10 are shown in purple, and the positions of the fragments to the left of the cusp (fainter fragments) are shown in green. It is clear that the green data are dominated by fragments that are less shrouded in dust than the purple fragments, which are concentrated close to the parent fragment, G.

4.4 Discussion

The impulsive fragmentation of 73P-B implied by the relative fragment speeds is unlike characteristics observed for fragmentation due to rotational instability. For example, rotational instability is thought to have led to the fragmentation of Comet 332P/Ikeya-Murakami (332P), whose fragments follow an entirely different ejection time distribution than those of 73P-B. Jewitt et al. (2016) showed that the fragments of 332P were ejected over a longer span of time ($\sim$ 40 days) in observations taken in 2016 January and April. This indicates that the fragmentation mechanism for 332P was not impulsive, which supports its potential for rotational instability. It is important to note, however, that multiple fragmentation mechanisms could ultimately lead to the breakup of a comet, and untangling these mechanisms from the aftermath of a single fragmentation event is difficult. From 73P's breakup event in 1995, Wesolowski (2021) showed that an outburst event can lead to a $\sim$3 times increase in sublimation rate. This increased sublimation can then lead to the continued destruction of the comet, regardless of the mechanism that originally led to the outburst event.

Next, we compare the differential indices from this work with indices reported from past works on 73P-B, fragmented comets and active asteroids, boulder distributions on the surfaces of asteroids and comets, comet dust tails, and other populations in Table 4.3.

The differential index we calculated for 73P-G, $q = 2.2 \pm 0.5$, is shallow compared to the differential index we calculated for 73P-B, $q = 3.1 \pm 0.5$. This could be due to the low statistics at 73P-G. Our calculated index for 73P-B agrees with past measurement by Ishiguro et al. (2009), who measured a differential index $q = 3.34 \pm 0.05$ by first fitting the cumulative SFD to find the best-fit cumulative index. The cumulative SFD plotted in Figure 10 of Ishiguro et al. (2009) appears to closely match the cumulative SFDs we plotted in Figures 4.6, 4.7, and 4.8. We therefore have confidence in our results. When comparing the small fragments within 73P-B and -G, to larger fragments of 73P from the 2006 apparition as measured by Reach et al. (2009), we find that the values of q for 73P-B and -G are consistent or are steeper. Reach et al. (2009) found differential indices $q = 1.84$ for fragments $r \lesssim 225$ m and $q = 2.56$ for fragments $r \lesssim 225$ m. We also compare our results to the differential index calculated for recently fragmented comet C/2019 Y4. Ye et al. (2021) found that the differential index varied when measuring the size distribution of different groups of fragments, and appeared to change over time in one case. They found indices $q = 2.5 \pm 0.5$, 4.4 ± 1.4, and 2.0 ± 0.4. This finding highlights the fast changing, ephemeral nature of a comet fragments following a fragmentation event. The fragments of comet 332P/Ikeya-Murakami have a differential index $q = 3.6 \pm 0.6$ (Jewitt et al. 2016), which is steeper than our value for 73P-G, but agrees within the errors on the value for 73P-B.

The differential index for 73P-B is also consistent with $q = 3.5$, the differential index describing a self-similar collisional cascade as described by Dohnanyi (1969). We also find agreement with the differential index of the Kreutz family comets $q = 3.2$ (Knight et al. 2010). However, we find the measurements of boulders on cometary and asteroidal surfaces tend to be steeper with differential indices of $q = 3.7 \pm 0.2$ for boulders on 103P/Hartley 2 (Pajola et al. 2016) and $q = 4.6 \pm 0.3$ for boulders on 67P/Churyumov–Gerasimenko (Pajola et al. 2015). Comet dust tails seem to produce a range of differential indices, some of which agree with our value for 73P-B and some that are both steeper and more shallow. Values range from $q \sim 1.9$ to $q \sim 3.7$ as can be seen in Table 4.3. SPC population surveys have produced differential indices that are in close agreement with our value for the fragments of 73P-B. SPC differential indices range from $q \sim 2.59$ to $q \sim 2.92$.

Most surveys of KBOs consist of objects $r \gtrsim 30$ km and have size distribution with $q \sim 4$ (e.g. Trujillo et al. 2001; Bernstein et al. 2004; Fuentes & Holman 2008; Fraser & Kavelaars 2008). For sizes $r \leq 30$ km, models are used to estimate the size distribution based on coagulation models of initial planetesimal size and collisional cascade models of debris in circumstellar debris disks and find estimates of differential indices that vary with size in the Kuiper belt (Pan & Sari 2005; Pan & Schlichting 2012; Schlichting et al. 2013).

Some values for Kuiper belt populations become quite steep in Table 4.3, as Fraser et al. (2014) implemented a different luminosity function than was used previously to measure the distributions of the Kuiper belt objects based on their absolute magnitudes. The steep differential index of large KBOs may be indicative primordial objects, leftover from planetary accretion. The described models find that while the slopes of the KBO size distribution varies with KBO radius, the smaller KBOs begin to approach shallower slopes, more representative of production by collisional evolution (Pan & Sari, 2005; Pan & Schlichting, 2012; Schlichting et al. 2013).

More differential index comparisons can be seen in Table 4.3. We point out that Table 4.3 is not necessarily a comprehensive list indices for each category, however we find that the lists are sufficiently representative of each category. While comparing the SFDs aids in our understanding of how the small bodies evolved, it is important to note that there seems to be no trend of slope with particle size as seen in Figure 4.12. From this, it appears that for any given size range and population (perhaps except for the KBOs), it is possible to measure a differential index anywhere between ∼2 and ∼4.

Distributions with $q < 4$ are dominated by the largest particles. Therefore, we can estimate the total mass of the fragments that made up 73P-B and 73P-G. However, the fragments with 73P-B and -G are shrouded in dust, and significant fragments may therefore have gone undetected. So, our mass estimate is a lower limit. Assuming density, $\rho = 500$ kg m^{-3} (Jorda et al. 2016), primary fragment 73P-B with a radius $r \leq 354 \pm 7$ m has a mass of $\sim 9.28 \times 10^{10}$ kg. The total mass of all fragments observed on average across the three days of observations, including the primary 73P-B, is $\sim 9.55 \times 10^{10}$ kg. The secondary fragments then make up a mass fraction of $f_M \sim 3.0\%$ of the total mass. Primary fragment 73P-G with a radius $r \leq 58.2 \pm 2.4$ m has a mass of $\sim 4.11 \times 10^8$ kg. The total mass of all fragments observed on average across the three days of observations, including the primary 73P-G, is $\sim 1.04 \times 10^9$ kg. The secondary fragments then make up a mass fraction of $f_M \sim 40.0\%$ of the total mass within the vicinity of 73P-G, indicating a much more destructive event.

Fragments 73P-B and -G have not been observed on subsequent apparitions, supporting the observation of their rapid destruction. During 73P's perihelion passage in 2011, 73P went unobserved. During perihelion passage in 2017, 73P was observed with its primary fragment 73P-C, and a new fragment that has been labeled "73P-Bt". Thus, every time 73P is observed near perihelion passages, new fragmentation events occur. 73P always fragments in the range of it's orbit where temperatures are the highest, further implying that a thermal breakup mechanism is driving the repeated fragmentation.

Body and Aspect	Target	Source	Radius Range (m)	q
Fragmented Comets	**73P-B**	**This Work**	**9-47**	**3.1 ± 0.5**
	73P-B	Ishiguro et al. 2008	10-37	3.34 ± 0.05
	73P-G	**This Work**	**6-47**	**2.3 ± 0.3**
	73P-G	**This Work**	**6-20**	**1.8 ± 0.1**
	73P-G	**This Work**	**20-47**	**3.1 ± 0.2**
	73P	Reach et al. 2009	$\lesssim$ 225	1.84
			$\gtrsim$ 225	2.56
	332P	Jewitt et al. 2016	20-30	3.6 ± 0.6
	C/2019 Y4 (A)	Ye et al. 2021	100-400 m	2.5 ± 0.5
				& 4.4 ± 1.4
	C/2019 Y4 (B)	Ye et al. 2021	100-400 m	2.0 ± 0.4
Fragmented Active Asteroids	331P	Jewitt et al. 2021	40-110	4 - 4.5
Boulders on Comet Surfaces	67P	Pajola et al. 2015	3.5-25	4.6 ± 0.3
	103P/Hartley 2	Pajola et al. 2016	5-33	3.7 ± 0.2
Boulders on Asteroid Surfaces	Bennu	Dellagiustina et al. 2019	4-29	3.9 ± 0.3
	Ryugu	Michikami et al. 2019	2.5-70	3.65 ± 0.05
	Itokawa	Michikami et al. 2008	2.5-15	4.1 ± 0.1
	Itokawa	Mazrouei et al. 2014	3-20	4.4 ± 0.1
Kreutz Family Comets	Survey	Knight et al. 2010	5 - 35 m	3.2

Comet Dust Tails	67P	Marschall et al. 2020	$1 \times 10^{-7} - 3 \times 10^{-5}$	$3.7^{+0.57}_{-0.078}$
	67P	Fulle et al. 2016	$<1 \times 10^{-3}$	3.6 - 4.3
	67P		$>1 \times 10^{-3}$	3.6
	67P	Rinaldi et al. 2017	$1 \times 10^{-6} - 1 \times 10^{-3}$	$3.1^{+3}_{-0.1}$
	67P	Fulle 2004	$1 \times 10^{-6} - 1 \times 10^{-2}$	3.5 - 4.0
	2P/Enke	Ishiguro et al. 2007	$1 \times 10^{-3} - 1 \times 10^{-1}$	3.0 - 3.5
	4P/Faye (tail)	Sarugaku et al. 2007	$<1 \times 10^{-2}$	3.5 ± 0.1
	4P/Faye (trail)		$<1 \times 10^{-2}$	1.9 ± 0.2
	22P/Kopff	Ishiguro et al. 2007	$1 \times 10^{-3} - 1 \times 10^{-2}$	3.25 - 3.5
	65P/Gunn		$1 \times 10^{-4} - 1 \times 10^{-3}$	3.25 - 3.5
Main Belt Asteroids	Survey	Kuiper et al. 1958	5×10^{3} - 5×10^{4}	~2.8 ±0.04
	collisional model	Dohnanyi 1969	5×10^{4} - 5×10^{6}	~3.5
	Survey (SDSS)	Yoshida & Nakamura 2007	200 - 2.5×10^{3}	~2.3
	Survey (SMBAS-II)		300 - 500	~2.3
	Survey(inner belt)	Jedicke & Metcalfe 1998	4.25×10^{3} - $\sim 1 \times 10^{4}$	2.615
			2.25×10^{3} - 4.25×10^{3}	3.790
			450 - 2.25×10^{3}	2.240
	Survey(middle belt)		5.5×10^{3} - $\sim 1.5 \times 10^{4}$	3.68
			700 - 5.5×10^{3}	2.435
	Survey(outer belt)		1.25×10^{4} - $\sim 6 \times 10^{4}$	2.225
			5×10^{3} - 1.25×10^{4}	2.750
			1.15×10^{3} - 5×10^{3}	2.250
Jovian Trojans	Survey	Jewitt & Trujillo 2000	2.2×10^{3} - 2.0×10^{4}	3.0 ± 0.3

Irregular satellites	Survey	Sheppard & Jewitt 2003; Jewitt & Sheppard 2005	1×10^3 - 8.5×10^4	$\sim$2.0
Short Period Comets	Survey	Meech et al. 2004	$1 \times 10^3 - 1 \times 10^4$	2.45 ± 0.05
	Survey		$2 \times 10^3 - 5 \times 10^3$	2.91 ± 0.06
	Survey	Fernandez et al. 2013	$1.4 \times 10^3 - 9 \times 10^3$	2.92 ± 0.23
	Survey	Weissman and Lowry 2003	$1.4 \times 10^3 - 9 \times 10^3$	2.59 ± 0.03
KBOs	Survey	Trujillo et al. 2001	$5 \times 10^4 - 1 \times 10^5$	$4.0^{+0.6}_{-0.5}$
	Model	Pan and Sari 2005	$<4 \times 10^4$	2.88 - 3.14
	Survey (hot)	Fraser et al. 2014	$7 \times 10^4 - 5 \times 10^5$	$5.3^{+0.43}_{-1.2}$
	Survey (cold)		$7 \times 10^4 - 5 \times 10^5$	$8.5^{+2.3}_{-1.1}$
	Cratering SFD extrapolation	Morbidelli et al. 2021	10 - 1×10^3	2.0 - 2.2

Table 4.3: Differential Indices of Small Bodies - Note: this is not a comprehensive list.

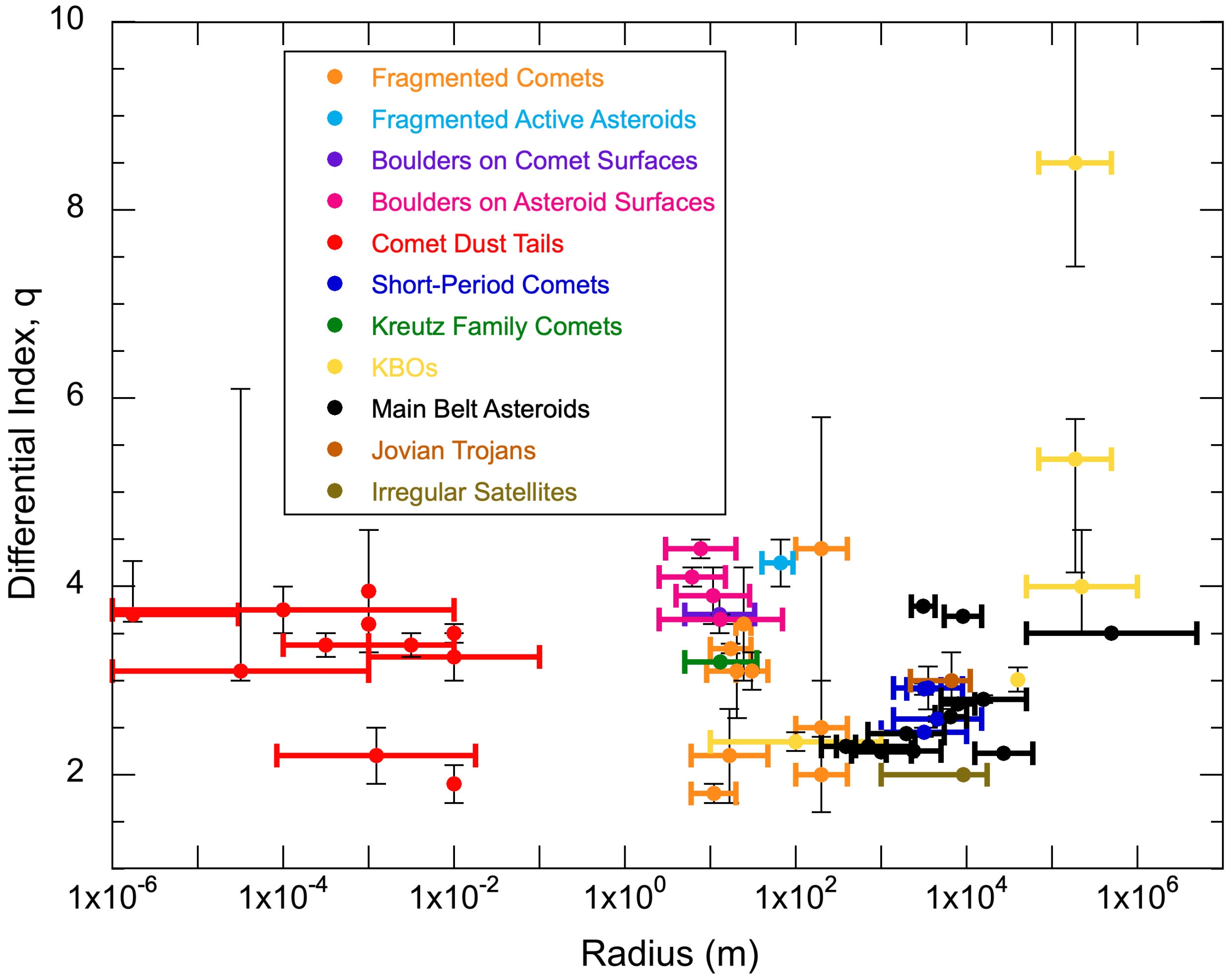

Figure 4.12: Comparison of Differential Indices of Small Bodies - The differential indices, q, are plotted with object radii (m) from Table 4.3. The horizontal bars represent the range of sizes within which the associated index was calculated. The vertical bars represent the reported errors on q. Except for the hot and cold KBO population indices measured by Fraser et al. (2014), all of the indices fall somewhere between $q \sim 2$ and $q \sim 4$, with no apparent dependence on object size.

4.5 Summary

From a high resolution study of fragmenting comet 73P/Schwassmann-Wachmann 3 we find

- the secondary fragments within 73P-B have a range of velocities, v$\sim$0.95 - 6.58 ms^{-1}, relative to the motion of primary fragment 73P-B. The distribution of fragment velocities indicate an impulsive ejection time that occurred 7.4 ± 0.2 days prior to the observations (prior to 2006 April 20). The implication on the fragmenting mechanism, is that the mechanism must have been impulsive. This implication is not consistent with rotational instability, but is more consistent with thermally induce fracture or pressure build up. The repeated nature of the fragmentation of 73P each perihelion passage further implies a thermally induced mechanism. These findings are also consistent with the finding that 73P-C (the nucleus) is rotating too slowly to be rotationally unstable as of 2006 (Graykowski & Jewitt, 2017). While these observations do not prove or disprove a fragmentation mechanism for certain, they do all consistently point towards thermally induced mechanisms.
- a differential index $q = 3.1 \pm 0.5$ for the distribution of the secondary fragments shed from 73P-B and a differential index $q = 2.2 \pm 0.5$ for the distribution of the secondary fragments shed from 73P-G.
- the mass of 73P-B is $\sim 9.28 \times 10^{10}$ kg ($r \leq 354.0 \pm 7.0$ m) and the lower limit on the total mass including all the secondary fragments is $\sim 9.55 \times 10^{10}$ kg. We also find the mass of 73P-G is $r \leq 58.2 \pm 2.4$ kg ($r \leq 58.2 \pm 2.4$ m) and the lower limit on the total mass including all the secondary fragments is $\sim 1.04 \times 10^{9}$ kg.

REFERENCES

[1] Asphaug, E. & Benz, W. 1996, Icarus, 121, 225

[2] Boehnhardt, H. 2004, Comets II, 301

[3] Crovisier, J., Biver, N., Bockelee-Morvan, D., et al. 1995, IAU Circ., 6227

[4] Dellagiustina, D. N., Emery, J. P., Golish, D. R., et al. 2019, Nature Astronomy, 3, 341

[5] Dohnanyi, J. S. 1969, J. Geophys. Res., 74, 2531

[6] Fernández, Y. R., Kelley, M. S., Lamy, P. L., et al. 2013, Icarus, 226, 1138

[7] Fraser, W. C., Brown, M. E., Morbidelli, A., et al. 2014, ApJ, 782, 100

[8] Fraser, W. C., & Kavelaars, J. J. 2008, AJ, 137, 72

[9] Fuentes, C. I. & Holman, M. J. 2008, AJ, 136, 83

[10] Fulle, M., Marzari, F., Della Corte, V., et al. 2016, ApJ, 821, 19

[11] Fuse, T., Yamamoto, N., Kinoshita, D., et al. 2007, PASJ, 59, 381

[12] Graykowski, A. & Jewitt, D. 2019, AJ, 158, 112

[13] Graykowski, A. & Jewitt, D. 2022, in prep

[14] Hartig, G. F., Ford, H. C., Illingworth, G. D., et al. 2002,

[15] Hartmann, W. K., Tholen, D. J., & Cruikshank, D. P. 1987, Icarus, 69, 33

[16] Ishiguro, M., Sarugaku, Y., Ueno, M., et al. 2007, Icarus, 189, 169

[17] Ishiguro, M., Usui, F., Sarugaku, Y., et al. 2009, Icarus, 203, 560

[18] Jedicke, R. & Metcalfe, T. S. 1998, Icarus, 131, 245

[19] Jewitt, D. 1997, Earth Moon and Planets, 79, 35

[20] Jewitt, D., Li, J., & Kim, Y. 2021, AJ, 162, 268

[21] Jewitt, D., Mutchler, M., Weaver, H., et al. 2016, ApJ, 829, L8

[22] Jewitt, D. & Sheppard, S. 2005, Space Sci. Rev., 116, 441

[23] Jewitt, D. C., Trujillo, C. A., & Luu, J. X. 2000, AJ, 120, 1140

[24] Jorda, L., Gaskell, R., Capanna, C., et al. 2016, Icarus, 277, 257

[25] Knight, M. M., A'Hearn, M. F., Biesecker, D. A., et al. 2010, AJ, 139, 926

[26] Kokotanekova, R., Snodgrass, C., Lacerda, P., et al. 2017, MNRAS, 471, 2974

[27] Krist, J. E., Hook, R. N., & Stoehr, F. 2011, Proc. SPIE, 8127

[28] Kuiper, G. P., Fujita, Y., Gehrels, T., et al. 1958, ApJS, 3, 289

[29] Lamy, P. L., Toth, I., Fernandez, Y. R., et al. 2004, Comets II, 223

[30] Marschall, R., Markkanen, J., Gerig, S.-B., et al. 2020, Frontiers in Physics, 8, 227

[31] Mazrouei, S., Daly, M. G., Barnouin, O. S., et al. 2014, Icarus, 229, 181.

[32] Meech, K. J., Hainaut, O. R., & Marsden, B. G. 2004, Icarus, 170, 463

[33] Michikami, T., Honda, C., Miyamoto, H., et al. 2019, Icarus, 331, 179

[34] Michikami, T., Nakamura, A. M., Hirata, N., et al. 2008, Earth, Planets and Space, 60, 13

[35] Morbidelli, A., Nesvorný, D., Bottke, W. F., et al. 2021, Icarus, 356, 114256

[36] Pan, M. & Sari, R. 2005, Icarus, 173, 342

[37] Pan, M. & Schlichting, H. E. 2012, ApJ, 747, 113

[38] Pajola, M., Lucchetti, A., Bertini, I., et al. 2016, A&A, 585, A85

[39] Pajola, M., Vincent, J.-B., Güttler, C., et al. 2015, A&A, 583, A37

[40] Reach, W. T., Vaubaillon, J., Kelley, M. S., et al. 2009, Icarus, 203, 571

[41] Rinaldi, G., Della Corte, V., Fulle, M., et al. 2017, MNRAS, 469, S598

[42] Ryon, J. E. 2022, ACS Instrument Handbook for Cycle 30 v. 21.0, 21

[43] Sarugaku, Y., Ishiguro, M., Pyo, J., et al. 2007, PASJ, 59, L25

[44] Samarasinha, N. H. 2001, Icarus, 154, 540

[45] Schlichting, H. E., Fuentes, C. I., & Trilling, D. E. 2013, AJ, 146, 36

[46] Schlichting, H. & Pan, M. 2013, American Astronomical Society Meeting Abstract, 221, 220-06

[47] Sekanina, Z. 1981, Annual Review of Earth and Planetary Sciences, 9, 113

[48] Sekanina, Z. 1997, A&A, 318, L5

[49] Sheppard, S. S. & Jewitt, D. C. 2003, IAU Special Session, 1, 31

[50] Trujillo, C. A. & Brown, M. E. 2001, ApJ, 554, L95

[51] Vaubaillon, J. J. & Reach, W. T. 2010, AJ, 139, 1491

[52] Weaver, H. A., Lisse, C. M., Mutchler, M., et al. 2008, Asteroids, Comets, Meteors 2008, 1405, 8248

[53] Weissman, P. R. & Lowry, S. C. 2003, Lunar and Planetary Science Conference

[54] Wesołowski, M. 2021, NA, 89, 101626

[55] Ye, Q., Jewitt, D., Hui, M.-T., et al. 2021, AJ, 162, 70

[56] Ye, Q., Vaubaillon, J., & Desmars, J. 2022, arXiv:2205.124

[57] Yoshida, F. & Nakamura, T. 2007, Planet. Space Sci., 55, 1113

CHAPTER 5

Conclusion and Future Prospects

5.1 Irregular Satellites

5.1.1 Color and Shape Survey Summary

The color survey covered in Chapter 2 is the most comprehensive irregular satellite color survey across all of the giant planets (Graykowski & Jewitt, 2018). We found that the colors of the irregular satellites of the giant planets are similar to each other, independent of heliocentric distance, and lack the ultrared matter that colors the surfaces of many Kuiper belt objects. If the irregular satellites were captured from the Kuiper belt, then their surface colors must have been modified, and the modification process must have been non-thermal. We find that collisional shattering likely determines the shapes in both types of object, implying that collisional resurfacing is a possible mechanism to evolve the surface colors of the irregular satellites. These findings have been further supported. Peña & Fuentes (2022) measure the optical colors of 21 Saturnian irregular satellites, expanding on the amount of irregular satellite colors measured at Saturn, and they find that the colors are consistent with the colors reported by Graykowski & Jewitt (2018) and also ultimately lack ultrared matter.

5.1.2 Future Prospects of Irregular Satellite studies

While the color survey we conducted is the most comprehensive color survey of the irregular satellites across the giant planets, the color data of the populations at Uranus and Neptune are lacking. Only 5 of 9 known irregular satellites of Uranus and 2 of 7 known irregular satellites at Neptune are represented (Graykowski & Jewitt, 2018). With large telescopes like Keck, it is possible to obtain the colors of all 9 Neptunian and 7 Uranian irregular satellites, as they are all predicted to have apparent magnitudes h $<$ 25.0, the faintest magnitude observed in Graykowski & Jewitt (2018). Additionally, with the upcoming opening of the Vera C. Rubin Observatory and the recent launch of the James Webb Space Telescope (JWST), small body astronomy will expand greatly. The Vera C. Rubin observatory will increase the discovery rate of small bodies, and this will include moons of the giant planets. I expect the population sizes of irregular satellites of Uranus and Neptune to begin approaching that of Jupiter and Saturn. JWST will allow astronomers to gather greater details on the physical parameters of the surface of small bodies than before. For example, in cycle 1 of JWST's General Observer Program, observing time was awarded to measure IR spectra of 5 Jovian Trojans of the Lucy Mission targets under principal investigator Michael Brown (proposal ID: GO 2574). To complement this, it would then be extremely beneficial to conduct a similar study on a comparable sample of Jovian irregular satellites, as both populations have been proposed to originate from the OPD (Morbidelli et al. 2005; Nesvorný et al. 2013). As pointed out in Chapters 1 and 2, with current observations, the irregular satellites appear to be collisionally evolved, whereas the Jovian Trojan population appears much less collisionally evolved, indicating differences in early evolution of the populations. The colors of the Jovian Trojans and the irregular satellites, however, appear to be very similar as seen from Figure 2.6. Comparing detailed near-infrared spectra of these two small body populations will help us better understand the origin and evolutionary similarities and differences between the two. This can also be applied to other small body populations as well. As we discover more and expand our understanding of the irregular satellites in context of other small body populations, we will be able to define the origin and evolution of our solar system.

5.1.3 Past and Future Spacecraft Missions to Irregular Satellites

Some irregular satellites have been visited by spacecraft as secondary goals to their primary mission. For example, the Cassini spacecraft, launched October 1997 to study Saturn, flew by and imaged a Jovian and some Saturnian irregular satellites en route. In December 2000, Cassini imaged Jovian irregular satellite Himalia, the largest Jovian irregular and primary member of the Himalia collisional family. Cassini images of Himalia can be seen in Figure 5.1. Dimensions measured from these images were 150 ± 20 km by 120 ± 20 km (Porco et al. 2003). the phase angle at which the images were taken suggest that these measurements were lower limits on the size. This agreed with ground based measurements, which estimated the diameter of Himalia to be ~170 km (Cruikshank et al. 1982). The measurements from the spacecraft and the ground-based flux measurements allowed for a new estimation of albedo (0.05 ± 0.01), which is consistent with a carbonaceous asteroidal surface (Porco et al. 2003). in February 2007, the New Horizons spacecraft also took distant images of Himalia as well as Elara.

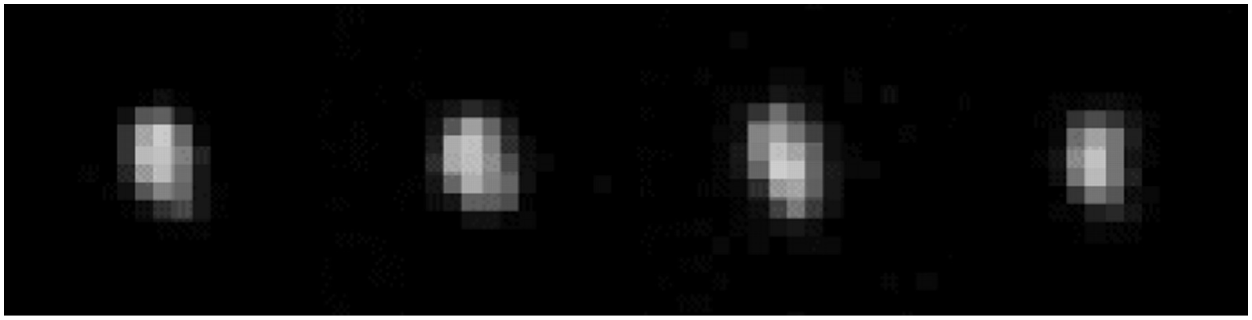

Figure 5.1: Himalia Imaged by Cassini - Himalia over 4.5 hours as viewed by the Cassini Imaging Science Subsystem at a phase angle of 70°. The images begin on 18 December 2000 and end on 19 December 2000. Figure adapted from Porco et al. (2003).

Cassini also imaged 25 Saturnian irregular satellites. The spacecraft also took high resolutions images of Saturn's largest irregular satellite, Phoebe, which can be seen in Figure 5.2. The images revealed a heavily cratered body, reaching a resolution of a few tens of meters. Many large craters were observed (130 craters with diameter D $\geq$ 10 km), but none large enough to represent an impactor that would deliver enough energy to disrupt the body (Jewitt & Haghighipour, 2007). Phoebe does not appear to be part of a collisional family, and these Cassini crater observations enhance that conclusion. The other 24 irregular satellites observed by Cassini were much farther way, and appear as point sources in the images. Lightcurves were obtained for these bodies, and the measured rotation periods ranged from ∼5.5 - ∼76 h (Denk & Mottola 2019). None are near rotational instability.

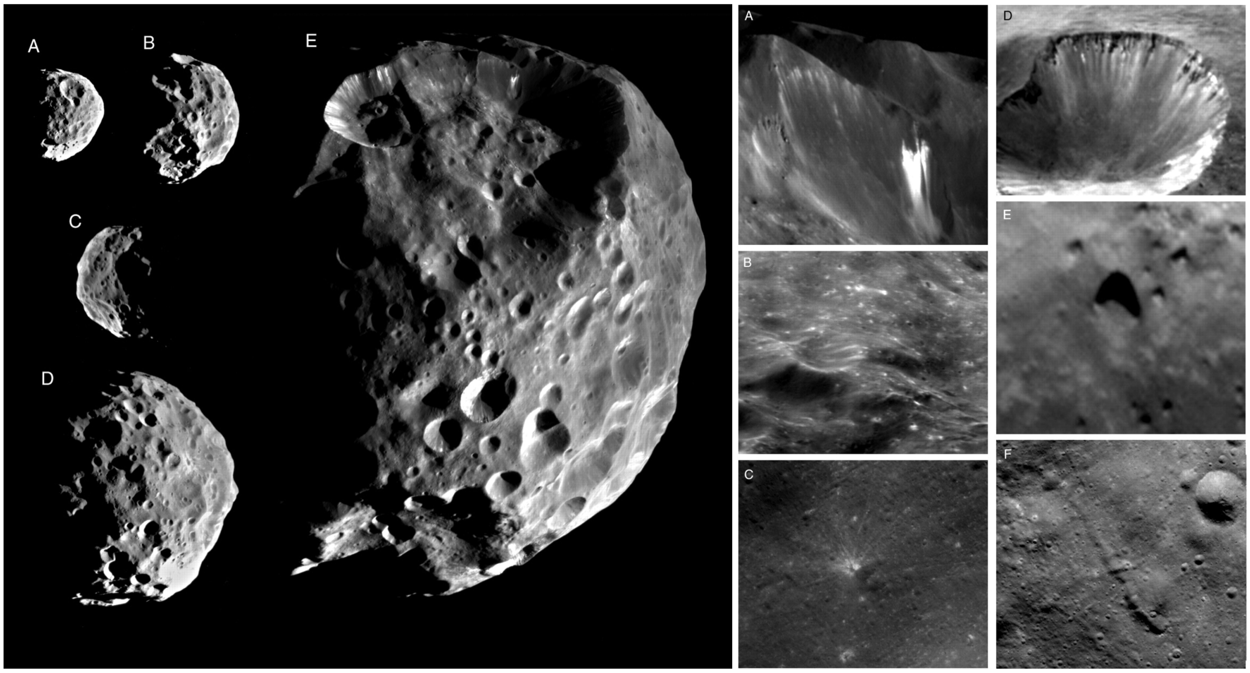

Figure 5.2: Phoebe Imaged by Cassini - Left: 5 different global views (A-E) of Phoebe images at a phase angle of 84°. Right: details of Phoebe's morphology. A: bright, down-slope streamers in Jason crater; B: bright markings surrounding small craters; C: crater with bright rays; D: crater with banding; E: ejecta blocks at the bottom of a crater; F: Elongate depression. Adapted from Porco et al. (2005).

The Voyager 2 spacecraft also observed Phoebe, aiding in gravitational measurements. Voyager 2 also observed Triton and Nereid of Neptune in 1989, helping to accurately measure their sizes and albedos. Triton is the largest irregular satellite with a diameter of 2706 ± 2 km, and appears icy and crater free as seen in Figure 5.3. Its strikingly young surface makes Triton an interesting target for future space missions, and understanding its origin as an irregular satellite is therefore crucial in order to understand the origin and evolution of Triton and of the irregular satellites in general. Because of its large size, the potential capture mechanisms are difficult to implement as summarized by Jewitt and Haghighipour (2007). As described in Chapter 1, three-body interactions seem to be the most likely capture mechanism for this large irregular satellite (e.g. Goldreich et al. 1989; Agnor & Hamilton 2006).

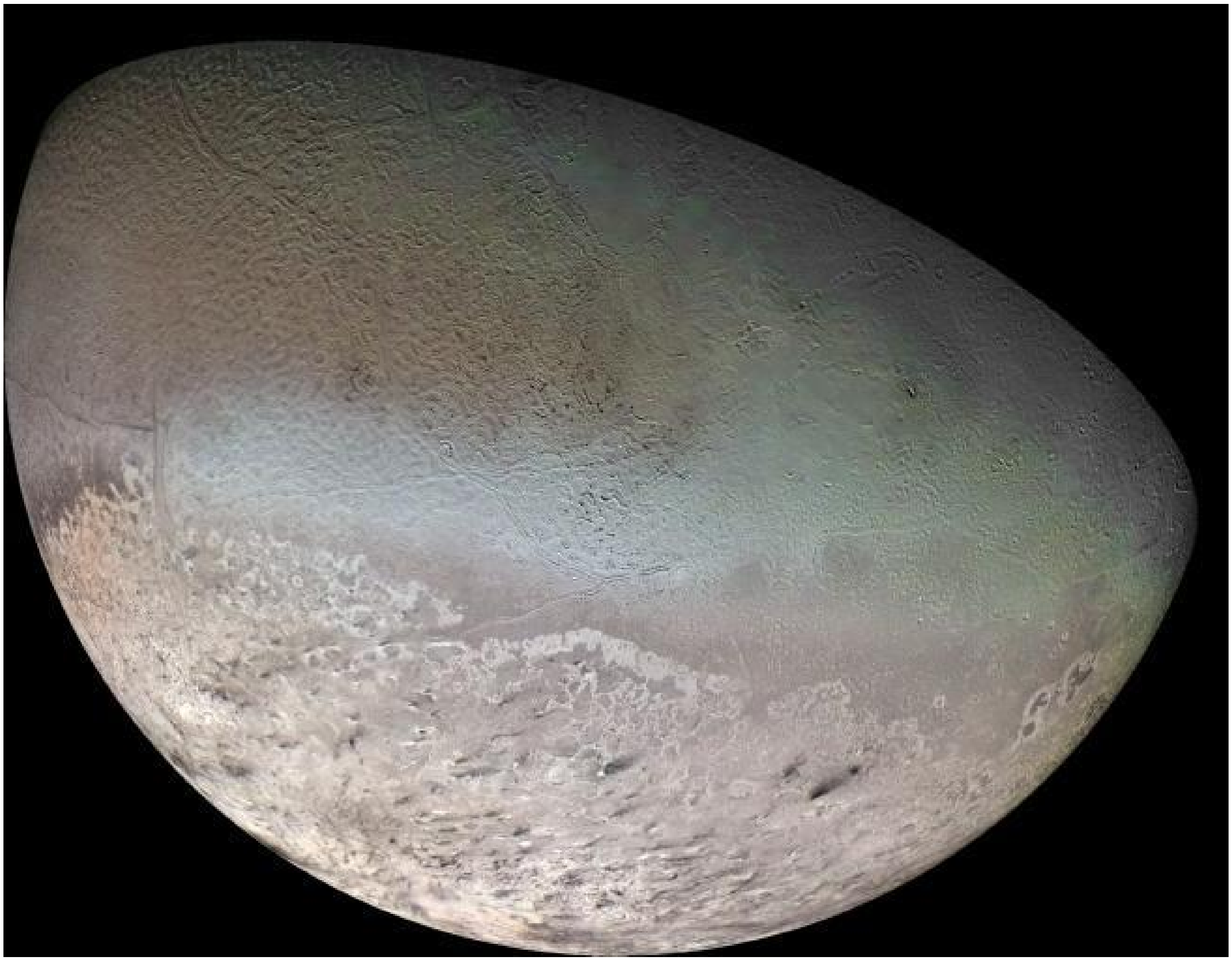

Figure 5.3: Triton Imaged by Voyager 2 - This mosaic of images from the Voyager 2 spacecraft showing the young, largely crater-free, icy surface. Image courtesy of NASA/JPL/USGS

Despite these spacecraft data, composition of irregular satellite surfaces is still a mystery. For example, ground-based optical reflectance spectra and near-infrared spectra have been taken for Himalia, but are largely featureless and noisy leading to claims of both a missing spectral feature that would be indicative of water as well as the weak detection of another feature also indicative of water (e.g. Luu 1991; Jarvis et al. 2000; Vilas et al. 2006; Chamberlain & Brown 2004). These ambiguous results call for high resolution spectral studies of the irregular satellites, especially as a complement to the upcoming Lucy mission as suggested above, in Section 5.1.2. Upcoming spacecraft have the ability to image some of the irregular satellites as well. The European Space Agency's (ESA) spacecraft Jupiter Icy Moons Explorer (JUICE) is set to launch in 2023 with the aim of observing Ganymede, Callisto, and Europa (Grasset et al. 2013). JUICE also aims observe some of the Jovian irregular satellites, though much less spatially resolved than these three main targets. Similarly, NASA's Europa Clipper mission is planned to launch in 2024 with the aim of orbiting and studying Europa (Lam et al. 2018). While its primary target is Europa, observing the Jovian irregular satellites is suggested as a secondary science goal for the craft, with the aim to take spectral observations in order to understand the potential source regions of the bodies based on their surface composition (Sayanagi et al. 2021). These data along with the Vera C. Rubin Observatory, and JWST, will provide the next big step in our understanding of the origin and evolution of the irregular satellites.

5.2 Fragmenting Comets

5.2.1 Fragmentation of 73P Summary

We aim to understand the physical processes that cause comets to fragment as well as the dynamical processes of the fragments, aiding in the understanding of their evolution throughout their lifetime in the solar system. Fragmentation could be the primary cause of a comet's mass loss and eventual destruction, and could therefore be the most important process of comet evolution in our solar system. Many dynamical studies of comet lifetime estimations do not include fragmentation in the model. Nesvorný et al. (2017) use the heliocentric distance of the comet at perihelion, the time spent close to the sun, and the number of perihelion passages in order to determine the lifetime of short period comets. This model then will estimate lifetimes based on the mass loss due solely to the sublimation of the comet. Di Sisto (2009) shows that if various split rates are assumed, the estimated lifetimes of the short period comets would be reduced. This is important because, in a steady state, the rate of comets supplied by the Kuiper Belt and Oort Cloud should be equivalent to the rate of destruction. If the lifetimes of the comets are short, the supply would need to be large enough to compensate. Therefore, measuring the effect of fragmentation on the lifetime of a comet is crucial in order to estimate the supply rate and understand the population of the cometary source regions in our solar system. The ability to differentiate the various fragmentation mechanisms (tidal, rotational, thermal, outgassing pressure, and impact-induced) through observations of a comet's physical characteristics aids in the prediction of cometary fragmentation. Understanding these effects can further aid in the calculation of mass loss, and therefore the estimation of cometary lifetime.

We looked at a specific comet, 73P/Schwassmann-Wachmann 3, as a case-study of fragmentation. We first analyzed 84 images of the nucleus 73P-C taken with HST on 2006 April 10 and 11 (Graykowski & Jewitt 2019). We found that the best-fit lightcurve period is $P = 10.38 \pm 0.04$ hours ($2P = 20.76 \pm 0.08$ hours for a double-peaked lightcurve expected for an irregularly shaped body). This rotation period is well above the critical period for breakup due to rotational instability. Accounting for dust contamination,our best estimate of the absolute magnitude leads to a nucleus radius $r_n \sim 0.4 \pm 0.1$ km. Finally, we found phase-lagged brightness variations in the coma that indicate a dust outflow speed of $v_g = 107 \pm 9$ m s^{-1}, corresponding to average dust particle radius $\bar{a} \sim 3 \pm 1$ μm. The mass loss rate, $dM/dt \sim 50$ kgs^{-1}, is consistent with sublimation of an exposed, ice patch of radius only $\sim$0.2 km. We also analyzed fragments 73P-B and 73P-G, which shed 10s to 100s of tertiary fragments themselves (Graykowski & Jewitt In Prep). From a high resolution study of fragmenting comet 73P/Schwassmann-Wachmann 3 we find the mini fragments within

73P-B have a range of velocities, v $\sim$ 0.95 - 6.58 ms^{-1}, relative to the motion of parent fragment 73P-B. These velocities indicate an impulsive ejection time that occurred 7.4 ± 0.2 days prior to the observations (prior to 2006 April 20). We also found a differential index $q = 3.1 \pm 0.5$ for the distribution of the mini fragments shed from 73P-B and a differential index $q = 2.2 \pm 0.5$ for the distribution of the mini fragments shed from 73P-G. Finally, we found the mass of 73P-B is $\sim 9.28 \times 10^{10}$ kg ($r \leq 354.0 \pm 7.0$ m) and the lower limit on the total mass including all the tertiary fragments is $\sim 9.55 \times 10^{10}$ kg. The mass of 73P-G is $r \leq 58.2 \pm 2.4$ kg ($r \leq 58.2 \pm 2.4$ m) and the lower limit on the total mass including all the secondary fragments is $\sim 1.04 \times 10^{9}$ kg.

5.2.2 Future Prospects for Fragmented Comet Surveys

While understanding the fragmentation of a single comet has aided greatly the understanding of its evolution and our ability to predict future fragmentation events, it is important to understand how the fragmentation 73P fits in context with comet populations as a whole. Additionally, the dominant fragmentation mechanism(s) may differ amongst the SPC and LPC populations. When observing long period comets (period $>$ 200 years), Levison et al. (2002) found there were fewer dormant comets than predicted by models by a factor of 100. Belton (2015) made a similar observation for short period comets (period $<$ 200 years). In both cases, more comets than expected had completely disappeared. In each study, the dynamical models did not account for fragmentation. This implies that comet fragmentation could have played a role in the disappearance of these comets. The fact that this is the case for both long and short period comets suggests that, regardless of their distance to the sun, comets are fragmenting, and eventually disrupting. It then is important to develop fragmentation models in order to understand whether there is a difference in fragmentation mechanisms between short and long period comets, or if the mechanisms are independent of long versus short period comets.

Also, obtaining a fragmentation rate will aid in measuring the effect of fragmentation on the lifetime of a comet. In a previous survey, Chen and Jewitt (1994) estimated an average rate of 0.01 fragmentation events per comet per year, but could not determine whether this rate applies equally to all comets or if some comets are especially prone to breakup while others are essentially immune to fragmentation. Also, due to poor statistics, a fragmentation rate could not be determined separately for long and short period comets. Obtaining a fragmentation rate for long and short period comets separately will illuminate whether different fragmentation mechanism dominate in each population. Also, improving the statistics on the overall cometary fragmentation rate will also help identify whether or not fragmentation is the main mechanism of comet destruction in general.

In general, we expect the comets to split when they are the most active, which is when the body reaches perihelion because sublimation rates increase with temperature. Each year, ∼70 short period comets pass through perihelion. Observations should not be limited to comets reaching perihelion, because not all splitting mechanisms rely on outgassing of materials and have the potential to split at any distance from the sun. Long period comets are much less well observed because comets spend the majority of their time near apogee rather than near perihelion. With periods as small as 200 years, reaching up to 1000s of years, long period comets are usually far from the sun, inactive, and therefore unable to be observed. Only ∼15-20 long period comets come to perihelion each year, and most often are not discovered until 1 or 2 years ahead of this date when their magnitude has finally increased enough to be observed. This means there is likely an observable reservoir of ∼30-40 long period comets a year. An archival search for missed fragmentation events would be beneficial as well. I expect the split rate to be higher for LPCs than SPCs. LPCs tend to be smaller in size than the average SPC with diameters < 1 km, while SPCs reach larger sizes on the order of 10km in diameter (Nesvorný 2017). Smaller bodies will experience greater thermal stress, than the larger bodies, and therefore disrupt more easily (Whitman et al. 2006, Belton et al. 2015). This indicates that the most common fragmentation mechanism is thermal. However this could be due to observational bias as comets near the sun, disrupting from thermal effects will be very bright. However a comet that splits further from the sun due to rotational instability, for example, can be much less bright. A complete observational survey would allow for an accurate estimate of fragmentation rate.

REFERENCES

[1] Agnor, C. B. & Hamilton, D. P. 2006, Nature, 441, 192

[2] Belton, M. J. S. 2015, Icarus, 245, 87

[3] Chamberlain, M. A. & Brown, R. H. 2004, Icarus, 172, 163

[4] Chen, J. & Jewitt, D. 1994, Icarus, 108, 265

[5] Cruikshank, D. P., Degewij, J., & Zellner, B. H. 1982, Satellites of Jupiter, 129

[6] Denk, T. & Mottola, S. 2019, Icarus, 322, 80

[7] Di Sisto, R. P., Fernández, J. A., & Brunini, A. 2009, Icarus, 203, 140

[8] Goldreich, P., Murray, N., Longaretti, P. Y., et al. 1989, Science, 245, 500

[9] Grasset, O., Dougherty, M. K., Coustenis, A., et al. 2013, Planet. Space Sci., 78, 1

[10] Graykowski, A. & Jewitt, D. 2018, AJ, 155, 184

[11] Graykowski, A. & Jewitt, D. 2019, AJ, 158, 112

[12] Graykowski, A. & Jewitt, D. 2022, in prep

[13] Jarvis, K. S., Vilas, F., Larson, S. M., et al. 2000, Icarus, 145, 445

[14] Jewitt, D. & Haghighipour, N. 2007, ARA&A, 45, 261

[15] Lam, T., Buffington, B., Campagnola, S. 2018, In 2018 Space Flight Mechanics Meeting, 0202

[16] Levison, H. F., Morbidelli, A., Dones, L., Jedicke, R., Wiegert, P. A., Bottke Jr, W. F. 2002, Science, 296, 2212-2215

[17] Luu, J. X. 1991, Asteroids, Comets, Meteors 1991, 765, 141

[18] Morbidelli, A., Levison, H. F., Tsiganis, K., et al. 2005, Nature, 435, 462

[19] Nesvorný, D., Vokrouhlický, D., & Morbidelli, A. 2013, ApJ, 768, 45

[20] Nesvorný, D., Vokrouhlický, D., Dones, L., Levison, H. F., Kaib, N., Morbidelli, A. 2017, AJ, 845, 27

[21] Peña, J. & Fuentes, C. 2022, AJ, 163, 274

[22] Porco, C. C., Baker, E., Barbara, J., et al. 2005, Science, 307, 1237

[23] Porco, C. C., West, R. A., McEwen, A., et al. 2003, Science, 299, 1541

[24] Whitman, K., Morbidelli, A., & Jedicke, R. 2006, Icarus, 183, 101

[25] Sayanagi, K., Wong, M., Becker, T., et al. 2021, BAAS

[26] Vilas, F., Lederer, S. M., Gill, S. L., et al. 2006, Icarus, 180, 453